INSIGHT INTO THE FLOW CHARACTERISTICS DOWNSTREAM OF MICRO VORTEX GENERATORS

A THESIS SUBMITTED TO
THE GRADUATE SCHOOL OF NATURAL AND APPLIED SCIENCES
OF
MIDDLE EAST TECHNICAL UNIVERSITY

BY

MUHİDDİN TUĞRUL AKPOLAT

IN PARTIAL FULFILLMENT OF THE REQUIREMENTS
FOR
THE DEGREE OF DOCTOR OF PHILOSOPHY
IN
AEROSPACE ENGINEERING

SEPTEMBER 2023

Approval of the thesis:

INSIGHT INTO THE FLOW CHARACTERISTICS DOWNSTREAM OF MICRO VORTEX GENERATORS

submitted by **Muhiddin Tuğrul AKPOLAT** in partial fulfillment of the requirements for the degree of **Doctor of Philosophy** i**n Aerospace Engineering, Middle East Technical University** by,

Prof. Dr. Halil Kalıpçılar
Dean, Graduate School of **Natural and Applied Sciences** _____

Prof. Dr. Serkan Özgen
Head of the Department, **Aerospace Engineering, METU** _____

Asst. Prof. Dr. Mustafa Perçin
Supervisor, **Aerospace Engineering, METU** _____

Examining Committee Members:

Prof. Dr. Oğuz Uzol
Aerospace Engineering, METU _____

Asst. Prof. Dr. Mustafa Perçin
Aerospace Engineering, METU _____

Prof. Dr. Metin Yavuz
Mechanical Engineering, METU _____

Asst. Prof. Dr. Hayri Acar
Aeronautical Engineering, ITU _____

Asst. Prof. Dr. Onur Baş
Mechanical Engineering, TEDU _____

Date: 08.09.2023

I hereby declare that all information in this document has been obtained and presented in accordance with academic rules and ethical conduct. I also declare that, as required by these rules and conduct, I have fully cited and referenced all material and results that are not original to this work.

Muhiddin Tuğrul, Akpolat:

Signature :

ABSTRACT

INSIGHT INTO THE FLOW CHARACTERISTICS DOWNSTREAM OF MICRO VORTEX GENERATORS

Akpolat, Muhiddin Tuğrul
Doctor of Philosophy, Aerospace Engineering
Supervisor : Asst. Prof. Dr. Mustafa Perçin

September 2023, 160 pages

This study investigates the wake characteristics of Micro Vortex Generators (MVGs) in a subsonic flow regime. First, the wakes generated by three ramp-type MVGs with different height-to-boundary layer thickness ratios (h/δ) are characterized experimentally using a two-dimensional two-component particle image velocimetry technique. The experimental results are complemented with three-dimensional numerical simulations for five different h/δ ratios ranging from 0.18 to 0.54. The effect of the device height, or the h/δ ratio, is investigated in terms of velocity components, vorticity distributions, turbulence properties, and various decay parameters, such as maximum streamwise velocity deficit and maximum upwash velocity, using five different device heights employing the experimental and numerical results. The self-similarity of the ramp-type MVG wake in terms of streamwise and wall-normal velocity components is investigated. The wake flow properties are then compared to similar types of MVGs operating in the supersonic regime available from the literature. The experimental and numerical results reveal general operating principles and wake decay characteristics in the low subsonic flow regime, which display similar characteristics to MVGs of similar h/δ values operating at supersonic conditions. It is shown that the vortex strength, and thus

mixing and wake decay characteristics, depend on the effective device Reynolds number regardless of the Mach number. A wake model is suggested by using the self-similarity of the ramp-type MVGs and the wake decay parameters. Using the detailed investigation of the decay parameters for the modeling efforts, a method to designate the limit between MVGs and conventional (δ-scale) vortex generators is suggested based on the wake deficit decay characteristics. The model is then used to reconstruct wakes of ramp-type MVGs in supersonic flow regimes from the literature.

Keywords: Micro Vortex Generators, Flow Control, Experimental Aerodynamics, Computational Fluid Dynamics

ÖZ

MİKRO GİRDAP ÜRETEÇLERİNİN İZ BÖLGELERİNİN KARAKTERİSTİKLERİ ÜZERİNE BİR ÇALIŞMA

Akpolat, Muhiddin Tuğrul
Doktora, Havacılık ve Uzay Mühendisliği
Tez Yöneticisi: Yrd. Doç. Dr. Mustafa Perçin

Eylül 2023, 160 sayfa

Bu çalışma, düşük sesaltı bir akış rejiminde Mikro Girdap Üreteçlerinin (MGÜ'ler) iz bölgesi karakteristiklerini araştırmaktadır. İlk olarak, farklı yükseklik-sınır tabaka kalınlığı oranlarına (h/δ) sahip üç rampa tipi MGÜ tarafından üretilen iz bölgeleri deneysel olarak iki boyutlu iki bileşenli parçacık görüntülemeli hızölçer (2D2C PIV) tekniği kullanılarak karakterize edilmiştir. Deneysel sonuçlar, 0.18 ile 0.54 arasında değişen beş farklı h/δ oranı için üç boyutlu sayısal simülasyonlarla tamamlanmıştır. Cihaz yüksekliği, yani h/δ oranı, hız bileşenleri, girdaplılık dağılımları, türbülans özellikleri, ve akış yönündeki hız bozunumu, akışa dik yöndeki hız bozunumu ve bunların pozisyonları olmak üzere çeşitli bozulma karakteristikleri açısından beş farklı cihaz yüksekliği kullanılarak deneysel ve sayısal sonuçlar üzerinden incelenmiştir. Rampa tipi MGÜ'lerin ürettikleri akış yönündeki ve akışa dik yöndeki hız bileşenlerinin özbenzerlikleri araştırılmıştır. İz bölgesi akış özellikleri daha sonra literatürden elde edilen süpersonik rejimde çalışan benzer MGÜ türleri ile karşılaştırılmıştır. Deneysel ve sayısal sonuçlar, düşük süpersonik akış rejiminde genel çalışma prensiplerini ve iz bölgesi bozulma karakteristiklerini ortaya koymaktadır, ki bu da süpersonik koşullarda çalışan benzer h/δ değerlerine sahip MGÜ'lerle benzer özellikler göstermektedir. Girdap gücü ve dolayısıyla karışım ve iz bölgesi bozulma özellikleri, Mach sayısına bakılmaksızın efektif cihaz Reynolds

sayısına bağlı olduğu gösterilmiştir. Rampa tipi MGÜ'lerin özbenzerlikleri ve bozulma karakteristikleri kullanılarak bir iz bölgesi modeli önerilmiştir. İz bölgesini modelleme çalışmaları sırasında detaylı bir şekilde incelenen bozulma karakteristkilerini kullanarak MGÜ'ler ile geleneksel (δ-ölçekli) girdap üreteçleri arasındaki sınırı belirlemek için bir yöntem önerilmiştir. İz bölgesi modeli daha sonra literatürde bulunan bazı rampa tipi MGÜ'lerin iz bölgesini modellemek için kullanılmıştır.

Anahtar Kelimeler: Mikro Girdap Üreteçleri, Akış Kontrolü, Deneysel Aerodinamik, Sayısal Akışkanlar Dinamiği

ACKNOWLEDGMENTS

I would like to express my deepest gratitude to my advisor, Dr. Mustafa Perçin, for his guidance and encouragement. Working with him, learning from him, and being his first Ph.D. student has been an invaluable honor.

I would like to thank the members of the Thesis Advisory Committee, Prof. Dr. Metin Yavuz and Prof. Dr. Oğuz Uzol, for their criticism and guidance with their out-of-the-box ideas. I sincerely thank Dr. Rajan Kumar from Florida State University for the first discussions on the topic.

I am grateful to Dr. Atılgan Toker for his support, guidance, and encouragement. I deeply thank my friend and mentor, Dr. Ali Doğrul, for his advice throughout my life and academic career. I would like to thank Dr. Mustafa Serdar Genç, who made me realize how hard I can work and have fun doing it.

I would like to thank all the personnel from the METU Center for Wind Energy (METUWind, RÜZGEM) for their help and friendship. I would like to thank again Prof. Dr. Oğuz Uzol, the director of RÜZGEM, and Dr. Mustafa Perçin, the laboratory coordinator, for their support and for giving me the opportunity to work on various experiments and projects. I will always reminisce about working in the labs of RÜZGEM with joy and pride for years, often working from dusk to dawn. I must give special thanks to my dear friend and brother, Dr. Anas Abdulrahim, with whom we worked together for years, spending countless hours setting up equipment and conducting experiments.

I express my most profound appreciation to Tekin Aksu for helping me through the hard times, believing in me, for his friendship, and for sharing his deep knowledge of numerical methods. I would like to thank my friends, Dr. Mustafa Akdemir, Can Çıtak, Özgür Harputlu, and Ergun Umut Kılınç, for the inspiring discussions we had regarding Computational Fluid Dynamics.

The acknowledgment part of this thesis is not complete without Buğrahan Öztürk and Abdelrahman Hassanein, as we have worked on the topic together and shared lots of great moments while, of course, drinking liters of coffee; thank you for being there for me and improving this study.

I would like to express my sincere gratitude to Safa Aysan for always being there to assist me whenever I needed help, especially during my recovery period. I express utmost gratitude to my remarkable roommate, business associate, and friend, Babür Erdem, the bee whisperer. I would like to thank my dear friend Rauf Aksu for his constant support and companionship, which have been invaluable to me.

I express my deepest thanks to my friends who endured me during my Ph.D. Big thanks go to; Nil Akdede, Elif Can Çayan Aksu, Ezgi Arısoy, Mevlüt Aycan Aşıkoğlu, Serdar Başdemir, Doğa Beşer, Cenk Çetin, Oğuz Eren, Salih Ertan, Barış Fiçer, Dr. Hooman Amiri Hazaveh, Irmak Taylan Karpuzcu, Fırat Kıyıcı, Burak Kızılkaya, Yasemin Kösa, Dr. Engin Leblebici, Berkan Mumcu, Utku Olgun, Dr. Oğuz Kaan Onay, Gülay Oskay, Dr. Yaşar Ostovan, Alp Pirci, Halil Ünay, Alper Yetiş, and Dr. Onur Yontar.

I am filled with immense gratitude towards my family for the support and trust they have shown me.

Finally, I want to express my gratitude to Nur Elif Yurdaçalış for always being there for me and providing unwavering support.

As this study, which has been reminding me of the punishment of Sisyphus, comes to an end, it seems like the boulder is getting closer to the top of the hill once again. And finally, I would like to pledge to myself that I will continue to derive my inspiration not from the heavens or an unseen world but from life itself.

"*One must imagine Sisyphus happy.*"

Albert Camus

TABLE OF CONTENTS

LIST OF TABLES

TABLES

LIST OF FIGURES

FIGURES

LIST OF ABBREVIATIONS

ABBREVIATIONS

2D2C PIV	Two-Dimensional Two-Component Particle Image Velocimetry
BL	Boundary Layer
CFD	Computational Fluid Dynamics
FOV	Field of View
HWA	Hot-Wire Anemometry
ILES	Implicit Large Eddy Simulation
K-H	Kelvin-Helmholtz
LDA	Laser Doppler Anemometry
LES	Large Eddy Simulation
MVG	Micro Vortex Generator
NACA	The National Advisory Committee for Aeronautics
NASA	The National Aeronautics and Space Administration
Nd:YAG	Neodymium-Doped Yttrium Aluminum Garnet
PIV	Particle Image Velocimetry
POD	Proper Orthogonal Decomposition
RANS	Reynolds Averaged Navier-Stokes
SBLI	Shockwave Boundary Layer Interaction
SPOD	Snapshot Proper Orthogonal Decomposition
SST	Shear Stress Transport
TI	Turbulence Intensity
TKE	Turbulent Kinetic Energy
VG	Vortex Generator (Conventional vortex generators or vortex generators with heights larger than or comparable to the local boundary layer thickness)

LIST OF SYMBOLS

SYMBOLS

$\overline{U}$, $\overline{V}$	Normalized Streamwise and Wall-Normal Velocities
$\bar{y}$	Length Scale
A, B	Coefficients For Modeling the Streamwise Velocity Profiles
c	Chord
C, D	Coefficients For Modeling the Wall-Normal Velocity Profiles
g	Gap For Vane-Type MVGs
h	Device Height
H	Shape Factor
h^+	Device Reynolds Number
h_e	Effective Device Height
h_e^+	Effective Device Height Reynolds Number
k	Cut-Off Factor
M	Mach Number
Re	Reynolds Number
Re_θ	Momentum Thickness Reynolds Number
U	Streamwise Velocity (x-direction)
u'	Streamwise Velocity Fluctuation
U^+	Dimensionless Velocity
U_∞	Freestream Velocity
U_{BL}	Undisturbed Boundary Layer Velocity
U_{Def}	Maximum Velocity Deficit ($\lvert U_{BL}-U\rvert_{max}$)
U_{eff}	Effective Hot-Wire Cooling Velocity
U_{min}	Minimum Streamwise Velocity or Maximum Velocity Deficit
U_τ	Friction Velocity
u'v'	Reynolds Shear Stress
V	Wall-Normal Velocity (y-direction)

v'	Wall-Normal Velocity Fluctuation
V_{max}	Maximum Wall Normal Velocity or Maximum Upwash Velocity
W	Spanwise Velocity (z-direction)
W	Width
w	Width of MVG
w_U	Wake Width for Streamwise Velocity Profiles
w_V	Wake Width for Wall-Normal Velocity Profiles
x, y, z	Coordinate System
y^+	Length Scale
y_{Udef}	Position of the Maximum Velocity Deficit (U_{Def})
y_{V1}, y_{V2}	Positions Defining the Wake Width for Wall-Normal Velocity
y_{Vmax}	Position of the Maximum Upwash Velocity
y^*	Constant Wake Width Factor
α	Device Angle
Γ	Circulation
Γ_5	Circulation at Five Device Heights Downstream
δ	Boundary Layer Thickness
δ^*	Displacement Thickness
θ	Momentum Thickness
μ	Dynamic Viscosity
ρ	Density
υ	Kinematic Viscosity
τ	Wall Shear Stress
c_t	Constant
Ω	Vorticity

CHAPTER 1

INTRODUCTION

Vortices are omnipresent in the universe, ranging from the Great Red Spot of Jupiter, which has a diameter of 1.3 times that of the Earth, to the tiniest microorganisms having a length between 500 to 1200 micrometers, generating vortex fields to ensnare their prey (Figure 1.1).

The device called Micro Vortex Generator is but a small means to generate and employ the ubiquitous phenomena that are vortices, seen throughout our universe, possibly to control flow at various regimes, subsonic, transonic, supersonic, and hypersonic alike.

In order to focus on the flow control aspect of vortices, this chapter includes some findings from the literature. The chapter starts with the definition of boundary layer control and its types and continues with their areas of applications, where a more elaborate discussion on Micro Vortex Generators can be found. The chapter concludes with the organization and objectives of this study.

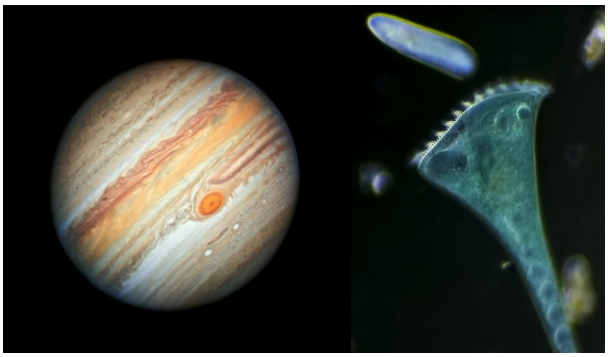

Figure 1.1 Left: The Great Red Spot seen in between two jet streams, as seen by the Hubble Space Telescope [1]. Right: A *Paramecium* getting caught by a *Stentor coerulus* by the action of vortices created by its cilia (still from [2]).

1.1 Boundary Layer Control

Methods of boundary layer control -or flow control in general- which are employed in many engineering applications aim to introduce various types of perturbations into the flow field in order to alter the flow development with goals such as lift enhancement, drag reduction, mixing enhancement, heat transfer enhancement, and noise reduction.

One of the most crucial utilization of flow control is found in aerospace applications. Since most of the flow control applications in aerospace problems are made in a way that utilizes perturbations or alterations to the boundary layer itself, it is safe to call them boundary layer control.

Boundary layer control methods can be divided into two categories: active and passive [3]. Examples of active boundary layer control methods are suction and blowing [4], acoustic excitation [5, 6], oscillations [7], and air jet vortex generators [8]. Active flow control methods can be altered with the changing conditions of the flow, such that they can simply be "turned off" when they are not needed. However, they are also more complex, with a variety of moving parts, compared to the passive boundary layer control methods.

Passive boundary layer control methods, as the name suggests, are passive, meaning they can not be moved or altered by any means. Therefore, they are nothing but a cause of drag in the off-design conditions. So, caution should be taken when employing passive boundary layer control methods. Passive boundary layer control methods include boundary layer bleed, vortex generators, added surface roughness, and cavities [9].

Boundary layer bleed is a well-established and proven method of boundary layer control, especially for supersonic air inlets [10, 11]. Boundary layer bleed is achieved by adding slots or perforated sections to remove the low-momentum flow from the boundary layer, resulting in a more energetic boundary layer that is less prone to separation. However, with the bleed mass flow removed from the system, the

combustor loses its invaluable mass flow, resulting in an inlet design that is larger and heavier to provide the same mass flow to the combustor.

Adding vortex generators (VGs) to the surface is also a commonly used method. After they were introduced by Taylor [12] in the 1940s, quite a few researchers started investigating their effects and viability for various applications, as seen from the NACA reports published in the following years [13, 14, 15, 16, 17, 18, 19, 20]. Some of the foci of these investigations are delaying separation on flat plates, airfoils, wings, and swept wings, both at low speeds and transonic regimes. McCullough *et al.* [14] employed pyramidal, wedge-like bodies in order to delay the separation of a turbulent boundary layer. The device they employed was, in essence, a ramp-type VG, and this study is probably the first example where a ramp-type VG is investigated (Figure 1.2). The flat plate experiments showed that it is desirable to lower the sizes of the wedges as much as possible to compensate for the increased drag. They have also conducted experiments with the wedges mounted on a NACA 63(3)-018 airfoil, resulting in a reduced separation. The results showed that the drag force is increased with the VGs attached. However, at higher angles of attack, that is, flow with a larger separated region, they have recorded reduced drag with VGs than without them. Finally, they have conducted experiments employing vane-type VGs much smaller than their wedge-type counterparts. Results showed that the same mixing effect with smaller VGs was possible, with about half the cost in drag, as they showed approximately the same increase in the maximum lift with their larger counterparts.

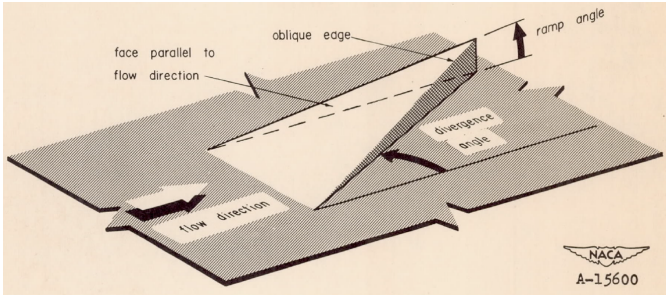

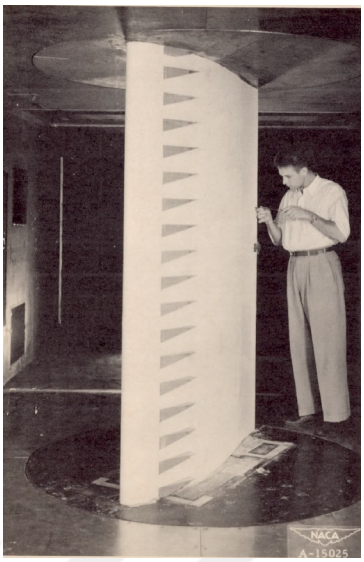

Figure 1.2 Sketch showing the device employed and the devices mounted on a NACA 63(3)-018 airfoil [14].

Weiberg and McCullough [16] successfully employed wedge-shaped VGs, improving the stability of a swept-back wing at Mach 0.16. Schubauer and Spangenberg [21] employed VGs to increase the rate of mixing in turbulent boundary layers. They have created various types of adverse pressure gradients on a flat plate and compared different fixed VGs in the adverse pressure gradient region, including ramp type, backward-facing ramp type, and vane-type VGs. They have reported that the mixing mechanics are similar for all the devices studied, introducing high momentum from the freestream flow to the boundary layer, with the differences of the devices compared rising from their form of achieving this and their drag penalty. Calerese *et al.* [22] experimentally investigated the effects of VGs on a scaled model of a C-130 aircraft body with the aim of reducing the total drag by delaying separation in the regions with adverse pressure gradient since the fuel consumption of the aircraft was excessive due the drag resulting from its highly upswept afterbody. They have also investigated the effects of small elements with a height lower than the boundary layer. Both VGs and small elements achieved noticeable drag reduction. However, the small elements resulted in much lower drag.

Vortex generators also found applications in wind turbines to control the flow separation and improve the overall performance of wind turbines [23, 24]. Moreover,

VGs have been applied and are still being used in wind turbines. UpWind Solutions, Inc. implemented the first application, increasing Annual Energy Production and reducing power scatter created by stalls during gusty wind conditions [25]. Gao *et al.* [26] studied the effects of VGs on an airfoil with a blunt trailing edge for wind turbines. The results showed that VGs significantly increase the maximum lift coefficient and stall angle of attack. They have concluded that increasing the device height increases the lift generated; however, the lift-to-drag ratio is reduced with the added drag penalty. They have also stated that the stronger vortices generated by VGs having larger dimensions do not necessarily result in better flow separation control.

1.2 Boundary Layer Control Employing Micro Vortex Generators

The studies summarized above mainly employed vortex generators with heights larger than or comparable to the local boundary layer thickness (δ-scale) to introduce high-momentum fluid from the freestream through corotating or counterrotating streamwise vortices. Kuethe [27] introduced the concept of having VGs embedded inside the boundary layer by employing semi-circular cross-section elements having height-to-boundary layer thickness (h/δ) ratios of 0.27 and 0.42 to reduce the noise generation by suppressing the Karman vortex street. Later, these VGs, called Sub-Boundary Layer Vortex Generators, Low-Profile Vortex Generators, or Micro Vortex Generators (MVGs), started to appear in various studies at subsonic velocities, and in the late 2000s, the emphasis of the studies in the literature shifted to supersonic flow regimes.

MVGs are passive boundary layer control devices that are submerged in the boundary layer itself. They control the boundary layer by generating vortices in the streamwise direction. As a consequence of being submerged in the boundary layer, the vortices generated by MVGs promote mixing between the sublayers of the boundary layer, creating a momentum exchange between the near-wall region (low momentum) and upper region (relatively higher momentum) of the boundary layer as defined in Figure 1.3) [28]. As the near-wall region of the boundary layer gains

momentum, the boundary layer becomes less susceptible to the effects of an adverse pressure gradient. The vortices created by the MVG generate this momentum transfer by means of upwash and downwash. As can be seen from the sketch in Figure 1.3, the upwash lifts the low-momentum fluid upwards, whereas the downwash entrains the high-momentum fluid towards the wall. As mentioned earlier, VGs promote mixing by entraining high-momentum fluid from the freestream to the boundary layer, while MVGs promote mixing inside the boundary layer itself.

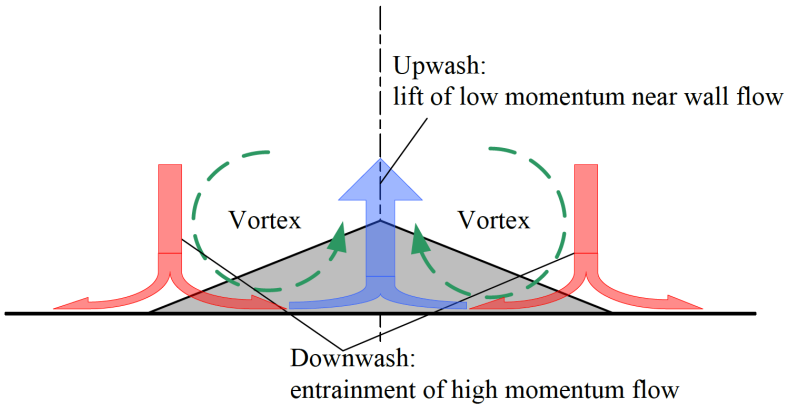

Figure 1.3 Sketch of the front view of a ramp-type MVG, illustrating streamwise vortex pair, upwash, and downwash (the direction freestream flow is pointing into the paper) [28].

After the work of Kuethe [27] at subsonic regimes, Holmes *et al.* [29] investigated the effects of MVGs on reducing the interior noise generated on the Gulfstream III, extending the investigations on MVGs to transonic regimes. VGs were used in Gulfstream II with partial success, as they were not able to reduce the noise levels to the desired levels on all frequencies [30]. Therefore, they have proposed to use MVGs instead. By delaying the shock-induced separation, MVGs were successfully found to reduce the noise levels in flight tests, eventually leading to a retrofit program of Gulfstream III aircraft (Figure 1.4). After the successful application on Gulfstream III aircraft, MVGs developed by NASA Langley found applications on the wings of Gulfstream V (Figure 1.5), helping the aircraft achieve higher maximum cruise speed, extending its range, and improving its stability [31].

Figure 1.4 An array of MVGs seen on top of the cockpit of a Gulfstream III. Image courtesy of Jonathan Zaninger [32].

Figure 1.5 MVGs on the Wings of a Gulfstream V [31].

As defined by Holmes *et al.* [29], MVGs increase the robustness of the boundary layer near the wall, where it is most susceptible to the effects of an adverse pressure gradient, unlike VGs. As illustrated in the sketch given in Figure 1.6, MVGs also have the intrinsic advantage of generating less drag and being more robust mechanically compared to VGs, as they are smaller in size.

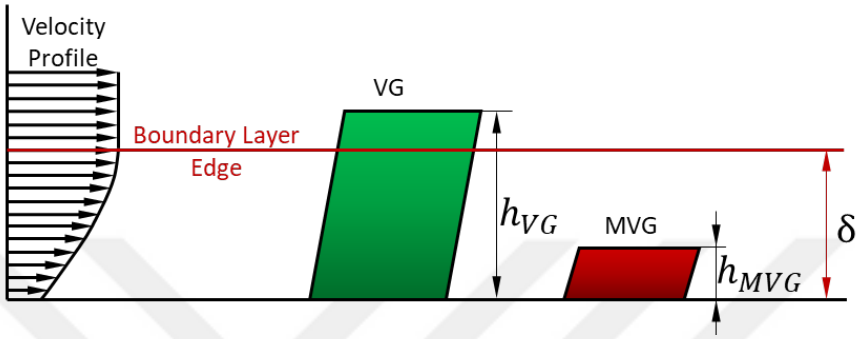

Figure 1.6 Size comparison of a typical VG and MVG to a typical boundary layer. Recreated from Holmes *et al.* [29].

Rao and Kariya [33] experimentally compared MVGs with an h/δ ratio of 0.625 or less with VGs on a flat plate turbulent boundary layer with an adverse pressure gradient. The results showed that an optimum arrangement of MVGs has the potential of exceeding the performance of VGs, primarily because of much lower added drag.

In the 1990s, Lin *et al.* [34, 35, 36] conducted experimental studies employing various types of MVGs at low speeds for controlling separated flow over a backward-facing ramp. For comparison, they have also conducted pressure measurements using VGs. The results showed that VGs create a more three-dimensional wake than MVGs, indicating that the vortices generated by VGs are indeed stronger than those generated by MVGs. However, since the results also show that both VGs and MVGs have the capability to control the flow, it can be safely stated that the vortices generated by VGs are stronger than necessary. They have concluded that smaller MVGs of the same type could perform as well as their larger counterparts, with an expected reduced device drag. Results agreeing with this study were presented by Kerho *et al.* [37]. They have employed MVGs having h/δ ratios of 0.8 and 0.3 to control the laminar separation bubble on a LA2573A airfoil at low

Reynolds numbers. A drag reduction of up to 38% was achieved with the MVGs installed. It was shown that the size of the laminar separation bubble was reduced in some cases, whereas in others, it was eliminated entirely. However, the authors stated that although it is possible to eliminate the separation bubble by prematurely forcing transition with larger MVGs, it might be desirable to use smaller MVGs that provide the circulation needed without generating the turbulent boundary layer immediately.

Another study by Lin *et al.* [38] focused on utilizing MVGs in high-lift applications. MVGs have their inherent advantage of being small in this application since they can be retracted with the flaps, causing no drag penalty during the cruise, which NASA Langley already realized on the Piper Malibu Meridian aircraft's flaps (Figure 1.7). With MVGs applied to its flaps, the aircraft achieved a slower stall speed, enabling it to pass the required safety regulations by the Federal Aviation Administration in 1996 [31]. Lin *et al.* [38] have concluded that MVGs could effectively control flap separation, increasing the lift-to-drag ratio by 100%. They have used MVGs producing two types of vortices, corotating and counterrotating, concluding that although both types effectively reduce the flow separation, the counterrotating vortices were slightly more effective. An agreeing study was presented by Godard and Stanislas [39], as they tested vane-type MVGs in counterrotating and corotating configurations having an h/δ range of 0.2 to 0.46, and the results showed that the former is approximately 100% more effective in increasing skin friction under the effect of an adverse pressure gradient.

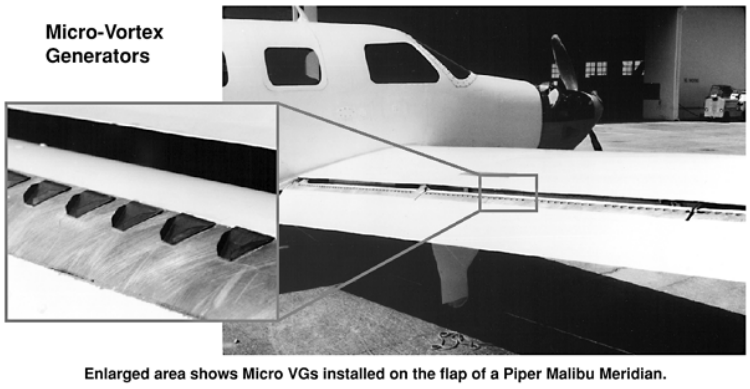

Figure 1.7 MVGs on the flap of a Piper Malibu Meridian [31].

Vane and ramp-type devices are the most encountered types of MVGs in the literature for both high and low-speed applications [28, 40, 41]. Configuring vane-type MVGs to produce corotating or counterrotating vortices is possible, whereas ramp-type MVGs are counterrotating vortex-producing devices. The definitions of geometrical parameters for counterrotating vane-type and ramp-type MVGs can be found in Figure 1.8. Counterrotating vane-type MVGs, in most cases, create stronger vortices than ramp-type MVGs in subsonic and supersonic flow conditions [40, 41].

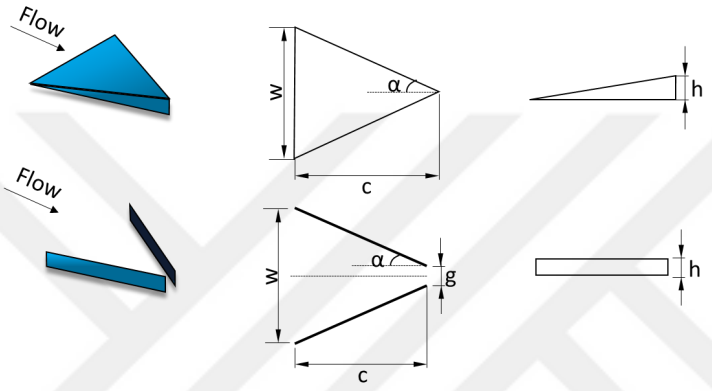

Figure 1.8 Top: ramp-type MVG. Bottom: vane-type MVG (counterrotating configuration).

Ashill *et al.* [42, 43] characterized various types of MVGs, namely counterrotating vanes (spaced and joined), single vane, ramp, and backward ramp, in terms of vortex strength, decay, and trajectory up to 50 device height downstream distances in both zero and adverse pressure gradient conditions at freestream velocities ranging from 10 m/s to 40 m/s. The results showed that the counterrotating vane had twice the vortex strength compared to the ramp. However, drag measurements in zero pressure gradient showed that ramp-type MVG had 40% drag compared to the counterrotating vanes, which agrees with the results of Schubauer and Spangenberg [21] for conventional (δ-scale) vanes and ramps.

Ashill *et al.* [42, 43] also presented the results of non-dimensional circulation downstream of the MVGs at x/h=5. The non-dimensional circulation was correlated with a Reynolds number called the device Reynolds number given below,

$$h^+ = \frac{hu_\tau}{\nu} \qquad [1.1]$$

The non-dimensional circulation generated by each type of MVG can be seen in Figure 1.9. However, it was seen that the circulation only varies slightly with the device Reynolds number after a particular value. Therefore, in order to generalize this correlation, in other words, in order to generalize the correlation by ruling out the device geometry, they have used the concept they call the effective height. Taking the effective height of ramp-type MVG to be equal to its actual height, they have equalized the maximum value of non-dimensional circulation of all the devices. The resulting correlation is given in Figure 1.10. As can be seen from Figure 1.10, it was found that the vortex strength of MVGs having an effective device Reynolds number (h_e^+) higher than 1400 falls into a single line.

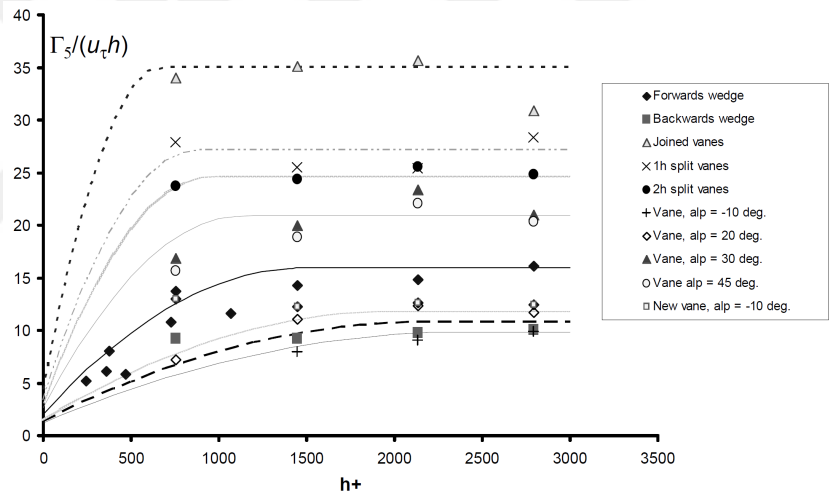

Figure 1.9 Non-dimensional circulation versus device Reynolds number for different MVGs at five device heights downstream of the MVGs [40].

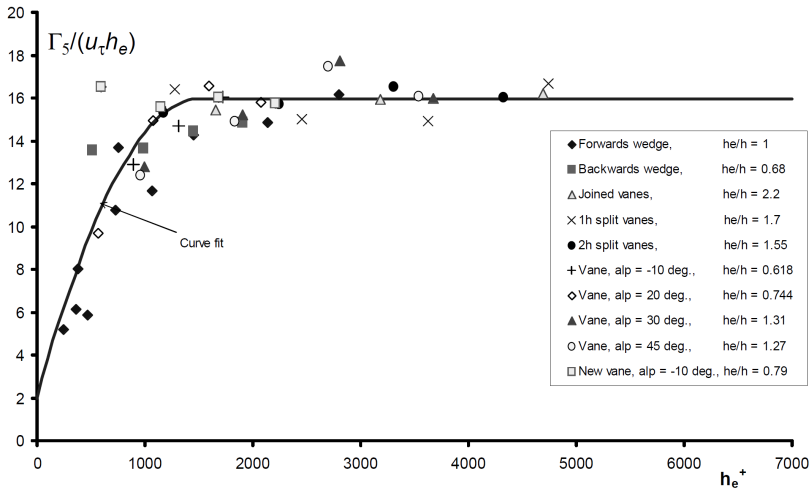

Figure 1.10 Generalized non-dimensional circulation versus device Reynolds number for different MVGs at five device heights downstream of the MVGs [40].

MVGs found some applications in the wind energy field. Velte and Hansen [44] examined the effects of counterrotating vane-type MVGs on an airfoil to achieve separation control on DU 91-W2-250 airfoil, which is a wind turbine dedicated airfoil. The MVGs, having an h/δ ratio of 0.56, were placed on 20% of the airfoil chord. The MVGs altered the flow to have much less or no separation, resulting in an improved lift-to-drag ratio. At far downstream positions (x/h=48), flow structures induced by the MVGs covered the entire boundary layer thickness, exceeding the MVG height. In their numerical study, Martínez-Filgueira *et al.* [45] studied vane-type vortex generators with five different heights, the largest having the same height as the local boundary layer thickness, whereas the smallest having a height of 20% of the local boundary layer thickness. The results showed that all the vortex generators with different heights have the same trends of vortex trajectories compared with the vortex generator with a height equal to the local boundary layer thickness, except the smallest one. Yan *et al.* [46] investigated the effects of MVGs on the aerodynamic performance of an airfoil and a vertical-axis wind turbine rotor. Results showed a significant increase in the lift-to-drag ratio for the airfoil with an increase of 2° in the stall angle. For the wind turbine, with the MVGs installed, the power production was found to be increasing even at a high tip speed ratio, whereas the power production was low for the uncontrolled case.

Another potential application of MVGs is on fuselages of rotary wing aircraft. Tai [47] numerically investigated the effects of MVGs on the V-22 for forward flight configuration. They have installed ten counterrotating vane-type MVGs to the overwing fairing of V-22. The MVGs created a beneficial effect on both lift and drag coefficients. However, the results showed that in order to achieve separation alleviation and use the full potential of MVGs, consideration must be given to the chordwise location and the incidence angle of the MVGs. Syahin *et al.* [48] conducted wind tunnel experiments on a helicopter fuselage that is designed for a wing-in-ground effect vehicle at a velocity range of 1 m/s to 10 m/s with and without ramp-type MVGs. Up to a 21% reduction in drag coefficient was achieved with MVGs.

MVGs found applications in supersonic flow regimes as well, with an ever-growing interest, especially in the control of shock-induced separation, which is a result of Shockwave Boundary Layer Interactions (SBLIs). SBLIs result in rapid retardation of the boundary layer, forcing it to thicken and possibly separate [49, 50, 51]. SBLIs are omnipresent in high-speed flows, increasing drag and flow unsteadiness on transonic wings [52, 53, 54], causing blade losses, decreased intake efficiency, and disturbed flow in the compressors of gas turbines [55, 56], separated boundary layers, flow unsteadiness and even engine unstart on supersonic [57, 58] and hypersonic inlets [59]. Therefore, controlling the SBLIs in external and internal flows is crucial for high-speed applications [60].

McCormick [61] compared wheeler doublet-type MVGs with a passive cavity to control a large separation bubble induced by SBLI. The results showed that MVGs significantly suppress the separation bubble; they result in a significantly thinner boundary layer downstream of the shock and decreased boundary layer losses, with a boundary layer having a considerably lower shape factor. However, by suppressing the separation, MVGs cause the lambda foot to be weaker. The lambda foot shock system is an oblique shock system induced by separation, and it suffers less total pressure loss than a normal shock. In comparison, the passive cavity reduced the total pressure loss, however, with increased boundary layer losses. The considerable extension of the lambda foot shock system can explain this physically. The effects of both approaches on the lambda foot shock system can be seen in the sketches and total pressure measurements given in Figure 1.11. The author states that both control methods have advantages and disadvantages. For example, if the application is an airfoil aiming to reduce wave drag, a passive cavity is probably the best option among the two. If the application is a supersonic diffuser, MVGs seem to be the best choice since they can successfully reduce the separation induced by SBLI, allowing more pressure recovery, which can also compensate for the increased shock loss. Mounts and Barber [62] conducted an accompanying CFD study with a ramp-type MVG at a Mach number of 1.4. Although it is impossible to directly compare the two studies, the CFD study supports the experimental results, showing a significant reduction in the separation bubble size, resulting in a more rapid pressure recovery.

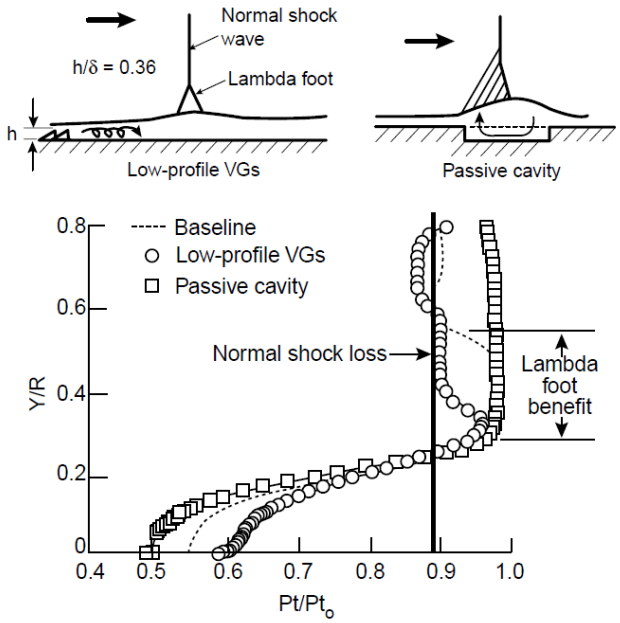

Figure 1.11 Total pressure ratio through the boundary layer. Y is the wall-normal distance, and R is the local radius of the test section, obtained 20δ downstream of the shock system (image reconstructed by Lin [41] from [61]).

Lee and Loth [63] conducted an extensive numerical study on various types of MVGs for controlling SBLI at Mach 3, employing Monotone Integrated Large Eddy Simulations. They have concluded that the vortices generated by MVGs can partially eliminate the flow separation induced by the shock and that they are able to move further downstream to entrain momentum flux, resulting in a boundary layer recovery. Among the MVG types they have studied, namely ramp-type (including half width and half height), vane-type, split ramp-type, and thick vane, the ramp-type MVG resulted in thinner downstream displacement thickness; however, they have generated the weakest vortices as they decayed faster compared to the others. Moreover, they have compared their results for both vane and ramp-type MVGs with the results of Ashill *et al.* [43], which is a study conducted under a zero pressure gradient at subsonic freestream velocities. The comparison of the vortex core trajectory showed that the subsonic data followed virtually the same non-dimensional trajectory up to x/h=20. After this position, the trajectories from the subsonic data continue to rise contrary to their supersonic counterparts, as an impinging shockwave is present for the supersonic case tilting the MVG wake.

Supersonic inlet performance is highly related to the development of the boundary layer through the inlet. Anderson *et al.* [64] studied the design of three different MVG arrays having h/δ ratios of 0.25 to 0.4 for a supersonic inlet using the results from experiments and CFD at Mach 2. They have employed the Design of Experiments methods for the optimization. All three devices had comparable effects with boundary layer bleed. Moreover, MVGs resulted in boundary layers that can withstand an SBLI. The authors concluded that ramp-type MVGs are the most practical option since they are fail-safe, mechanically robust, and affordable. An agreeing study was conducted by Herges *et al.* [65]. They have used an array of ramp-type MVGs in order to control the SBLI for a supersonic inlet at Mach 1.4. They have concluded that ramp-type MVGs can enhance the boundary layer that is already controlled by bleed; moreover, they can even replace the bleed altogether. Babinsky *et al.* [66] studied the effects of counterrotating vane-type MVGs having an h/δ ratio of 0.2 on the performance of a mixed compression inlet at Mach 1.3 and 1.5. The results showed that MVGs are able to reduce the separation size significantly in all conditions. However, it was found that with increasing Mach number, the separation control effectiveness of the MVGs was reduced. The authors state that MVGs might be used for supersonic inlets to reduce the bleed requirements, thus increasing the inlet performance. Oorebeek *et al.* [67] conducted an experimental study using Laser Doppler Anemometry (LDA) to compare the effects of MVGs and bleed on supersonic boundary layers at Mach numbers 1.5 and 1.8. MVGs resulted in similar increases in skin friction coefficients with bleed. Considering that the bleed system removed up to 10% of the incoming mass flow from the boundary layer, MVGs offer a better solution in this case. Baruzzini *et al.* [68] also studied the application of MVGs for supersonic inlets. Their numerical study employed vane-type and ramp-type MVGs alongside a porous bleed at Mach numbers of 2 and 2.5. The results showed that the effect of the bleed limited the vortex lift-off characteristics of vane-type MVGs, whereas the ramp-type MVGs performed better in that manner as the vortices they created transferred high-energy fluid to the targeted region of the boundary layer. However, for both types of MVGs, it was suggested that the MVGs should not be placed on porous surfaces since the

bleed degraded their effects. When placed on a solid wall, vane-type MVGs exceeded the performance of their ramp-type counterparts of equal heights. However, the authors noted that as the vane-type MVGs are susceptible to thermal erosion due to excessive aerodynamic loading, they might create potential foreign object damage, whereas the ramp-type MVGs are thought to be more durable to these effects. Ghosh *et al.* [69] conducted a numerical study at Mach 2.5 on the effects of ramp-type MVGs on SBLI employing a Reynolds Averaged Navier Stokes (RANS) based method with a k-ω model. They have utilized immersed-boundary methods to simulate the high-speed flow over the MVG with fewer grid points than body-fitted grids. The numerical results were compared with the LDA measurements of Babinsky *et al.* [50]. They have concluded that using RANS with an immersed-boundary model is applicable to simulate the flow over an MVG array as their numerical predictions are validated with the experimental results.

Researchers also focused on the wake structures of MVGs, especially the ramp-type MVGs. The Large Eddy Simulations (LES) study by Li and Liu [18] focused on the separation control created at a supersonic ramp, a prototype SBLI problem that often exists in supersonic inlets. They have recorded agreeing results with the previous studies, as the MVG reduced the separation significantly and improved the shape factor. Through the LES, they have reported new findings on the control mechanism of ramp-type MVGs, vortex rings generated through the action of Kelvin-Helmholtz (K-H) instability. The vortex rings were found to strongly interact with the separation zone and separation shock, playing an essential role in the flow control mechanism of ramp-type MVGs. Vortex rings appear in the immediate downstream of the MVG and grow in size and become more irregular further downstream, while the streamwise vortex pair becomes weaker and eventually decays at a particular downstream position. Sun *et al.* [70] investigated the three-dimensional instantaneous flow characteristics in the near wake of a ramp-type MVG having an h/δ ratio of 0.66 at Mach 2 employing tomographic PIV. The mean results agreed with the previous studies as the counterrotating vortex pair is produced and lifted off from the wall further downstream. The instantaneous flow structure showed a train of arc-shaped vortices generated through the action of Kelvin Helmholtz (K-H)

instability, which occurs in the shear layer that bounds the wake. The presence of vortices created by K-H instability affects the instantaneous flow as the K-H vortices interact with the streamwise vortex pair, rendering the instantaneous wake rather complex. In a following study [71], they investigated the decay of the wake of two ramp-type MVGs having h/δ ratios of 0.57 and 0.77. The comparison of the height of MVGs showed that the larger MVG created stronger streamwise vortices, resulting in a stronger upwash. Moreover, larger MVGs created higher minimum streamwise and wall-normal velocity components with a slower wake recovery, meaning that the wake created by a larger MVG persists more than that created by its smaller counterpart. They have also proven that the wake of an MVG collapses into a single curve in terms of streamwise velocity, wall-normal velocity, and turbulent quantities, showing that the wakes of MVGs are self-similar. Another study [72] by the same research group compared the tomographic PIV results with the numerical results employing Implicit Large Eddy Simulations (ILES). They used the same ramp-type MVG with an h/δ ratio of 0.8 at Mach 2. The ILES results compared well with the experimental results for the streamwise velocity component, with the ILES results predicting a faster wake recovery. For the wall-normal component, the ILES results estimated the peak velocity to be $0.24U_\infty$, whereas the experiments showed the same peak as $0.34U_\infty$. The results indicated that the presence of K-H vortices vigorously undulates the shear layer that bounds the MVG wake. The K-H vortices, as they interact with the streamwise vortex pair, develop from an arch shape to a full ring shape in the far wake. These studies, in conclusion, clarify the presence of the K-H vortices in the ramp-type MVG wake. To consolidate their studies and previous descriptions by Babinsky *et al.* [50] and Li and Liu [73], they have suggested a conceptual model describing the ramp-type MVG wake in terms of the evolution of the vortical organization (Figure 1.12). In this conceptual model, the streamwise vortex pair is shown as focused filaments that occur in the immediate downstream of the MVG. However, as the curved shear layer around the wake rapidly becomes unstable, arch-shaped K-H vortices are generated. As the wake progresses, the leg portions of the arch-shaped K-H vortices extend to the lower side of the wake by the action of the streamwise vortices, eventually forming a vortex

ring (as shown in the lower right of the conceptual model). The vortex ring breaks down as they are subjected to turbulent distortion.

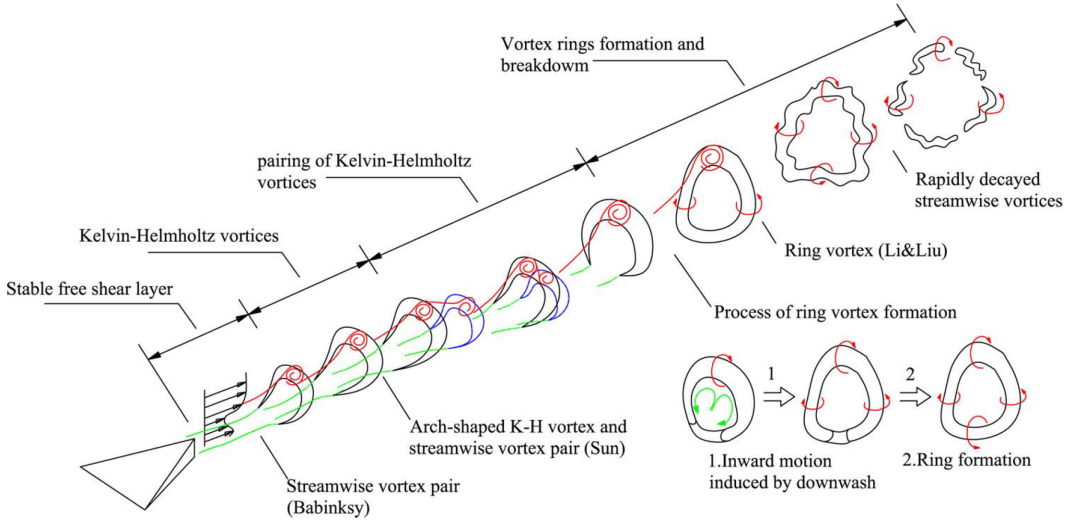

Figure 1.12 Conceptual model for the vortical organization in the ramp-type MVG suggested by Sun [71].

Giepman [74] experimentally studied the effects of the location and the size of ramp-type MVGs on the oblique shockwave reflection, the criterion of effectiveness being the size of the shock-induced separation bubble and reflected shock unsteadiness. They have used MVGs with h/δ ratios of 0.38, 0.56, and 0.77 for their PIV measurements. The larger MVGs were more effective in reducing the area of shock-induced separation than the smallest MVG, as they reduced the area of separation up to 87%. Larger MVGs were also effective at reducing the reflected shockwave unsteadiness. However, they state that caution must be taken as with increasing MVG height, the drag force increases. They have investigated the momentum added to the near-wall region by calculating the momentum flux contained in the region having a height up to 43% of the boundary layer thickness, where the separation bubble is most sensitive to the momentum flux. The results showed that the added momentum flux by ramp-type MVGs scaled linearly with their height since the device Reynolds number values of the MVGs used are well above 1400 (Figure 1.10). Their follow-up study [75] investigated the effects of Mach and Reynolds numbers on the wake of ramp-type MVGs. This parametric study investigated a range of Mach numbers (1.5 to 2.5) and Reynolds numbers (28×10^6 m^{-1} to 63×10^6

m^{-1}). It was found that most of the flow features of the wake, namely, the wake height, wake strength, vortex core height, and the added momentum flux, were scaling linearly with the device height. The control effectiveness of the ramp-type MVGs was reduced with the increasing Mach number since the added momentum flux to the near-wall region is reduced due to the weaker streamwise vortices, consistent with the results of Babinsky *et al.* [66]. The Reynolds number had no effect on the wake flow features. However, a slight effect was recorded as the mixing was increased at higher Reynolds numbers, shown by the slight decrease in the shape factor. The shape factors were 1.21 and 1.18 for freestream Reynolds numbers of $28x10^6$ m^{-1} and $63x10^6$ m^{-1}, respectively.

1.3 Objectives and Scope

This study investigates the wake flows generated by ramp-type MVGs in subsonic flows and compares the findings with those in supersonic flows that are available in the literature to explore the similarities between the two flow regimes. In order to do that, the undisturbed boundary layer is characterized utilizing hot-wire anemometry to determine the device heights. Then, the wakes generated by three ramp-type MVGs having the same design but different heights (i.e., different h/δ ratios) are investigated experimentally using the two-dimensional two-component Particle Image Velocimetry (2D2C PIV) technique.

A three-dimensional numerical study is conducted, which complements the two-dimensional results of the 2D2C PIV experiments and enhances the range of h/δ ratios with two more MVGs with increased device heights. After the validation of the numerical study with the experimental results and after the addition of two more MVGs utilizing the numerical simulations, the effect of device height is investigated in terms of the velocity components, the out-of-plane vorticity component, streamwise vorticity component, and various decay parameters for five different h/δ ratios ranging from 0.18 to 0.54. The wake decay features of MVGs are also investigated in spanwise planes in terms of the velocity components, allowing the examination of the three-dimensional influence of the MVGs in the wake and the effect of h/δ on that. Moreover, the similarities between the subsonic and supersonic wakes are discussed regarding the wake decay parameters.

With the experimental and numerical simulation results established, a wake model for the ramp-type MVGs is constructed using the self-similarity of the wake and various decay parameters. In order to do that, first, the self-similar behavior of the ramp-type MVG wake is examined in terms of streamwise and wall-normal velocity components. Then, a wake model is constructed by employing the self-similarity of the wake and the decay parameters, such as the decay of the maximum velocity deficit and the maximum upwash velocity and their positions. The wake model, which is constructed employing the results of experimental measurements and

numerical simulations conducted in subsonic regimes, is then used to reconstruct the wakes of ramp-type MVGs in supersonic flow conditions in terms of streamwise and wall-normal velocity components at various streamwise positions. Moreover, utilizing the difference in the decay characteristics of larger MVGs, a method to designate the limit between MVGs and conventional (δ-scale) vortex generators is suggested.

1.4 Thesis Outline

Chapter 1 presents the introduction, starting with the definition of boundary layer control with examples of applications from the literature with emphasis on conventional (δ-scale) vortex generators. The introduction continues with the utilization of MVGs for boundary layer control in various applications for supersonic and subsonic regimes. Chapter 2 describes the experimental facilities and the measurement techniques employed along with the undisturbed boundary layer and resulting MVG design and production. Chapter 3 investigates the wake characteristics of ramp-type MVGs experimentally. The numerical case is described in Chapter 4, along with the validation of the numerical results with their experimental counterparts. Chapter 5 investigates the decay of ramp-type MVGs and the effect of height on the wake, employing the numerical simulation results. Moreover, the decay characteristics of ramp-type MVGs in subsonic flow regimes are compared with their supersonic counterparts. A wake model named the Ramp-Type MVG Wake Model is presented in Chapter 6 with reconstructions of ramp-type MVG wakes in supersonic conditions in terms of streamwise and wall-normal velocity components using the model. Finally, Chapter 7 presents the conclusions of this study.

CHAPTER 2

EXPERIMENTAL SETUP

This chapter introduces the experimental setup and the measurement methods in order to characterize the MVGs.

2.1 Wind Tunnel Facility

Experiments were conducted in the METUWIND C3 (Figure 2.1) open-return suction-type boundary layer wind tunnel located at METU Center for Wind Energy (RÜZGEM), which has a test section of 1 x 1 x 8 m^3 (height x width x length), allowing for measurements with relatively large boundary layer thickness. The maximum velocity of the METUWIND C3 is 25 m/s with an average turbulence intensity of 0.35% at the inlet.

Figure 2.1 Open-return suction-type boundary layer wind tunnel (METUWIND C3) at METU Center for Wind Energy Research (RÜZGEM).

The wind tunnel is controlled via an in-house developed close-loop LabVIEW code, allowing the tunnel to be operated with constant Rotations per Minute (RPM), constant Reynolds number, and constant velocity. Figure 2.2 shows a sketch of the METUWIND C3 wind tunnel, the instruments, the sensors used for the control system, the MVG, and its approximate field of view (FOV). The wind tunnel is instrumented with static pressure taps (8 in total) at two locations on the contraction

cone surface, and the pressure difference is measured through a 4-20 mA pressure transmitter. A pitot-static tube is mounted inside the test section on top of the MVG to measure the static and total pressure of the incoming flow. A 16-channel pressure scanner is employed for the pitot-static pressure measurements. The air temperature and humidity are measured at the end of the test section. The atmospheric pressure is monitored by employing a handheld barometer. For the experiments, the wind tunnel is used in constant velocity mode. For that, the wind tunnel is calibrated at different fan RPM values while the measurement devices and the MVGs are placed inside to take the blockage effects into account. A separate calibration is performed for each MVG.

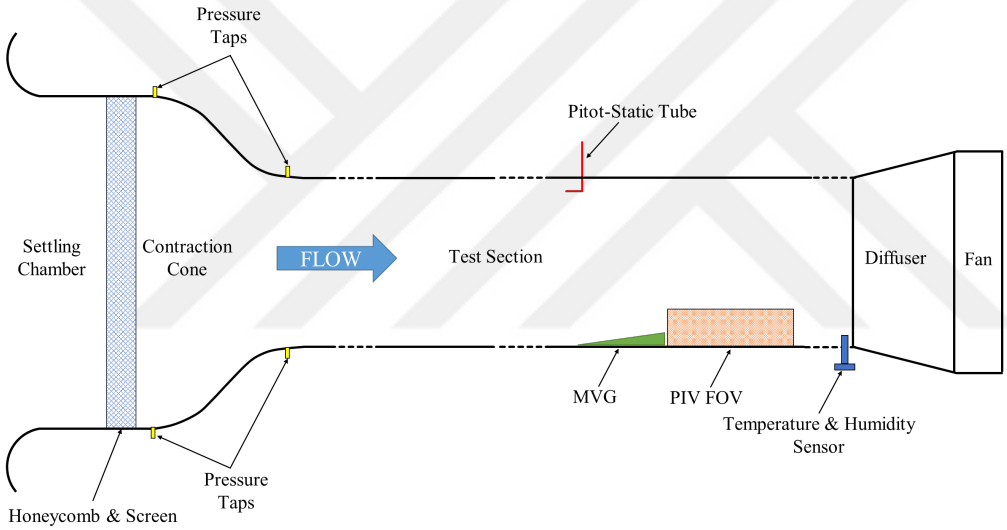

Figure 2.2 Sketch of the METUWIND C3 wind tunnel, including the MVG and the instruments and sensors for the close-loop control system.

2.2 Undisturbed Boundary Layer Measurements

Undisturbed boundary layer measurements are conducted to determine the boundary layer thickness upstream of the MVG at a freestream velocity of 10.1 m/s. The results of the measurements were then employed to design the MVGs used and the numerical simulation work done within this study.

Figure 2.3 shows the sketch of the undisturbed boundary layer measurements setup and the coordinate system. These measurements are conducted via hot-wire anemometry without the presence of any MVGs and without any elements to alter the boundary layer. A single-wire, 90° angled (L-type) hot-wire probe is placed 6.2 m downstream of the inlet, corresponding to a position 7 mm upstream of the leading edge of the MVG for the PIV measurements. This location is selected to let the boundary layer develop and have a relatively higher thickness, allowing to conduct measurements for a range of MVGs with different heights for which the smallest is producible. The boundary-layer hot-wire probe is traversed over a distance of 210 mm in the wall-normal direction (y-axis), the first measurement point being 10 mm away from the bottom wall of the wind tunnel. The first 100 mm is covered with a step size of 1 mm, and the rest is covered with a step size of 2 mm. The velocity data is collected at a sampling rate of 10 kHz for a sampling time of 30 seconds at each measurement step.

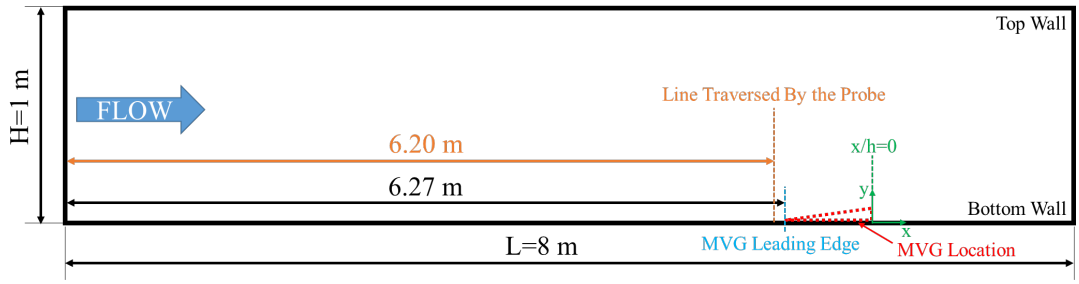

Figure 2.3 Sketch for the undisturbed boundary layer measurements

The boundary layer profiles in terms of velocity and turbulence intensity are shown in Figure 2.4. Due to the fact that hot-wire probes are sensitive to the inclination of the incoming flow [76], the velocity in Figure 2.4 is denoted as U_{eff}, which is the

effective hot-wire cooling velocity. However, since the hot-wire probe employed for the undisturbed boundary layer measurements was placed parallel to the bottom wall of the wind tunnel and well downstream of the wind tunnel inlet, the effective hot-wire cooling velocity was assumed to be equal to the streamwise velocity.

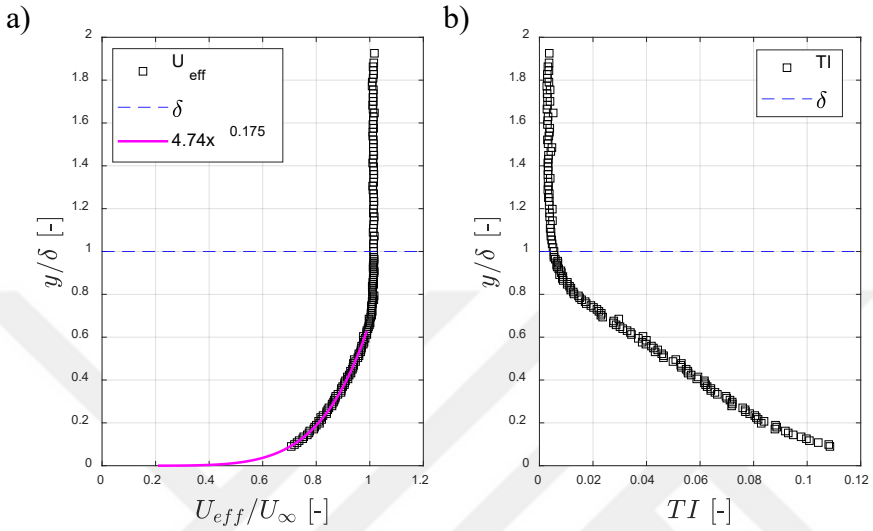

Figure 2.4 Results of the undisturbed boundary measurements (a) Streamwise velocity distribution of the undisturbed flow. (b) The turbulence intensity distribution of the undisturbed flow.

In Figure 2.4 (a), the streamwise velocity is normalized by the freestream velocity, and the wall-normal distance is normalized by the resulting boundary layer thickness, estimated to be 111.3 mm from the bottom wall. The boundary layer thickness is estimated using the velocity gradient profile in the wall-normal direction after applying a running-average filter to the velocity profile with a kernel size of 9 data points. A power-law fit is also included in Figure 2.4 (a). The resulting boundary layer thickness (δ), as well as the other boundary layer parameters, displacement thickness (δ^*), momentum thickness (θ), shape factor (H), momentum thickness Reynolds number, and friction velocity (U_τ) are calculated and tabulated in Table 2.1. The equations used for the calculation of the boundary layer parameters are given in equations 2.1 to 2.6.

Displacement thickness:

$$\delta^* = \int_0^{\delta} \left(1 - \frac{U_{eff}}{U_\infty}\right) dy \quad [2.1]$$

Momentum thickness:

$$\theta = \int_0^{\delta} \frac{U_{eff}}{U_\infty}\left(1 - \frac{U_{eff}}{U_\infty}\right) dy \quad [2.2]$$

Shape factor:

$$H = \frac{\delta^*}{\theta} \quad [2.3]$$

Momentum thickness Reynolds number:

$$Re_\theta = \frac{\rho U_\infty \theta}{\mu} \quad [2.4]$$

Friction velocity:

$$U_\tau = \sqrt{\tau/\rho} \quad [2.5]$$

Where τ is the wall shear stress, calculated by using the velocity gradient:

$$\tau = \mu \frac{dU}{dy} \quad [2.6]$$

Table 2.1 Undisturbed boundary layer properties

δ [mm]	δ^* [mm]	θ [mm]	H	Re_θ	U_τ [m/s]
111.31	8.11	6.74	1.2	4016	0.36

Figure 2.5 illustrates the dimensionless velocity (U^+), the velocity normalized by the friction velocity (U_τ), and the length scale y^+, calculated using Equation 2.7. It can be seen that the region of y^+=350 to 2500 of the undisturbed boundary layer profile is resolved utilizing the hot-wire anemometry (HWA) measurements.

$$y^+ = \frac{yU_\tau}{\nu} \qquad [2.7]$$

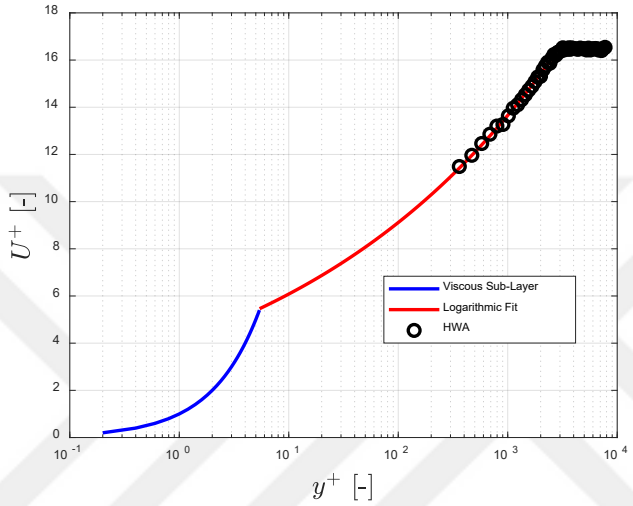

Figure 2.5 Dimensionless streamwise velocity of the undisturbed boundary layer.

2.2.1 Design of the Micro Vortex Generator

The ramp-type MVGs used in this study have the same design used by Sun [77], which follows the micro-ramps suggested by Anderson [78]. Three MVGs having heights of 20 mm, 30 mm, and 40 mm, named MVG2, MVG3, and MVG4, respectively, are used in this study. All of the MVG models used for experimental work are 3-D printed in RÜZGEM (METU Center for Wind Energy Research). Dimensions of all MVGs and corresponding h/δ ratios are given in Table 2.2, where δ is the boundary layer thickness as measured by the undisturbed boundary layer measurements. Figure 2.6 shows the sketch for the MVG design and CAD models of MVGs used in this study, along with 3-D printed MVGs.

Table 2.2 MVG dimensions and their corresponding h/δ ratios.

MVG	h	w	c	α	h/δ
Design	-	6.1h	6.9h	24°	-
MVG2	20 mm	122 mm	138 mm	24°	0.18
MVG3	30 mm	183 mm	207 mm	24°	0.27
MVG4	40 mm	244 mm	276 mm	24°	0.36

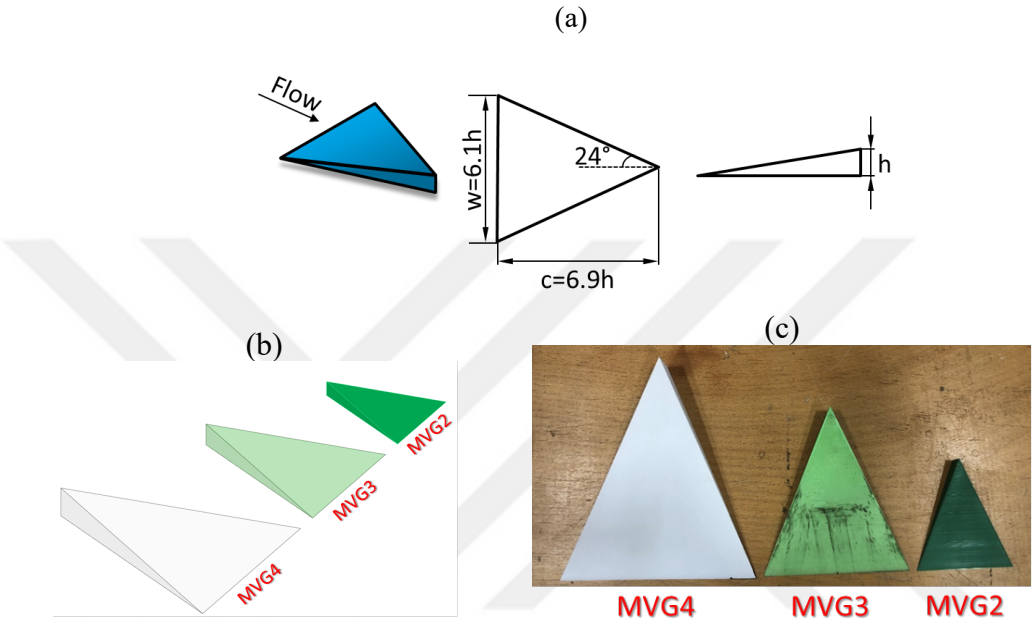

Figure 2.6 (a): The sketch for the MVG design (b): CAD models of MVGs used. (c): 3-D printed MVGs.

2.3 Measurement Details

Two-dimensional two-component Particle Image Velocimetry (2D2C PIV) measurements are conducted downstream of the MVGs in a streamwise-oriented plan aligned with the central axis of the MVG. The components used in the measurements are summarized in Table 2.3. The PIV setup consists of a New Wave Research Solo 120XT Nd:YAG 532 nm laser, a Phantom V640 high-speed camera equipped with a Nikon Nikkor 60 mm lens, and a Dantec Dynamics timer box. The laser beam emitted from the laser head parallel to the z-direction and directed upwards parallel to the y-direction employing a mirror (Figure 2.7). Then, the beam passes through a spherical and a cylindrical lens to be converted into an

approximately 1 mm thick laser sheet, focused in a region that covers the camera's field of view. The flow is seeded with fog of droplets with a mean diameter of 1 µm, created by employing a SAFEX fog generator. The time between the two laser pulses is defined as 70 μs, and the repetition rate is selected to be 10 Hz.

The laser head, camera, and spherical and cylindrical lenses are mounted on a three-axis heavy-duty traverse system, allowing the setup to be traversed to acquire more windows. The setup is traversed in streamwise (x) and wall-normal (y) directions for MVG3 and MVG4 to acquire eight windows total, whereas it is traversed only in the streamwise (x) direction for MVG2 to acquire four windows since the shear layer created by MVG2 is captured in the first wall-normal row of windows. The resulting fields of view for all three MVGs are shown in Figure 2.8 in dimensionless distance units of x/h and y/h for each MVG. The windows are acquired such that there are 5% and 10% overlap regions between the neighboring windows in the streamwise and wall-normal directions, respectively. The limits in both streamwise (x) and wall-normal (y) directions in terms of device heights get smaller with increasing device height due to the placement of MVGs 6.2 meters downstream of the wind tunnel inlet. That is why the experimental campaign is limited to MVG4, having a device height of 40 mm.

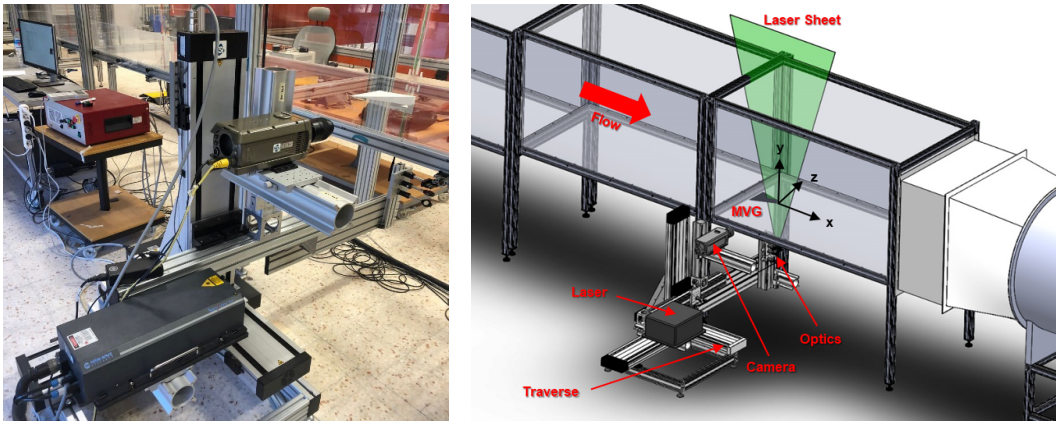

Figure 2.7 A photograph and a sketch of the PIV setup. Showing the traverse, the camera, laser, and the optics with the placement of MVG in the wind tunnel, including the coordinate system used.

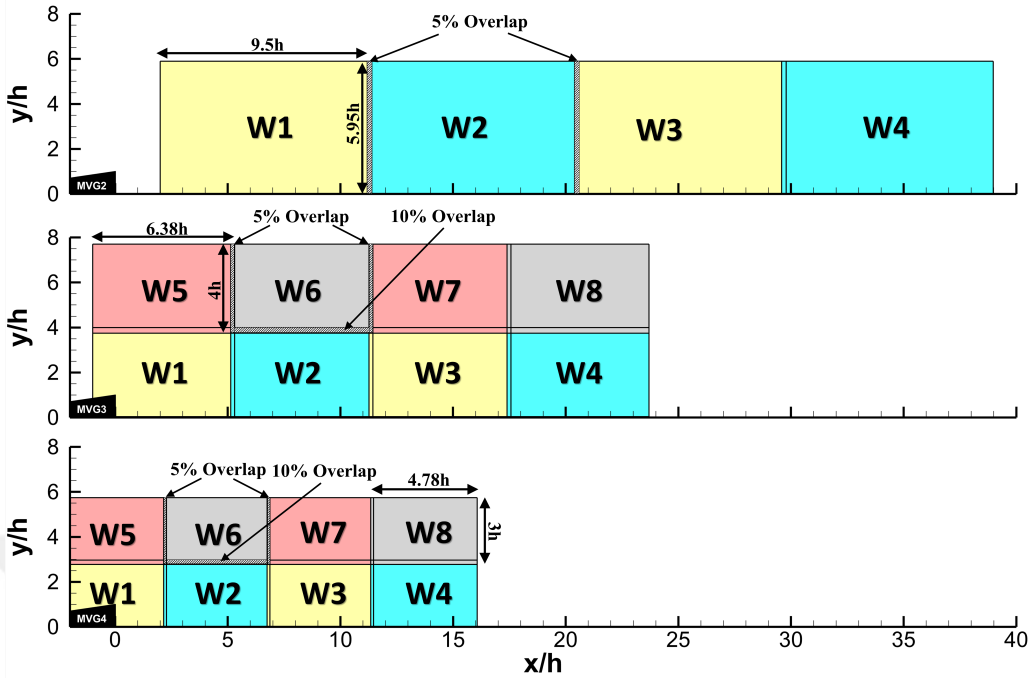

Figure 2.8 PIV measurement domain showing the windows with the overlap regions and fields of view dimensions for MVG2, MVG3, and MVG4.

A thousand double-frame particle images are acquired and preprocessed by applying opening, closing, and median filters to improve image quality and remove background noise for each window. Image masking was applied to mask the MVGs since they presented obstructions in the field of view. Then, using a two-step adaptive correlation analysis with the final interrogation window of 64x32 pixels^2 and 50% overlap, vector spacings of 1.2 mm along the streamwise direction and 0.6 mm along the wall-normal direction are obtained in the resulting vector maps. The vector fields are then stitched to provide a clear picture of the flow pattern in the wake of the MVGs.

Table 2.3 Components of the 2D2C PIV measurements.

Laser Sheet	Laser Type	Nd:YAG
	Manufacturer	New-Wave Research
	Model	Solo 120XT
	Maximum Energy	120 mJ/pulse
	Wavelength	532 nm
	Thickness	~1 mm
Optics	Mirrors	Dielectric Mirror
	Spherical Lens	Plano-convex, Focal Length: 500 mm
	Cylindrical Lens	Plano-concave, Focal Length: -12.4 mm
Camera	Model	Phantom V640
	Sensor Type	CMOS
	Sensor Resolution	2560x1600 $pixel^2$
	Sensor Size	25.6x16 mm^2
	Pixel Pitch	10 μm
	Pixel Depth	12 bits
	Maximum Repetition Rate	1400 fps @ Full resolution 2500 fps @ 1920x1080
	Internal Memory Buffer	16 GB
Camera Lens	Manufacturer	Nikon
	Focal Length	60
	f#	2.8
Seeding	Type	Fog
	Nominal Diameter	1 μm
	Generator	SAFEX

CHAPTER 3

WAKE CHARACTERISTICS OF MICRO VORTEX GENERATORS

This chapter investigates the wake characteristics of MVGs utilizing the results of 2D2C PIV measurements. The flow field properties investigated are streamwise velocity, wall-normal velocity, vorticity, streamwise and wall-normal velocity fluctuations, and Reynolds shear stress. These properties are presented in terms of contours and extracted profiles at various x/h locations in order to gain insight into the general characteristics of a ramp-type MVG wake.

As explained in the experimental setup chapter, the fields of view for the MVGs differ due to wind tunnel limitations. Therefore, profiles are extracted for MVG4 up to 15 device heights, MVG3 up to 20, and MVG2 up to 30 for all properties investigated in this chapter.

3.1 Decay of Time-Averaged Velocity Components

The flow fields created by the three MVGs were investigated regarding streamwise and wall-normal velocity components in both near and far-wake regions. Experimental results for MVG2, MVG3, and MVG4 are used to discuss the general characteristics of ramp-type MVGs.

3.1.1 Streamwise Velocity

The development and decay of the streamwise velocity component (U) normalized by the freestream velocity are shown in Figure 3.1 for MVG2, MVG3, and MVG4. The wake characteristics for all MVGs are quite similar, with some variations primarily due to the height difference. An example of these variations is the lift-off behavior characterized by the movement of the maximum streamwise velocity deficit

away from the wall. The lift-off behavior of MVG wake is distinctly seen in the contours for all three MVGs. However, it is seen that the lift-off is more pronounced with increasing MVG height. As the height increases, a velocity distribution with higher magnitudes is observed between the wall and the maximum deficit point. The contours also indicate that with increasing MVG height, a streamwise velocity distribution with higher magnitudes is observed between the wall and the maximum deficit point. This increase shows that high-momentum fluid penetrates more with larger MVGs to the near-wall region, indicating that stronger streamwise vortex pairs are created with larger MVGs. Moreover, a distinct shear layer, which divides the freestream flow and the wake and bounds the streamwise vortex pair between itself and the wall, is observed in all the contour plots. As the MVG height increases, the shear layer becomes more prominent as the angle at which the shear layer develops increases with increasing height, indicating a stronger turbulent mixing due to larger vortex pairs and increased coherent upwash motion [77].

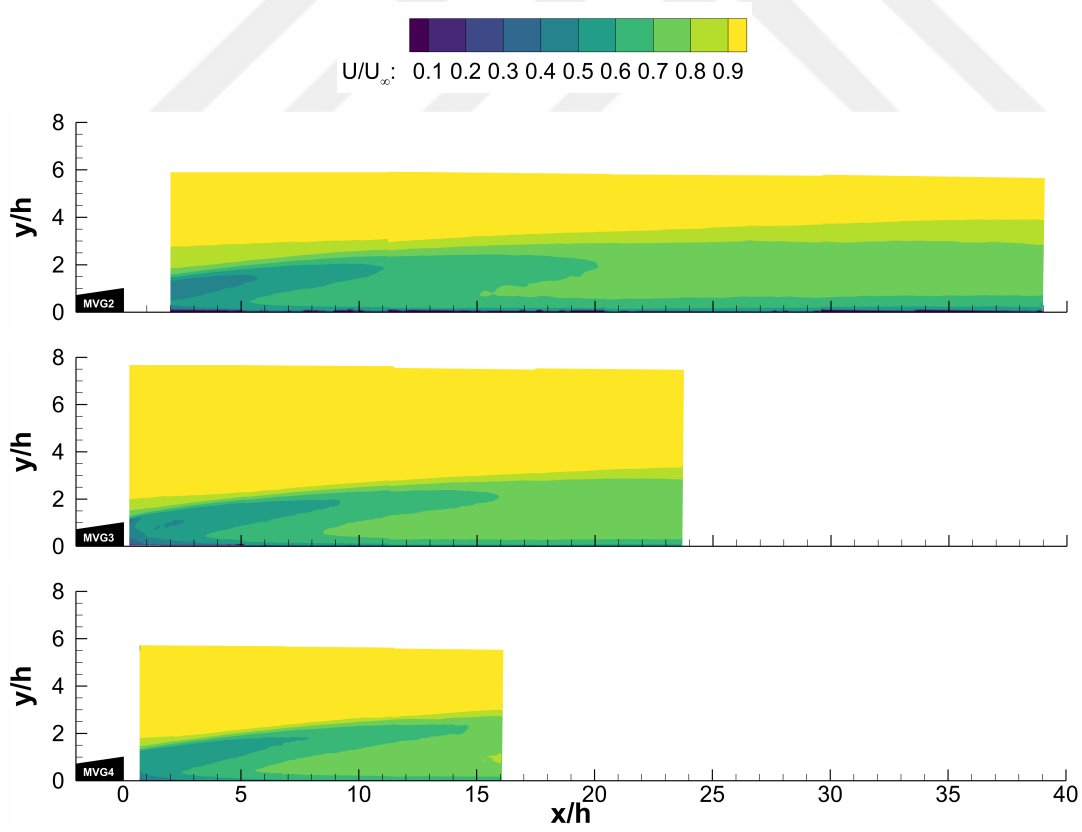

Figure 3.1 Contours of normalized streamwise velocity

In order to quantify the discussion above, wall-normal profiles are extracted from the 2D2C PIV data at four downstream stations, namely x/h=5, 10, 15, and 20 (Figure 3.2). The behavior of the streamwise velocity profiles for all the MVGs is similar, with some differences. For example, at x/h=5, the maximum velocity deficit is 48% for MVG2, 54% for MVG3, and 58% for MVG4, indicating that Figure 3.2 shows the streamwise evolution of normalized streamwise velocity profiles for each MVG. It can be observed that the location of the minimum streamwise velocity (i.e., maximum velocity deficit) shifts upwards for all three MVGs, caused by the upwash motion created by the streamwise vortex pair. The decaying wake further downstream is seen from the filled and flattened profiles. For example, at x/h=15, the maximum velocity deficit is 68% for MVG2, 70% for MVG3, and 71% for MVG4, indicating that the height effect starts to diminish further downstream, resulting in collapsing profiles as the wakes recover.

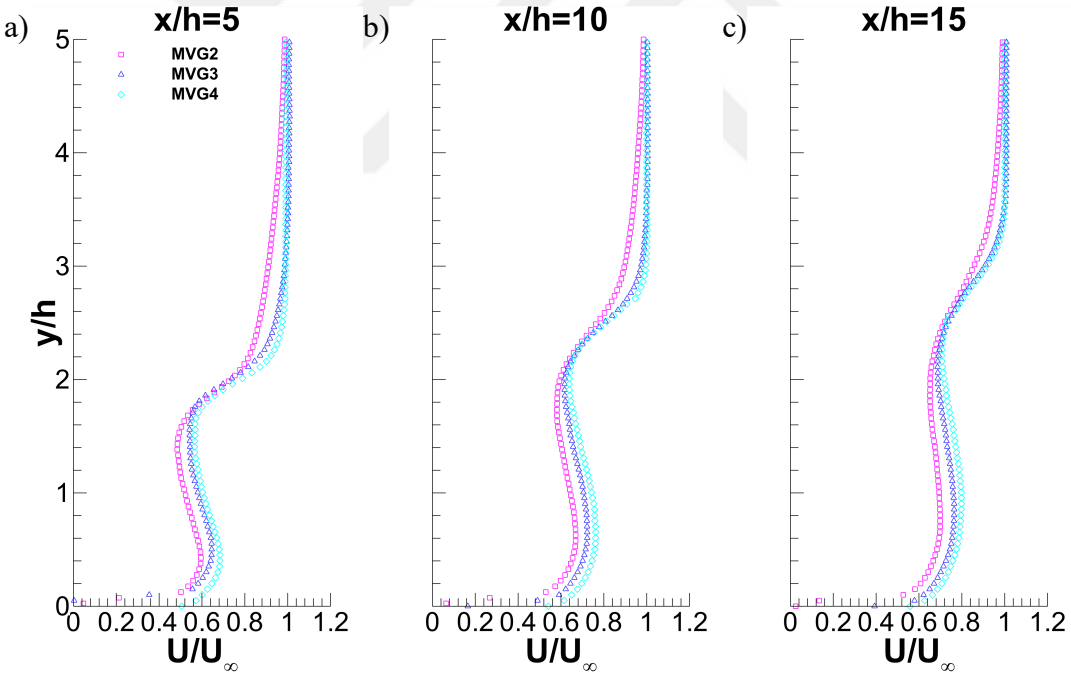

Figure 3.2 Profiles of normalized streamwise velocity at different downstream positions. a) x/h=5, b) x/h=10, c) x/h=15.

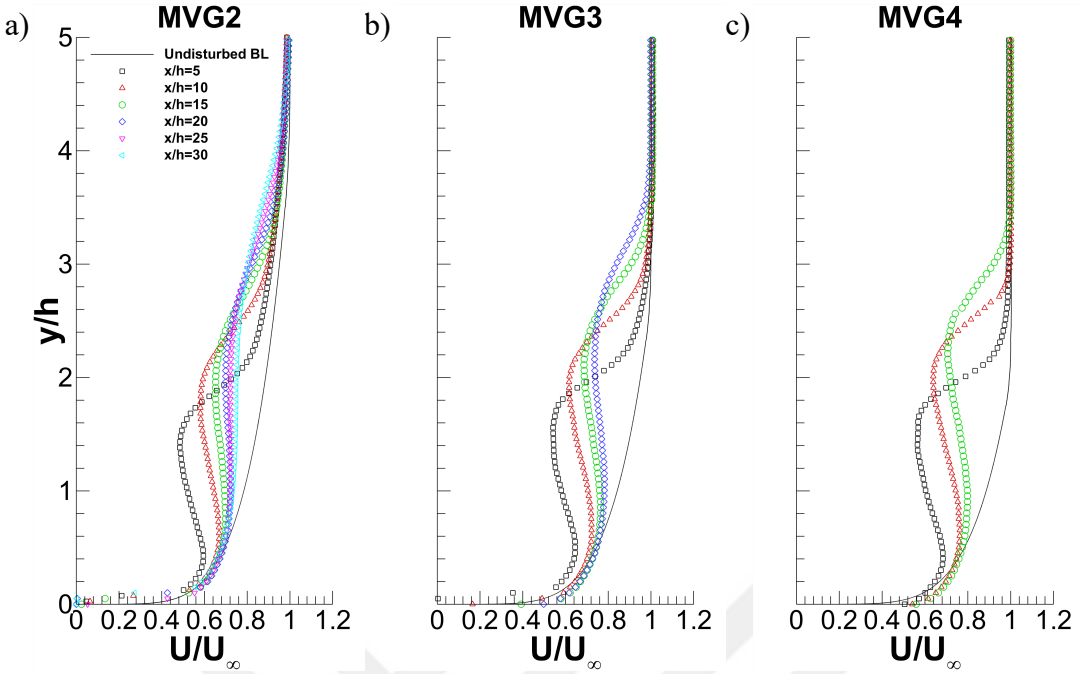

Figure 3.3 Streamwise evolution of normalized streamwise velocity profiles. a) MVG2, b) MVG3, c) MVG4.

3.1.2 Wall-Normal Velocity

Contours of wall-normal velocity normalized with the freestream velocity are given in Figure 3.4 for all three MVGs. The effect of MVG height is more pronounced in the wall-normal velocity contours, as they clearly display the upwash motion compared to the streamwise velocity contours. It is also seen from the wall-normal velocity contours that, with increasing MVG height, the magnitude of the wall-normal velocity in the wake is increased; this is more obvious just downstream the MVGs. In order to quantify the above discussion, wall-normal profiles are extracted from the 2D2C PIV data at four downstream stations, namely x/h=5, 10, 15, and 20, and shown in Figure 3.5. The wall-normal velocity profiles clearly show the MVG height effect, as the increasing MVG height results in an increased wall-normal velocity downstream of the MVG. The profiles at x/h=5 show this effect as the values of maximum wall-normal velocity are 25%, 32%, and 37% of freestream velocity for MVG2, MVG3, and MVG4, respectively, which in turn indicates that as the MVG height increases, the strength of the induced vortex pair, therefore, the mixing

effect generated by the MVG increases. As the wake recovery progresses, the wall-normal velocity profiles seem to collapse for all the MVGs downstream. The decreasing discrepancy of wall-normal velocity between the MVGs with different heights shows that the strengths of the upwash motions created become closer as the wake recovers further downstream. This comparison can also be made from Figure 3.6, as it shows the downstream progress of the wake for each MVG. At x/h=15, the values of maximum wall-normal velocity are 8%, 10%, and 12% of the freestream velocity for MVG2, MVG3, and MVG4, respectively, which indicates the diminishing height effect downstream as the wake decays. The recovery of the wall-normal velocity can be seen much better for MVG2 since more data is available downstream, as the percentage becomes 3% at x/h=35.

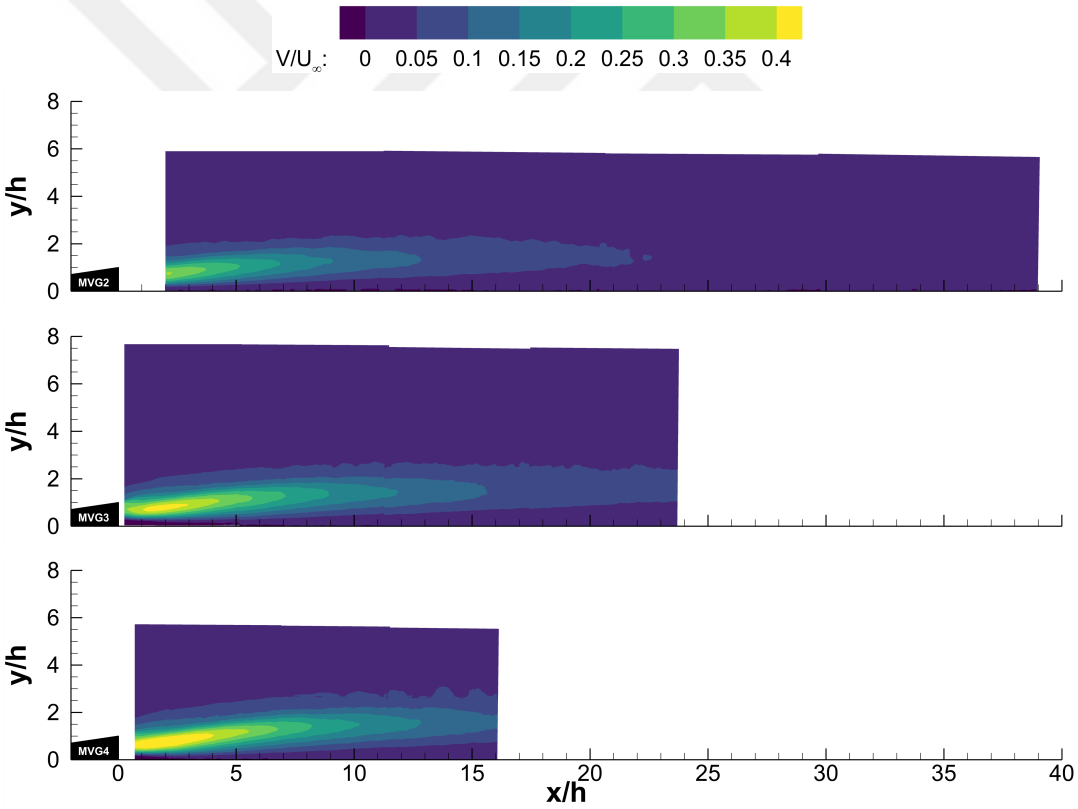

Figure 3.4 Contours of normalized wall-normal velocity.

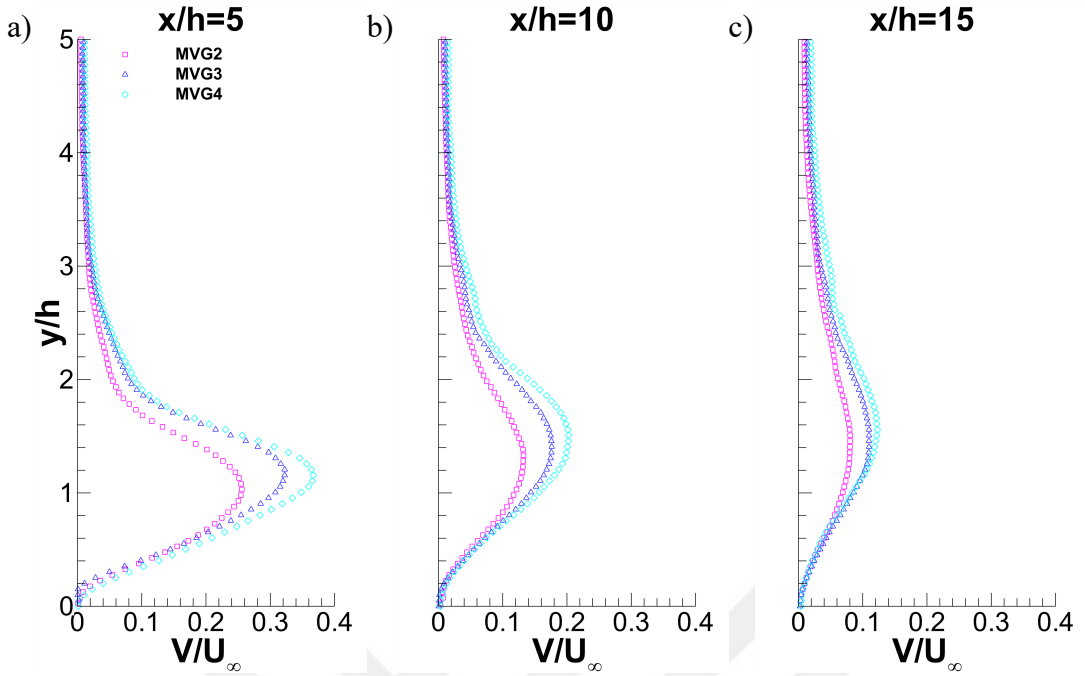

Figure 3.5 Profiles of normalized wall-normal velocity at different downstream positions. a) x/h=5, b) x/h=10, c) x/h=15.

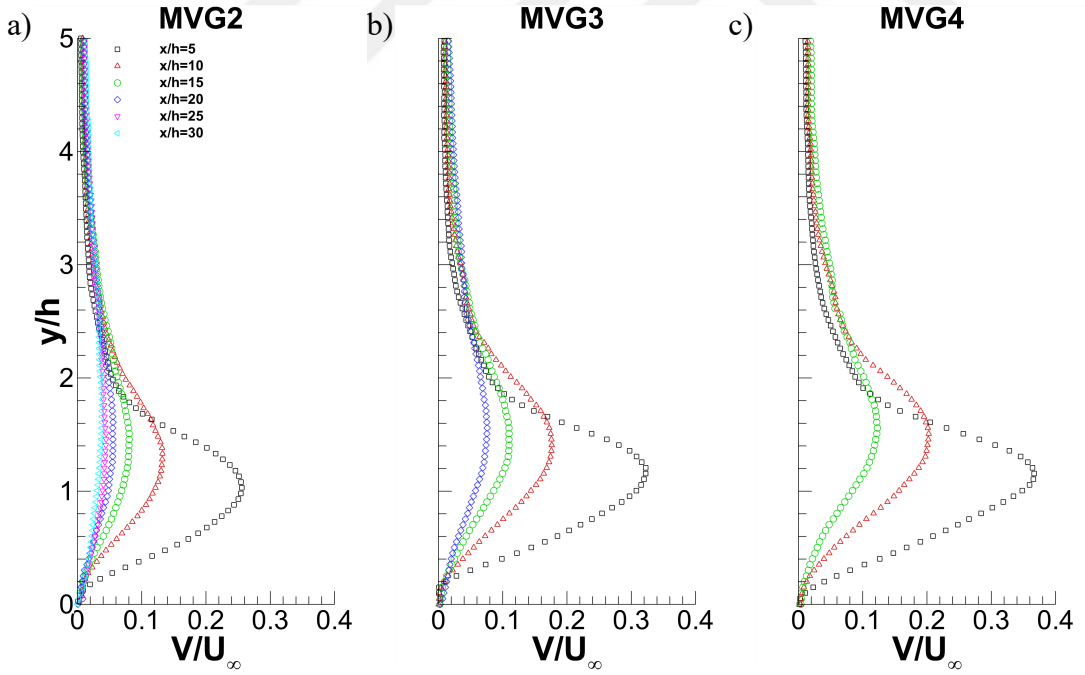

Figure 3.6 Streamwise evolution of normalized wall-normal velocity. a) MVG2, b) MVG3, c) MVG4.

3.2 Vorticity Distributions

Contours of out-of-plane vorticity (Ω_z) normalized by the height of MVGs and the freestream velocity are given in Figure 3.7. The increased vorticity levels are an indication of momentum transfer, which in turn shows the presence of mixing in the wake. Higher levels of vorticity are seen as the MVG height increases especially in the shear layer. At the near wake region, the level of negative vorticity is nearly doubled when the MVG height is doubled. However, as the flow progresses downstream, the vorticity levels of the MVGs at the shear layer start to equalize. This is clearly seen when the vorticity levels are compared for MVG2 and MVG4 at x/h=5 and 15 (Figure 3.8). The values of vorticity seem to be equalized for MVG3 and MVG4 at x/h=10, showing that such a height difference does not increase the mixing after a certain downstream distance. Figure 3.9 shows the streamwise evolution of the vorticity levels for each MVG. It can be seen that the peak negative level of vorticity is moving away from the wall, clearly indicating the upward movement of the wake. Further downstream, the profiles are flattened as the wake decays.

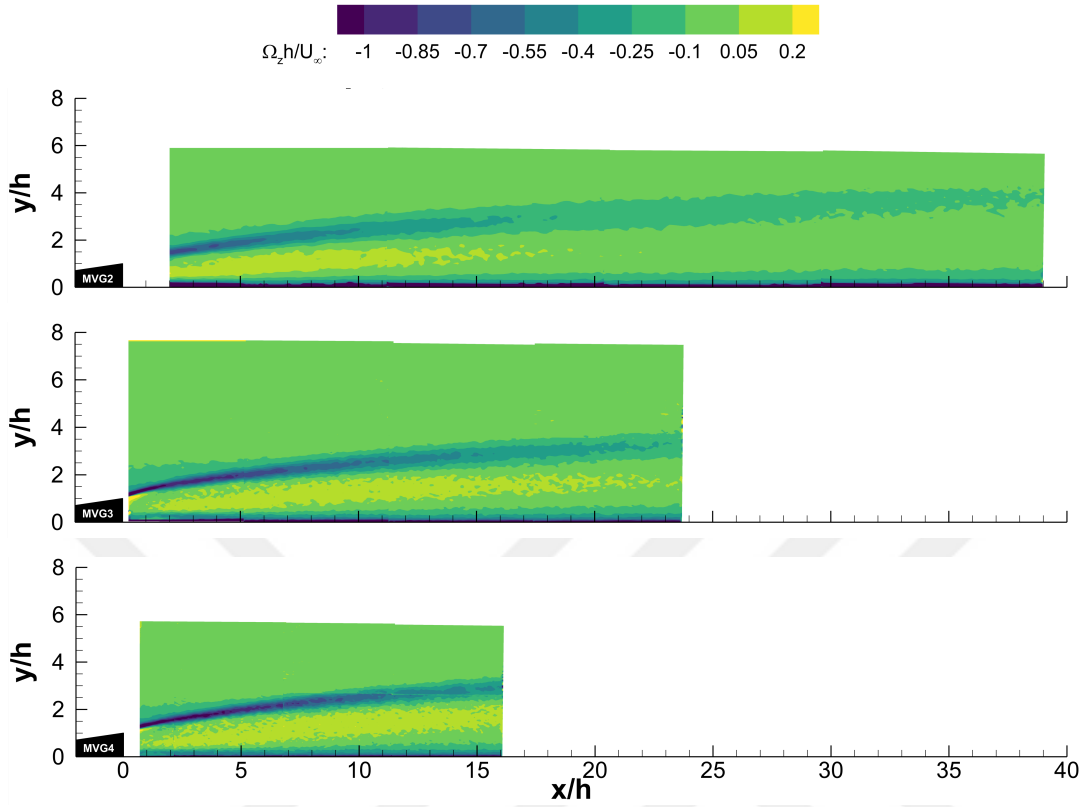

Figure 3.7 Contours of normalized out-of-plane vorticity.

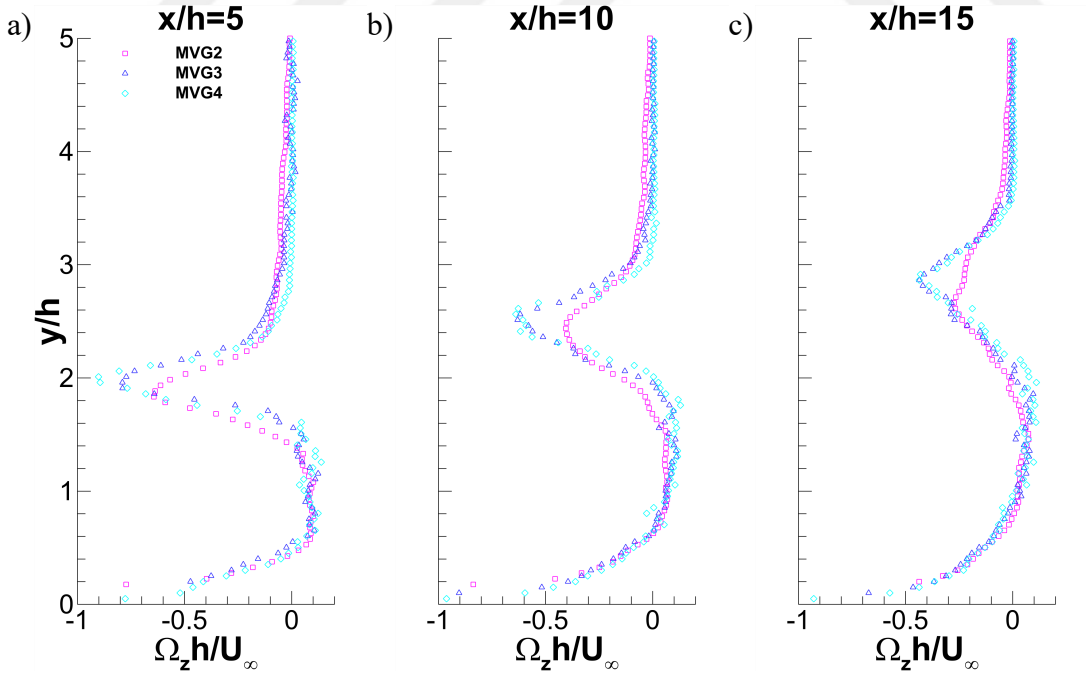

Figure 3.8 Profiles of normalized out-of-plane vorticity (Ω_z) at different downstream positions. a) x/h=5, b) x/h=10, c) x/h=15.

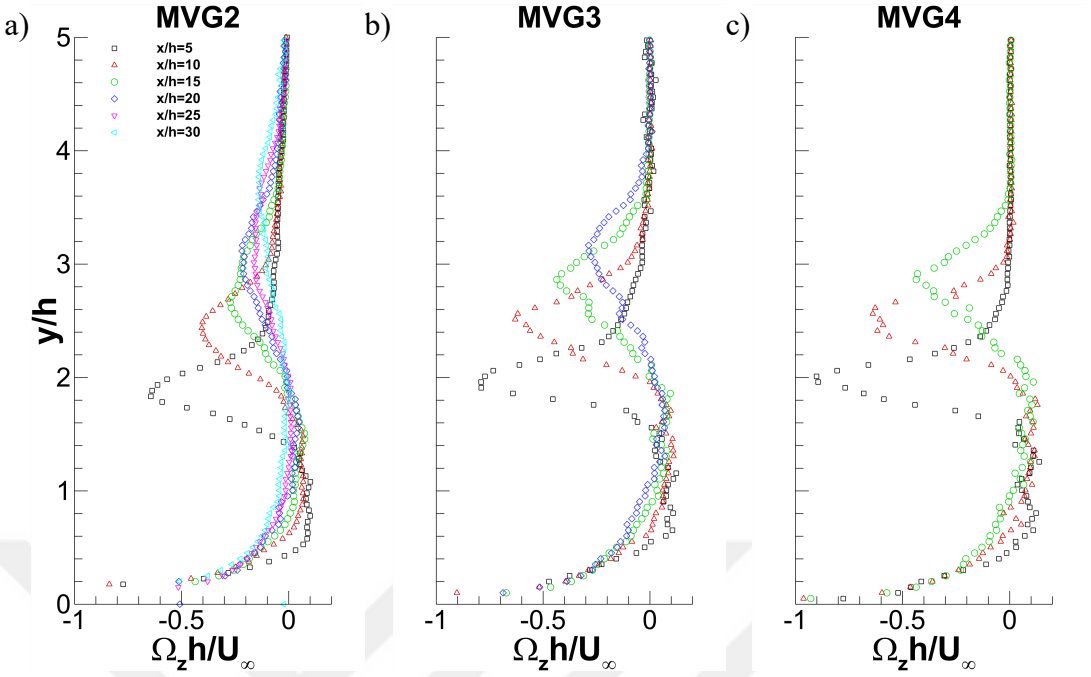

Figure 3.9 Streamwise evolution of normalized out-of-plane vorticity (Ω_z). a) MVG2, b) MVG3, c) MVG4.

3.3 Turbulence Properties

3.3.1 Velocity Fluctuations

Contours of streamwise and wall-normal velocity fluctuations normalized by the freestream velocity are seen in Figure 3.10 and Figure 3.11. The contours show that the velocity fluctuations follow the same lift-off trends that are seen in the velocity components. The contours also reveal the shear layer in the wake, with increased values of fluctuations concentrated in the region where the shear layer is expected to be.

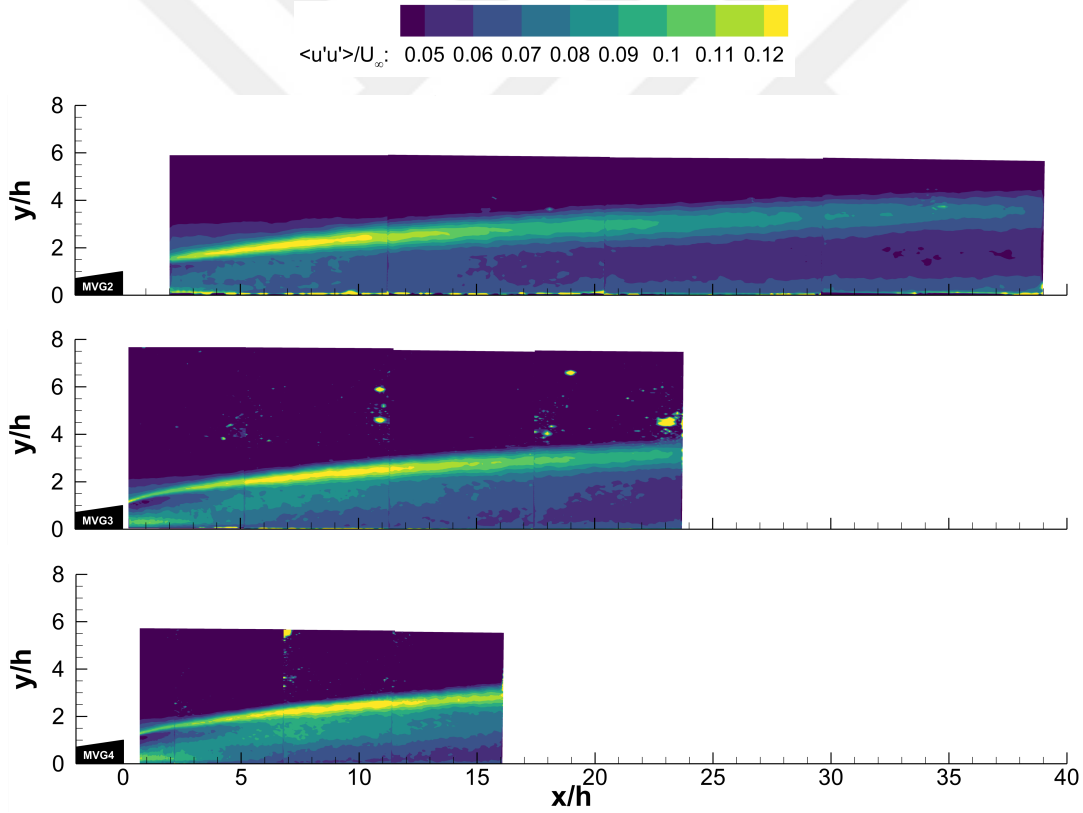

Figure 3.10 Contours of normalized streamwise velocity fluctuations.

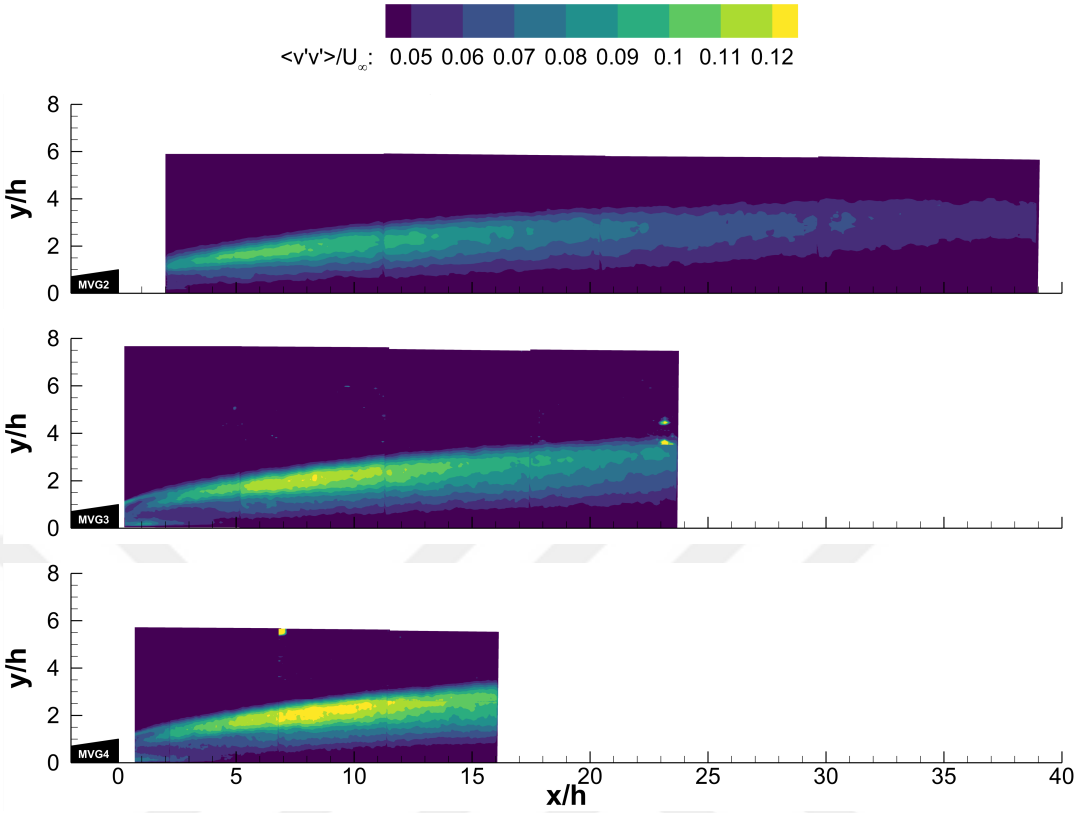

Figure 3.11 Contours of normalized wall-normal velocity fluctuations.

The extracted profiles of the velocity fluctuations comparing MVG2, MVG3, and MVG4 at x/h=5, 10, and 15 are given in Figure 3.12 and Figure 3.13 to illustrate the height effect on the velocity fluctuations. As is the case for streamwise and wall-normal velocities, the effect of the MVG height is more pronounced for the wall-normal component of the velocity fluctuations, as the streamwise velocity fluctuations tend to equalize for all the MVGs further downstream. The contours of normalized velocity fluctuations, especially for the streamwise component (Figure 3.10), show a concentration of slightly higher values near the wall, up to around three device heights, indicating the formation of the secondary vortices due to the shear between the primary vortices and the wall. To display the secondary vortices in a more quantified fashion, profiles of velocity fluctuations are extracted at x/h=2 and given in Figure 3.14. The profiles show the rapid decay of the secondary vortices as the peaks seen at x/h=2 are flattened at x/h=5 (Figure 3.12 and Figure 3.13). The streamwise evolutions of streamwise and wall-normal velocity fluctuations are given in Figure 3.15 and Figure 3.16. The profiles indicate the lift-off of the MVG wake.

The trends for the streamwise and wall-normal velocity fluctuations are quite similar as they flatten further downstream. The concentration of the peaks on the upper part of the wake, indicating the shear layer, is seen in both streamwise and wall-normal velocity fluctuations. Moreover, the increase seen in the fluctuations, i.e., the peaks, is explained by Herges [65] as a consequence of the presence of the streamwise vortex pair. However, the increased fluctuations seen at the shear layer where the vigorous motion of the Kelvin-Helmholtz (K-H) instability is dominant indicates the presence of the K-H instability, which is already shown by Sun [77] in supersonic flow regimes. The following section investigates the possible presence of K-H instability in subsonic flow regimes.

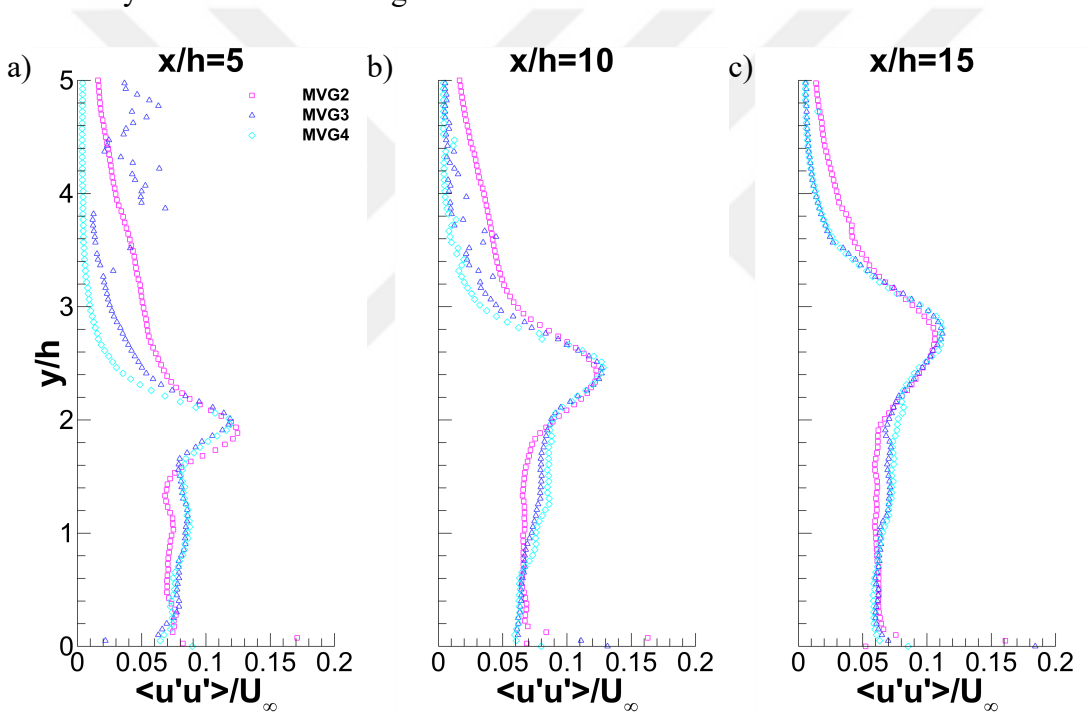

Figure 3.12 Profiles of normalized streamwise velocity fluctuations at different downstream positions. a) x/h=5, b) x/h=10, c) x/h=15.

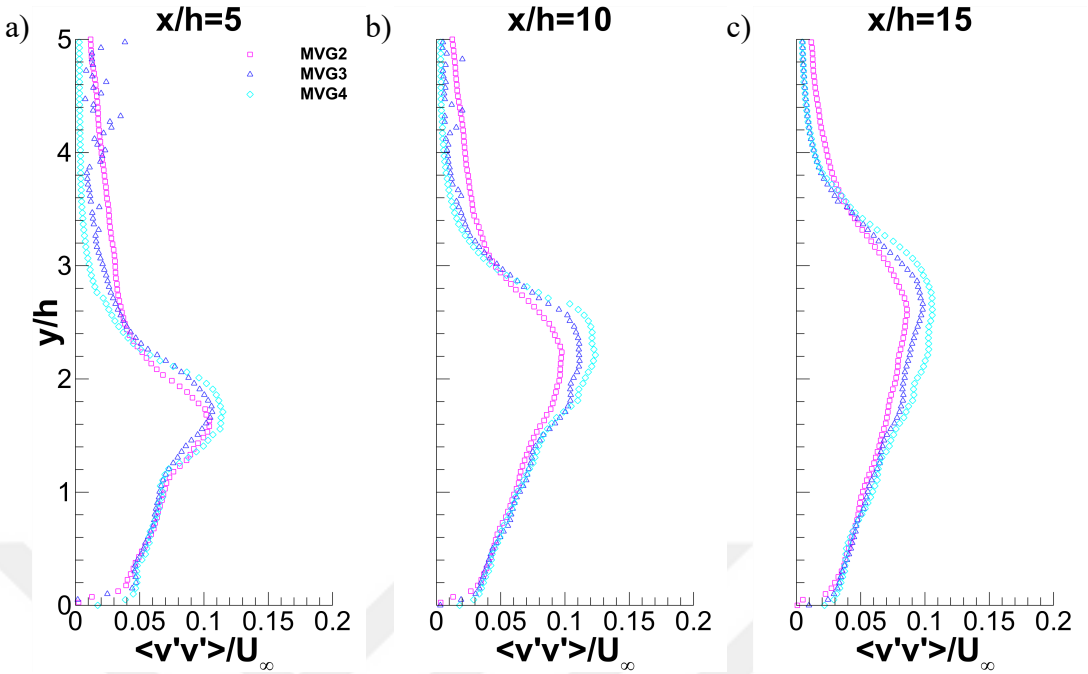

Figure 3.13 Profiles of normalized wall-normal velocity fluctuations at different downstream positions. a) x/h=5, b) x/h=10, c) x/h=15.

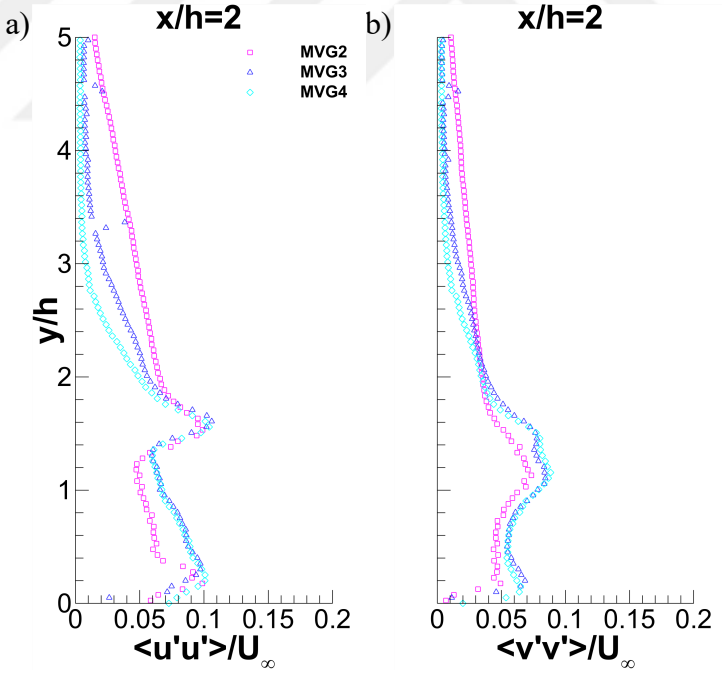

Figure 3.14 Profiles of normalized velocity fluctuations at different at x/h=2. a) streamwise component, b) wall-normal component.

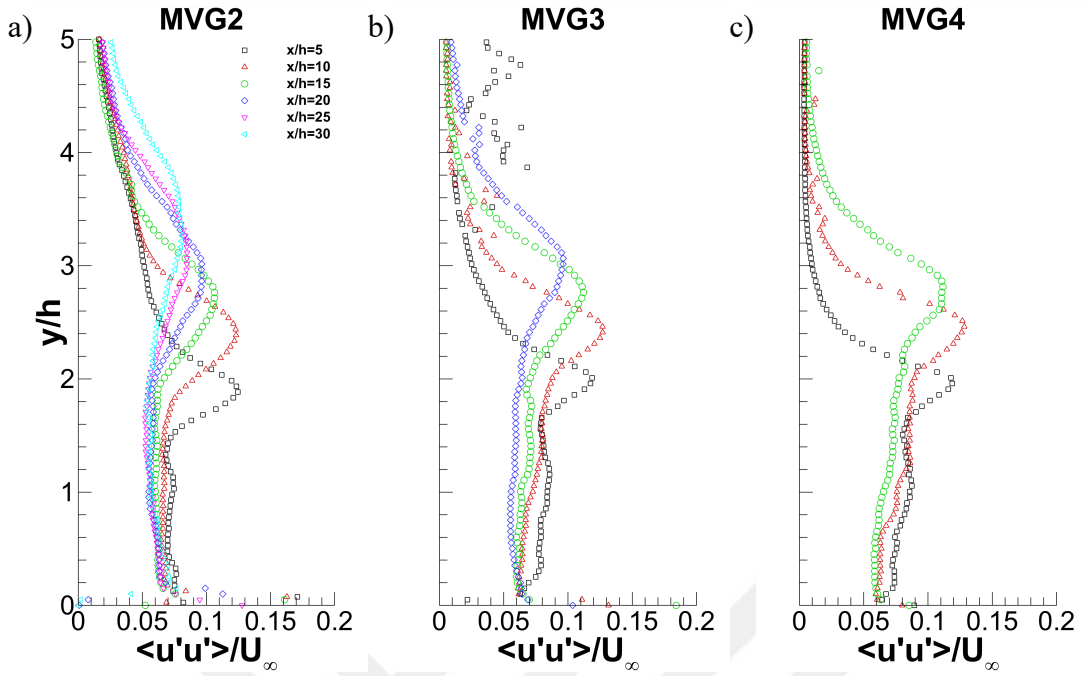

Figure 3.15 Streamwise evolution of normalized streamwise velocity fluctuations. a) MVG2, b) MVG3, c) MVG4.

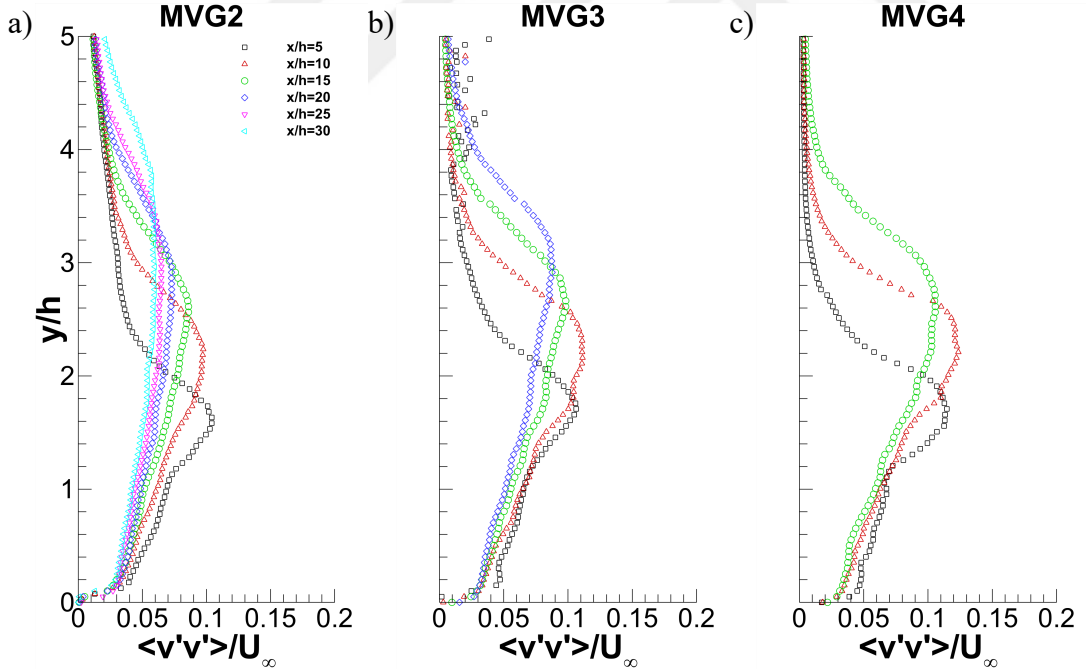

Figure 3.16 Streamwise evolution of normalized wall-normal velocity fluctuations. a) MVG2, b) MVG3, c) MVG4.

3.3.2 Reynolds Shear Stress

The shear layers generated by the MVG wakes are evident from the normalized Reynolds shear stress contours (Figure 3.17). The large-scale turbulent structures generated by the MVGs are seen clearly from the high magnitude of the Reynolds shear stress values. The concentration of negative peaks in the top part of the shear layer shows the shearing effect of the MVG wake, whereas the positive peaks show the upwash motion of the wake, indicating the high mixing activity in the wall-normal direction [65, 77]. The shear layer continues to be observed further downstream; however, it starts to weaken for MVG2 after approximately 14 device heights. This is especially valid for the positive peaks of the Reynolds shear stress, indicating the streamwise position at which the mixing activity diminishes.

In contrast to MVG2, the extent and the strength of the shear layer are more significant with increasing device height for both positive and negative peaks of the Reynolds shear stress. In order to quantify the above discussion, the MVGs are compared by extracting profiles at various x/h locations in terms of Reynolds shear stress in Figure 3.18. As expected, the two peaks, one negative and one positive, seen in the contours are also seen in the profiles, with the values tending to zero as they approach the freestream. Similar to the distributions of vorticity and velocity fluctuations, distributions for MVG3 and MVG4 resulted in comparable values, with MVG4 showing slightly higher lift-off as the peaks of Reynolds shear stress are located in higher y/h positions. In comparison, the profiles for MVG2 indicate more flattened distributions, especially at further downstream stations. Figure 3.19 shows the streamwise evolution of Reynolds shear stress distributions for each MVG. The lift-off of the wake is clearly observed from the profiles for both positive and negative peaks. The profiles get flattened as the wake progresses downstream. As mentioned for the contours seen in Figure 3.17, the positive peaks flatten well before their negative counterparts, indicating the diminishing mixing effect.

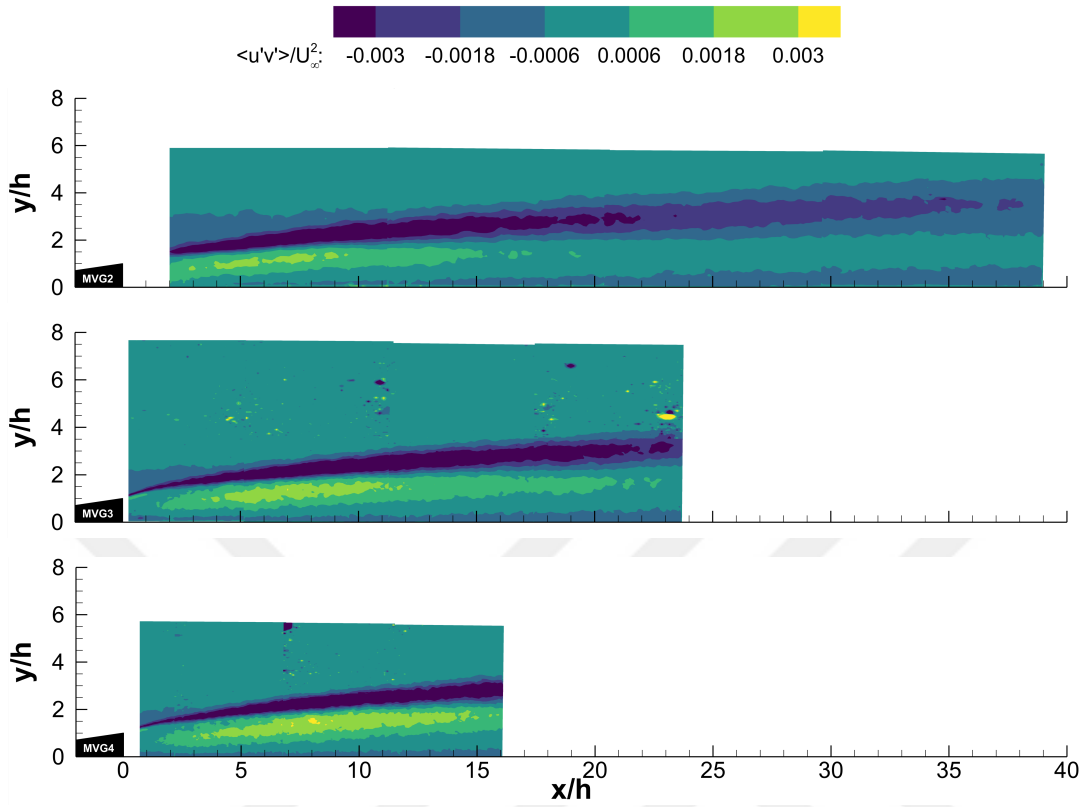

Figure 3.17 Contours of normalized Reynolds shear stress.

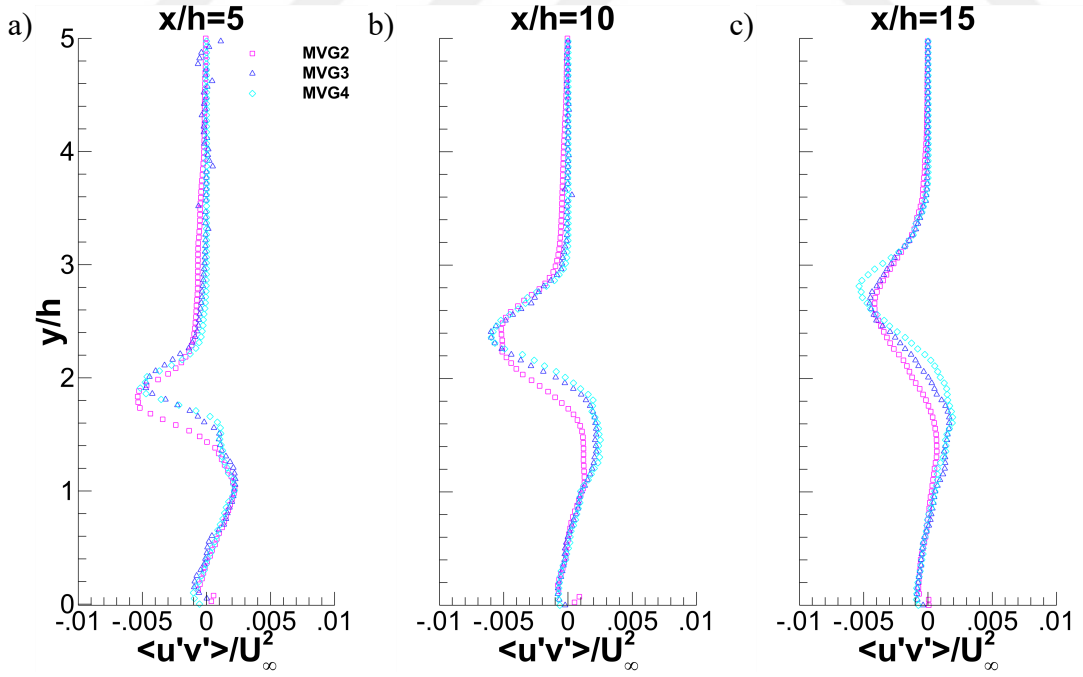

Figure 3.18 Profiles of normalized Reynolds shear stress at different downstream positions. a) x/h=5, b) x/h=10, c) x/h=15.

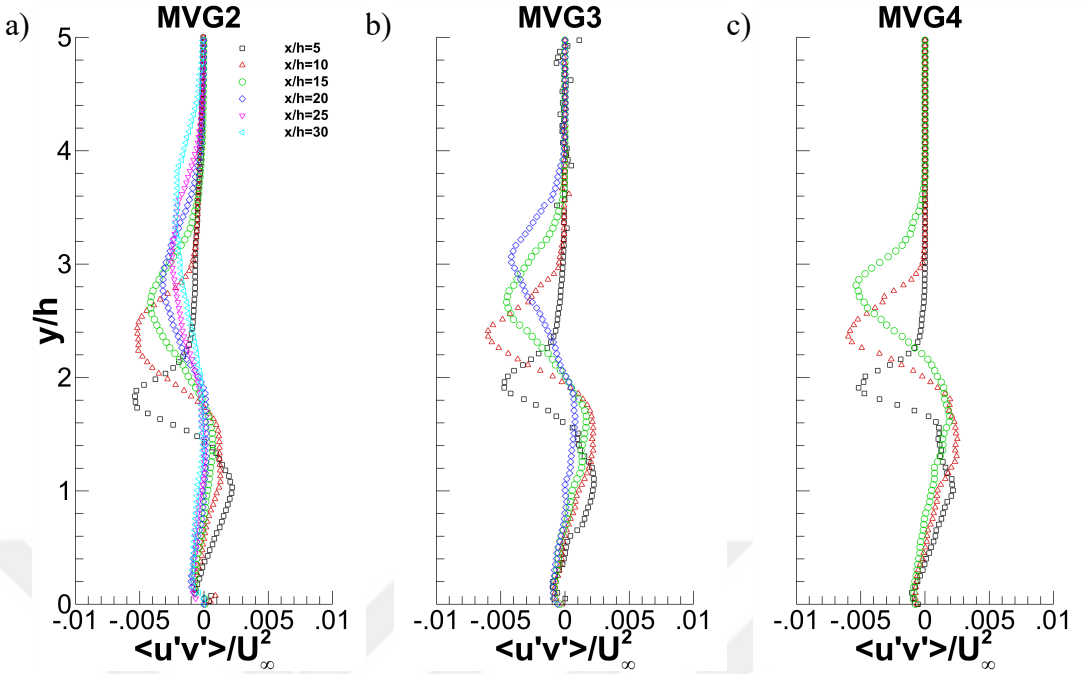

Figure 3.19 Streamwise evolution of normalized Reynolds shear stress. a) MVG2, b) MVG3, c) MVG4.

3.4 Proper Orthogonal Decomposition

Proper Orthogonal Decomposition (POD) is a mathematical tool used to decompose the flow structure into a finite set of spatial modes based on the kinetic energy content. The POD method was first suggested by Lumley [79] to prove the existence of well-organized energetic structures by removing the external effect of the incoming flow and filtering the instabilities that most probably influence the initial development of turbulence. Sirovich [80] later established the Snapshot Proper Orthogonal Decomposition (SPOD) method, which is more appropriate for datasets with high spatial density but low temporal frequency.

3.4.1 Mathematical Background of POD

POD, or SPOD, is a statistical tool used to break the space-time flow fields into discrete spatial modes and temporal coefficients based on their kinetic energy contents by computing the major eigenvalues and eigenvectors of a matrix composed of the snapshots of the flow using the method given by the equations below.

The fluctuating velocity is given by the equation below,

$$u'(x,t) = U(x,t) - \overline{U}(x,t) \qquad [3.1]$$

where, U(x,t) is the instanteous velocity snapshots and $\overline{U}$(x,t) is the mean velocity, and x and t refer to spatial coordinates. The instantaneous vector field is then decomposed into a series of deterministic spatial functions, as shown by the equation below.

$$u'(x,t) = \sum_{n=1}^{N} a_n(t)\, \phi^{(n)}(x) \qquad [3.2]$$

Where $a_n(t)$ is the time-dependent POD coefficient for the mode n, $\phi^{(n)}(x)$ is the spatial POD mode for the mode n, and N is the number of snapshots. The changing velocity instantaneously measured over M spatial positions and N times is organized into the matrix below.

$$\widehat{U} = \frac{1}{N}\begin{bmatrix} u_1'^1 u_1'^2 & \cdots & u_1'^N \\ \vdots & \ddots & \vdots \\ u_M'^1 u_M'^2 & \cdots & u_M'^N \end{bmatrix} \quad [3.3]$$

The auto-covariance matrix (C) is defined as,

$$C = \widehat{U}^T \widehat{U} \quad [3.4]$$

The above steps introduce this problem as an eigenvalue problem, demonstrated as follows, where A_n is the eigenvector, which corresponds to the eigenvalue λ_n.

$$CA_n = A_n \lambda_n \quad [3.5]$$

The eigenvalues of all N modes are ordered with respect to their magnitude as follows, where λ_n is set to zero during the analysis.

$$\lambda_1 > \lambda_2 > \lambda_3 > \cdots > \lambda_n \quad [3.6]$$

The resulting normalized POD modes that are produced from the solutions to the eigenvalue problems can be written as,

$$\phi^{(n)} = \frac{\widehat{U} A_n}{\left\| \widehat{U} A_n \right\|} \quad [3.7]$$

where ||…|| denotes the L_2-norm. It's worth noting that the eigenfunctions found here are orthogonal in time rather than space. After concatenating the POD modes to form, $\Psi=[\phi^{(1)},\phi^{(2)}\ldots\phi^{(n)}]$, the POD coefficients can then be found as follows:

$$a_n = \Psi^{-1} u_n' \quad [3.8]$$

3.4.2 Flow Structures of MVG Wake

The concentration of higher peaks on the upper part of the wake seen in both streamwise and wall-normal velocity fluctuations in the velocity fluctuations plots (Figure 3.10 and Figure 3.11) is explained by only the presence of the streamwise vortices by Herges *et al.* [65]. However, Li and Liu [73] discovered a new mechanism of SBLI control by the vortex pair generated by the MVGs, which is highly associated with a train of vortex rings, which was discussed as the most dominant mechanism of control of SBLI. Later, Sun [71] illustrated the conceptual organization in the wake of a ramp-type MVG (Figure 1.12). It was revealed that the primary mechanism resulting in the ring-type vortex generation in the MVG wake is the K-H instability first by Li and Liu [73] and then by Sun [71] and Giepman [74] starting from approximately four device heights downstream and up to 32 device heights downstream the MVGs. The vortex ring formation is found to be starting at 18 device heights downstream of the MVG in Sun's study [71]. Moreover, it was proven that this type of vortex can endure the shockwave with no evidence of breakdown [81]. In the search for the K-H instability, the POD technique is used in several studies to investigate the MVG wake. In two separate studies, Dong *et al.* [82, 83] used SPOD to investigate an MVG wake at M=2.5 and Re_{θ}=5760 for a Large Eddy Simulation case. On the first one [82], they concluded that the 1st mode, which carried the characteristics of the streamwise vortices, had the highest energy contribution. The characteristics of the streamwise vortices were also observed in the 2nd and 3rd modes. The fluctuation motion induced by the K-H instability started from the 4th and 5th modes. In their second study [83], they studied the physical mechanism of each POD mode using the Liutex core line identification introduced by Wang *et al.* [84]. In their results, they have identified two pairs of counter-rotating vortices, fluctuated roll-up motion of the streamwise vortex with large-scale structures, and K-H instability, which they have named the most significant unsteady feature of the MVG wake. Charkrit and Liu [85] applied SPOD to a Direct Numerical Simulation (DNS) dataset of an MVG wake to analyze the K-H instability in the hairpin ring

areas of the flow transition in order to gain insight into the ring-type vortex formation. It was stated that the 1st mode showed the characteristics of the streamwise vortex pair while the other modes showed the fluctuating motions induced by the K-H instability. They have concluded that the arc-shape vortex is not deformed into a hairpin vortex by itself but is formed by the K-H instability during the formation of the arc-shaped vortex and hairpin vortex during the boundary layer flow transition. Moreover, they have also studied the K-H instability using a 2-dimensional numerical simulation for an inviscid flow (Figure 3.20). The shear layer generated is seen in Figure 3.20 a and b, which then takes the form of a ring-like vortex resulting from the induced transfer of the motion of shear to rotation by the K-H instability (Figure 3.20 c and d). In Figure 3.20 e to h, it was seen that the two rotations become one with a still distinct pair of cores. The authors stated that the vortex pairing seen here is a distinguished indication of K-H instability.

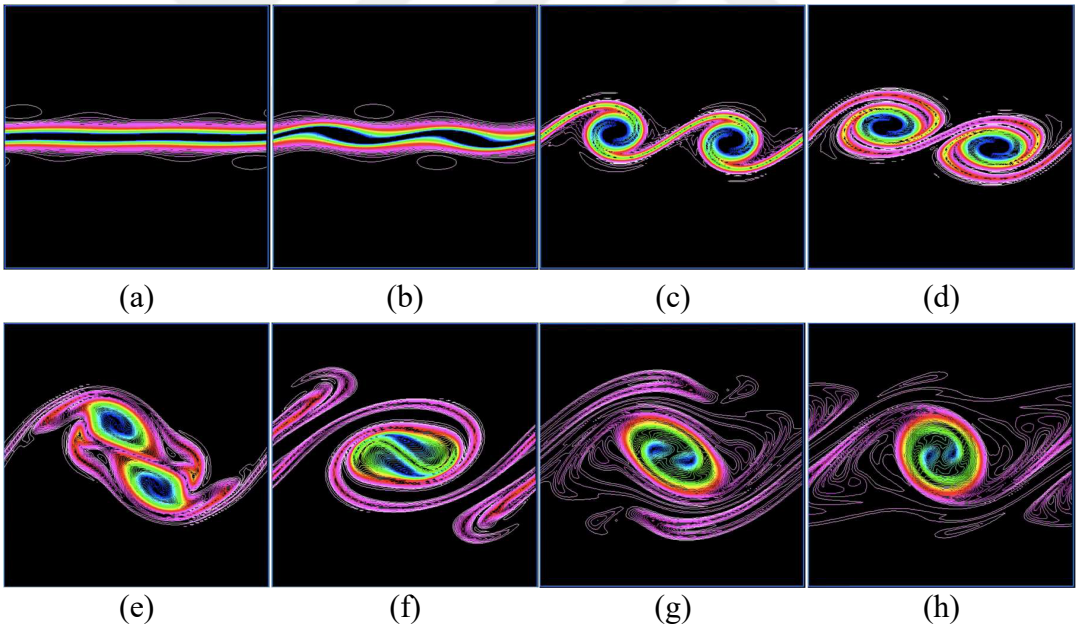

Figure 3.20 2-Dimensitonal Numerical simulation on K-H instability [85].

3.4.3 POD Analysis of Ramp-Type MVG Wake

The SPOD analyses are done for MVG2 and MVG3 only since the measurement field of view for MVG4 does not cover enough wall-normal distance to illustrate meaningful results for the analysis. The POD analyses are performed for Window 2 (Figure 2.8), corresponding to a range of approximately x/h=12 to 20 and y/h=0 to 5 for MVG2. The analyses are done for MVG3 for Window 3 (Figure 2.8), corresponding to a range of approximately x/h=12 to 17.5 and y/h=0 to 3.75.

Figure 3.21 illustrates the first ten modes for MVG2, which clearly shows the development of the K-H instability in the MVG wake. The first mode clearly shows the interface between the two zones of fluid caused by the shear layer in the wake, which is an essential phenomenon for the K-H instability to form. The 2^{nd}, 3^{rd}, and 4^{th} modes show the formation of vortex pairs. It should be noted that the pairs are not that distinctive in the 4^{th} mode compared to the 2^{nd} and 3^{rd} modes. The vortex pairing is due to the shear being transferred to rotational vorticity with the action of the K-H instability. Starting from the 5^{th} mode and clearly seen in the 7^{th} mode, the paired vortices seem to merge as the vortical features show an encircling behavior. The 9^{th} and 10^{th} modes illustrate that the vortices are merged with a distinctive pair of cores. The first ten modes for MVG3 are given in Figure 3.22, which shows similar modes when compared to the modes of MVG2. The modes for both MVGs show similar behavior to Chakrit and Liu [85] (Figure 3.20), proving that the K-H instability is present in the wake of a ramp-type MVG in subsonic flow regimes.

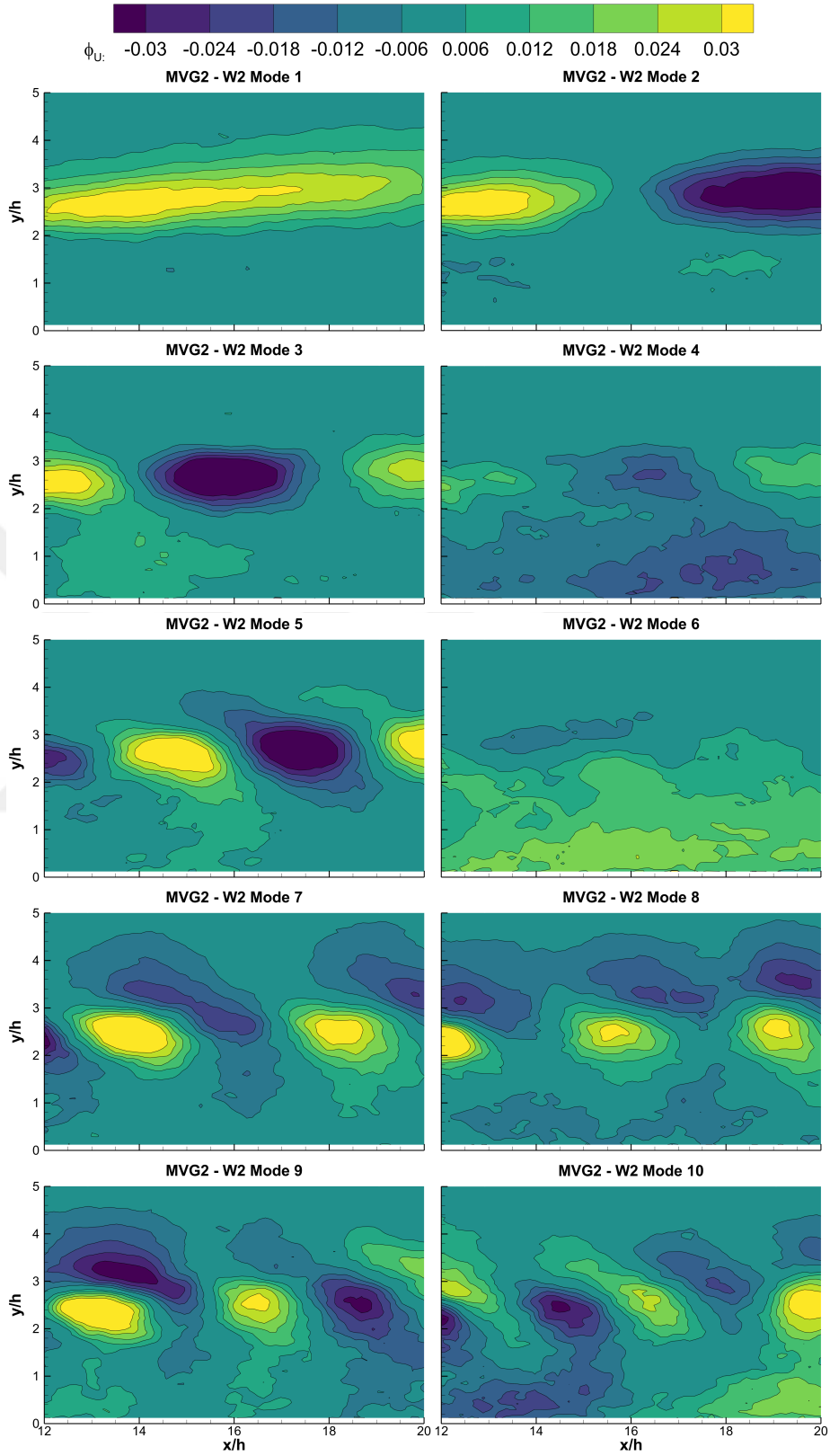

Figure 3.21 Streamwise POD components (ϕ_U) of the first ten modes for MVG2.

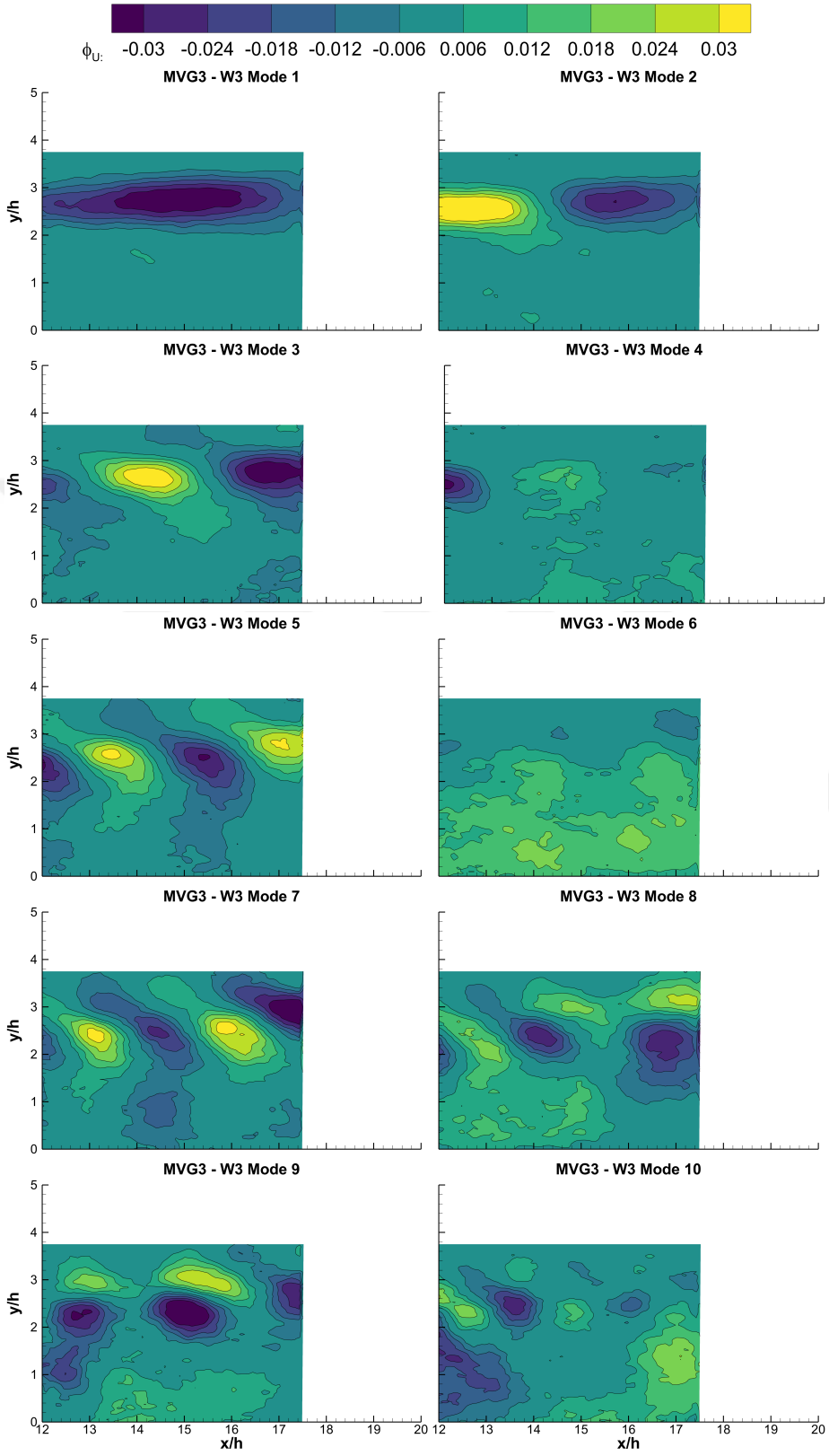

Figure 3.22 Streamwise POD components (ϕ_U) of the first ten modes for MVG3.

The energy level comparison of the TKE percentages associated with the first 100 modes based on the streamwise velocity component (U) is given in Figure 3.23 for MVG2 and MVG3. The 1st mode is the most dominant mode for both MVGs. The contribution of the 1st mode to the total TKE is higher in MVG2 than that of MVG3. In contrast, the contributions of the modes up to the 10th mode for MVG3 are either at the same level or higher than MVG2, indicating that MVG3 generates a more vigorous K-H instability compared to MVG2 which leads to the generation of a vortex pair that with a higher strength again compared to those generated by MVG2.

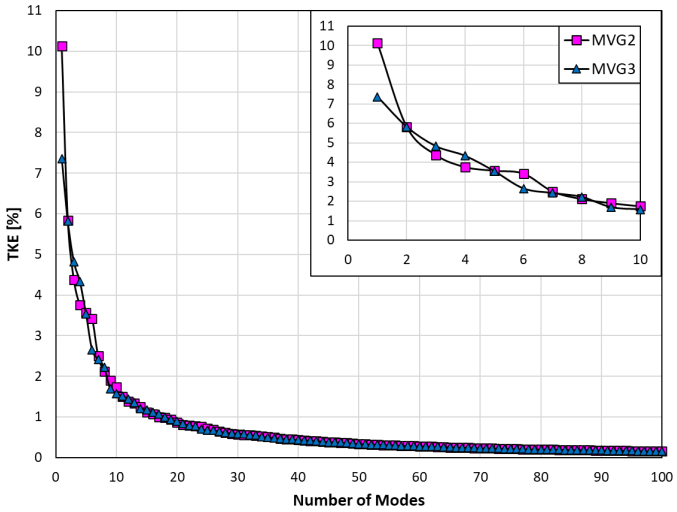

Figure 3.23 Comparison of percentage of TKE associated with the first 100 modes based on the streamwise velocity component (U) for MVG2 and MVG3.

The fact that the K-H instability and the resulting K-H vortices are present in the wake of MVGs at subsonic flow regimes shows that the wake, i.e., the streamwise vortex pair, might be undulating with the effect of K-H vortices. To illustrate this, Figure 3.24 shows the contours of the out-of-plane vorticity component on an instantaneous snapshot for MVG2. To show the K-H vortices and match their swirling effect to the approximate vortex centers, a vector distribution is superposed on the contours with a convective velocity of $0.85U_\infty$, using the same method given in [77]. After finding the approximate center of the K-H vortices, the vectors represented in a convective frame of reference are then shown with the streamwise velocity contours (Figure 3.25). The effects of the K-H vortices in the streamwise velocity distribution are clearly seen as the shear layer shows a wavy form, which

can be recognized as the effect of the K-H instability. Moreover, the streamwise velocity distribution and the vectors showed locally accelerated fluid above the vortices and locally decelerated fluid below the vortices, with the vortices swirling in the clockwise direction, showing the expected roll-up motion which is the precursor of the vortex ring formation shown in the conceptual model of the ramp-type MVG wake given in Figure 1.12.

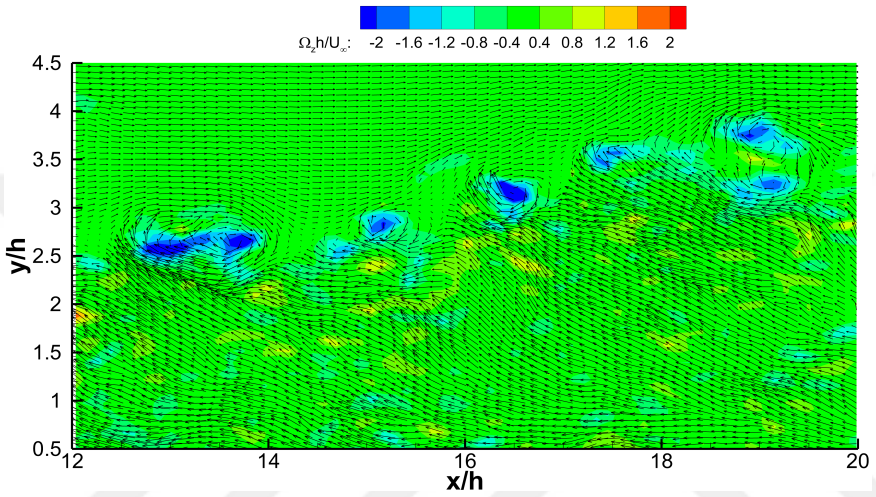

Figure 3.24 Contours of the out-of-plane vorticity component with the velocity vectors represented in the convective reference frame of $0.85U_\infty$.

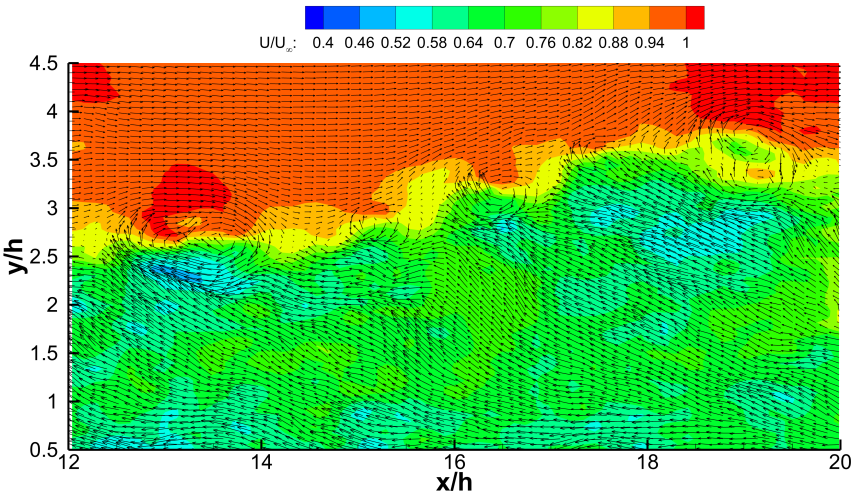

Figure 3.25 Contours of the streamwise velocity component with the velocity vectors represented in the convective reference frame of $0.85U_\infty$.

CHAPTER 4

NUMERICAL STUDY

This section presents the numerical setup and the results of the numerical study for the MVGs. The aim of the numerical study is twofold: to extend the study to include more MVGs and to investigate the three-dimensional characteristics of the ramp-type MVG wake, which is impossible with 2D2C PIV data. First, the numerical case setup is described in terms of the MVG models, grid generation, and numerical methods. Then, the numerical results are presented and compared with the experimental results in terms of streamwise and wall-normal velocity components and out-of-plane vorticity for the symmetry plane. This chapter focuses on the validation of the numerical study and the effect of increasing device height as it is made possible by the addition of MVG5 and MVG6.

4.1 Numerical Case Setup

4.1.1 Computational Analysis

The steady-state simulations are run through ANSYS Fluent software. Reynolds-Averaged Navier-Stokes (RANS) equations are solved with the k-ω SST turbulence model, which can effectively predict the flow development in the near-wall regions, as proposed by Menter [86, 87]. The second-order upwind discretization scheme is used for momentum and turbulence equations, and the COUPLED algorithm is employed, which solves the pressure-based continuity and momentum equations together. The turbulence model, namely the k-ω SST model, was chosen after a comparative study employing MVG2, which was selected as the current study's benchmark case as it allows to reduce the computational time and CPU cost with its smaller size.

The inlet and the outlet are defined as velocity inlet and pressure outlet, respectively. The wall surfaces of the domain and MVG are defined as walls with the no-slip condition. In addition, due to the axisymmetric geometry of the flow domain, a symmetry plane is defined that passes along the centerline of the MVG to reduce the computational time and cost. The inlet velocity is adjusted such that the velocity just upstream of the MVG is 10.1 m/s for every case, and the $TI_{ambient}$ value is selected as 0.35%, consistent with the flow parameters of the experiments. All simulations are run for 1500 iterations to reach scaled residuals below 10^{-7}, which is determined as a convergence criterion. MVGs used for the numerical study have the same design as their experimental counterparts (Figure 2.6), and there were no modifications to the shape or design of the original geometries or the edges of the MVGs. As mentioned above, MVG2 was chosen as the benchmark for grid convergence and validation studies. Furthermore, after validation of the numerical case employing MVG2, the experimental results for MVG3 and MVG4 were also compared with the numerical simulation results. In order to extend the study, two more MVGs having larger heights (i.e., larger h/δ ratios) were also employed in the numerical study, namely MVG5 and MVG6. The dimensions and their corresponding h/δ ratios for all the MVGs used in the numerical study are given in Table 4.1.

Table 4.1 MVG dimensions and their corresponding h/δ ratios used for the numerical study.

MVG	**h**	**w**	**c**	**α**	**h/δ**
Design	-	6.1h	6.9h	24°	-
MVG2	20 mm	122 mm	138 mm	24°	0.18
MVG3	30 mm	183 mm	207 mm	24°	0.27
MVG4	40 mm	244 mm	276 mm	24°	0.36
MVG5	50 mm	305 mm	345 mm	24°	0.45
MVG6	60 mm	366 mm	414 mm	24°	0.54

4.1.2 Domain and Mesh Generation

Pointwise software is employed to generate a fully structural multi-block flow domain. Y-type block topology is employed on MVGs to obtain high-quality mesh without changing the original geometries, including the edges of the MVGs (Figure 4.1). The size of the flow domain is 6.5 x 1 x 0.5 m^3 (Figure 4.2). MVGs are placed at the origin of the coordinate system, with the distances from the inlet, side walls, and the top wall being identical to those of the wind tunnel experiments, while the downstream distances are kept longer. The initial height of the cells adjacent to the walls and MVGs are set to obtain y^+=1 to ensure that the near-wall meshes are in a log-law layer. In the vicinity of the MVGs, locally denser grids are generated to resolve turbulent flow features. Smooth transition between the blocks of meshes both upstream and downstream of the MVGs is provided by implementing a constant growth rate.

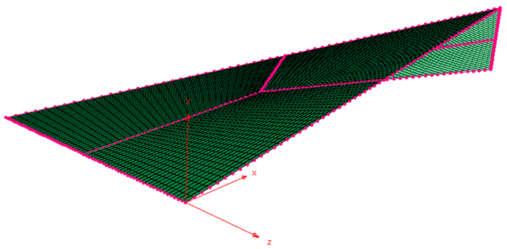

Figure 4.1 Y-type block topology seen on an MVG (half model).

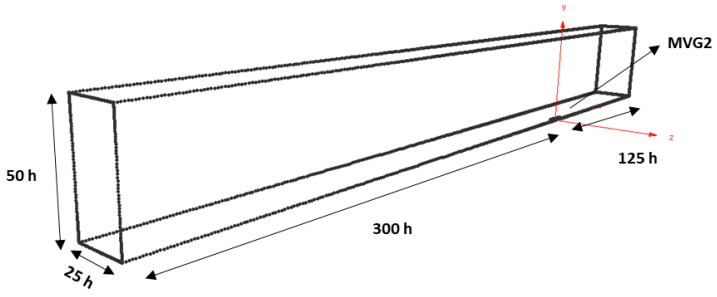

Figure 4.2 Numerical domain. Non-dimensional dimensions are given with regards to MVG2.

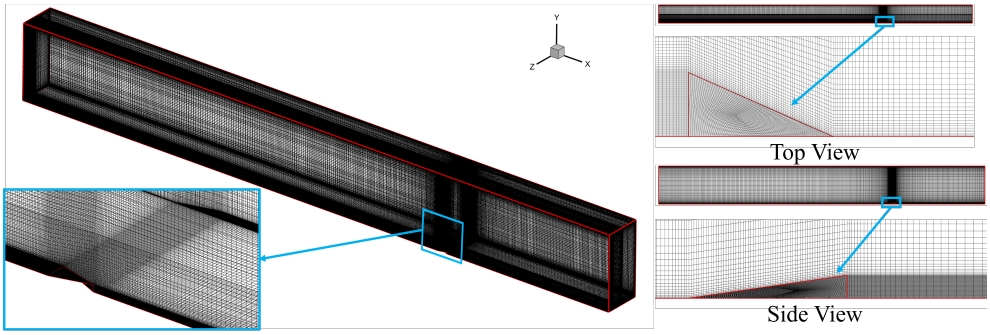

Figure 4.3 Grid with top and symmetry plane views, showing the locally denser regions in the vicinity of the MVG.

4.1.3 Grid Convergence Study and Validation

A grid convergence study is performed with the benchmark case (MVG2) to obtain the optimum mesh sizing and total number. Grid generation for the MVG cases is based on this study, and the number of mesh cells is extrapolated for the other cases with larger MVG dimensions. Table 4.2 shows the mesh cell numbers on the benchmark case and the total number of mesh cells in the numerical domain of test cases that are employed in the grid convergence study. All simulations are conducted under the same boundary layer inflow conditions, simulating the wind tunnel experiments. It is worth noting that the first cell heights adjacent to the MVG2 and other wall boundaries are kept constant for all cases to achieve $y^+=1$.

Table 4.2 Mesh cell numbers on MVG2 and the total number of mesh cells in the numerical domain for the grid convergence study.

Mesh No	Number of Cells on the MVG	Total Number of Cells
1	1,936	3,975,958
2	4,422	6,021,485
3	7,744	9,101,425
4	3,456	4,461,756

Simulation results are compared with the experimental data in terms of normalized streamwise velocity profiles in Figure 4.4 and wall-normal velocity profiles at various downstream positions for the benchmark case (MVG2) in Figure 4.5.

Although there are discrepancies in the near wake region, for example, at x/h=5, both velocity profiles of Mesh 2 and Mesh 3 are obtained in good agreement with the experimental data and very similar to each other at each downstream position. In order to illustrate the converging behavior of the grid, a grid is generated, which is in between Mesh 1 and Mesh 2 in terms of the number of cells (Table 4.2). The approximate discrepancies in terms of maximum velocity deficit, maximum wall-normal velocity, and their positions between the numerical and experimental results for MVG2 are given in Table 4.3 up to x/h=20.

Table 4.3 Approximate discrepancies in terms of maximum velocity deficit, maximum wall-normal velocity, and their positions between the numerical simulations and experimental results for MVG2 at x/h=5, 10, 15, and 20.

Position	Parameter	Mesh 1	Mesh 2	Mesh 3	Mesh 4
x/h=5	U_{min}	-9%	-4%	-3%	-5%
	$(y/h)_{Umin}$	-20%	3%	3%	2%
	V_{max}	-26%	15%	14%	11%
	$(y/h)_{Vmax}$	-20%	1%	1%	2%
x/h=10	U_{min}	-7%	-4%	-4%	-5%
	$(y/h)_{Umin}$	-30%	1%	1%	1%
	V_{max}	-41%	15%	14%	10.5%
	$(y/h)_{Vmax}$	-45%	1%	1%	4%
x/h=15	U_{min}	-8%	-4%	-4%	-5%
	$(y/h)_{Umin}$	-30%	1%	1%	1%
	V_{max}	-40%	13%	12%	10%
	$(y/h)_{Vmax}$	-37%	2%	2%	2.5%
x/h=20	U_{min}	-7%	-3%	-3%	-4%
	$(y/h)_{Umin}$	-30%	1%	1%	1%
	V_{max}	-39%	15%	17%	11%
	$(y/h)_{Vmax}$	-36%	1%	1%	2%

Mesh 2 achieves a good agreement for the normalized streamwise velocity profiles (Figure 4.4) for MVG2 in general. Regarding the velocity values, the numerical simulations seem to be underpredicting in the region where y/h is less than 1. A better agreement was achieved regarding the position of the maximum velocity deficit (i.e., the minimum streamwise velocity value). In order to quantify the agreement between the results of the numerical simulations and experiments, the value and the position of the maximum velocity deficit can be used. For example, all the cases underpredicted the maximum velocity deficit by approximately 5%. However, the

cases differ regarding the position of the maximum velocity deficit, with Mesh 1 underpredicting it by approximately 40%, whereas the Mesh 2 and Mesh 3 results are virtually the same as the experimental results.

Normalized wall-normal velocity profiles are given in Figure 4.5 for MVG2. With Mesh 1, both the value and position of the maximum wall-normal velocity are underpredicted by 35% and 42%, respectively. With Mesh 2 and Mesh 3, which are nearly identical, the values of maximum wall-normal velocity are overpredicted by approximately 15% at x/h=5, whereas their positions are predicted with a near-perfect match for all the streamwise stations. At further streamwise stations, the discrepancy in the values of the maximum upwash velocity decreases dramatically. Another grid is generated later on to illustrate the converging behavior of the grid, namely Mesh 4. As can be seen from Figure 4.4, even though the profiles for Mesh 4 are between the profiles for Mesh 1 and Mesh 2, Mesh 4 shows similar discrepancies regarding the streamwise velocity component. However, the convergence behavior is seen more clearly in terms of the wall-normal velocity component (Figure 4.5).

Although the agreement for the wall-normal velocity component between the profiles extracted from the results of the numerical simulations and experiments is worse than that for the streamwise velocity component, a sufficient agreement between the two is achieved considering the capabilities of RANS simulations. To summarize, a satisfactory agreement between the numerical simulation and experimental results regarding the velocity profiles could not be reached with Mesh 1. In contrast, Mesh 2 and Mesh 3 yield satisfactory results for both velocity components. However, as mentioned before, due to Mesh 3's higher cell numbers, Mesh 2 is selected for further numerical simulations.

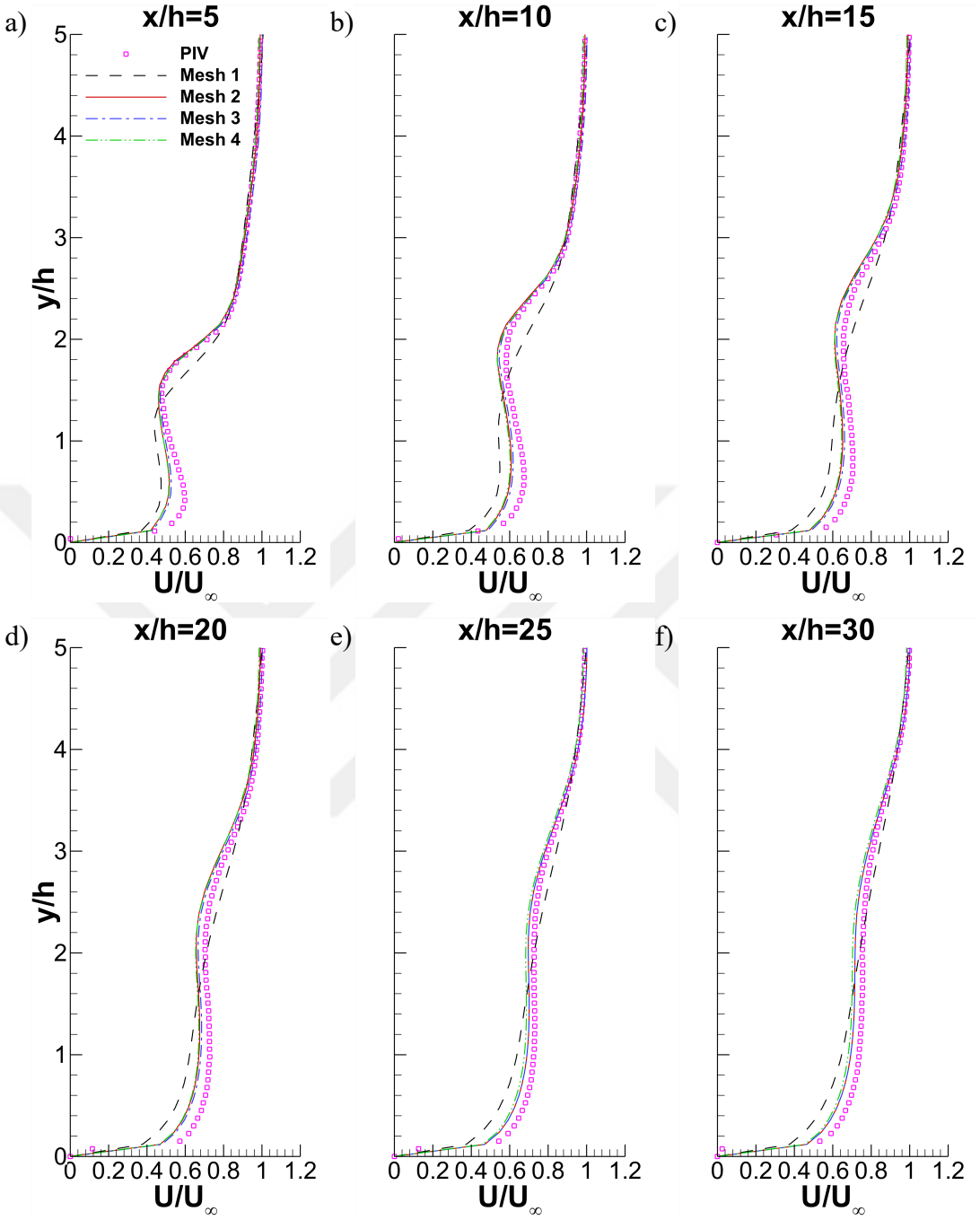

Figure 4.4 Comparison of the grid convergence cases and validation of the simulation results in terms of streamwise velocity for the benchmark case (MVG2) at a)x/h=5, b) x/h=10, c) x/h=15, d) x/h=20, e) x/h=25, f) x/h=30.

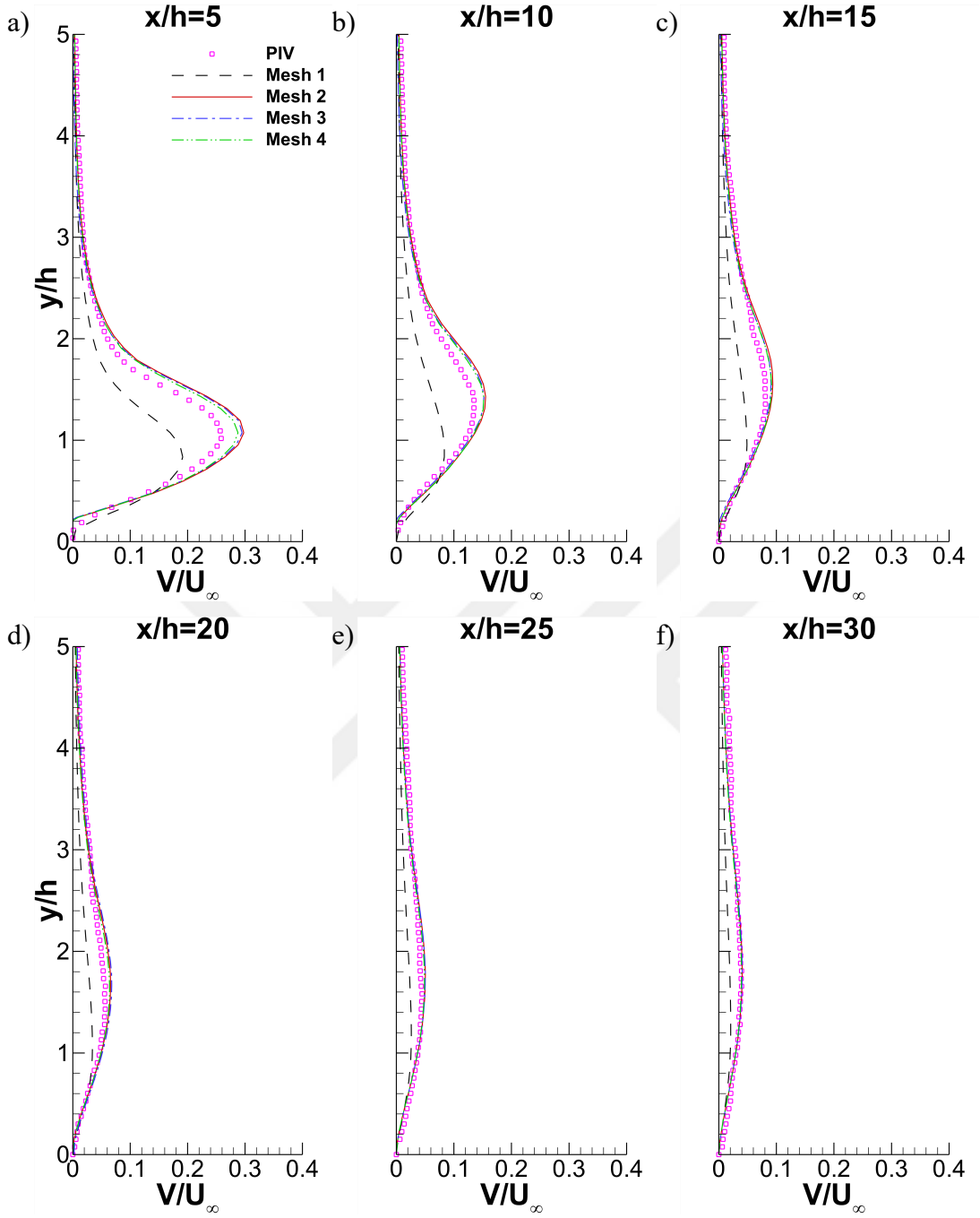

Figure 4.5 Comparison of the grid convergence cases and validation of the simulation results in terms of wall-normal velocity for the benchmark case (MVG2) at a)x/h=5, b) x/h=10, c) x/h=15, d) x/h=20, e) x/h=25, f) x/h=30.

4.1.4 Validation of MVG3 and MVG4 Simulations

As a part of the grid convergence study, the numerical simulation results for MVG2 are validated in terms of the streamwise and wall-normal velocity components. After the validation of the numerical simulation results for MVG2, the numerical case using the best mesh in terms of accuracy and CPU time, namely Mesh 2, was extrapolated for MVG3 and MVG4, resulting in a total number of cells of 8.2M and 10.2M, respectively. The results are validated up to x/h=20 for MVG3 and up to x/h=15 for MVG4, as the measurement fields of view for the 2D2C PIV experiments are limited (Figure 2.8). In this section, the validation regarding the results of the out-of-plane vorticity component (Ω_z) is also included for the MVGs.

The normalized streamwise velocity component comparisons for MVG3 and MVG4 are given in Figure 4.6. As it is with the MVG2 case, the results show a good comparison. However, approximately the same discrepancies seen for the MVG2 case are present as the streamwise velocity profiles are underpredicted, especially below y/h=1, and the maximum velocity deficit values are slightly underpredicted. For example, for MVG3 and MVG4 at x/h=5, the maximum velocity deficit is underpredicted by approximately 5%. The positions of the maximum velocity deficit for both MVGs are virtually the same for the numerical simulation and experimental results.

The normalized wall-normal velocity component for MVG3 and MVG4 is compared in Figure 4.7. Again, similar to the MVG2 case, the value of the maximum upwash velocity is overpredicted; however, with increasing device height, the disparities between the numerical simulations and the experimental results seem to decrease regarding the maximum upwash velocity, as the overprediction for MVG3 and MVG4 are approximately 9% and 7% at x/h=5, respectively. Regarding the positions of the maximum upwash velocity, virtually the same results are observed for the numerical simulations and experimental measurements, similar to the MVG2 case.

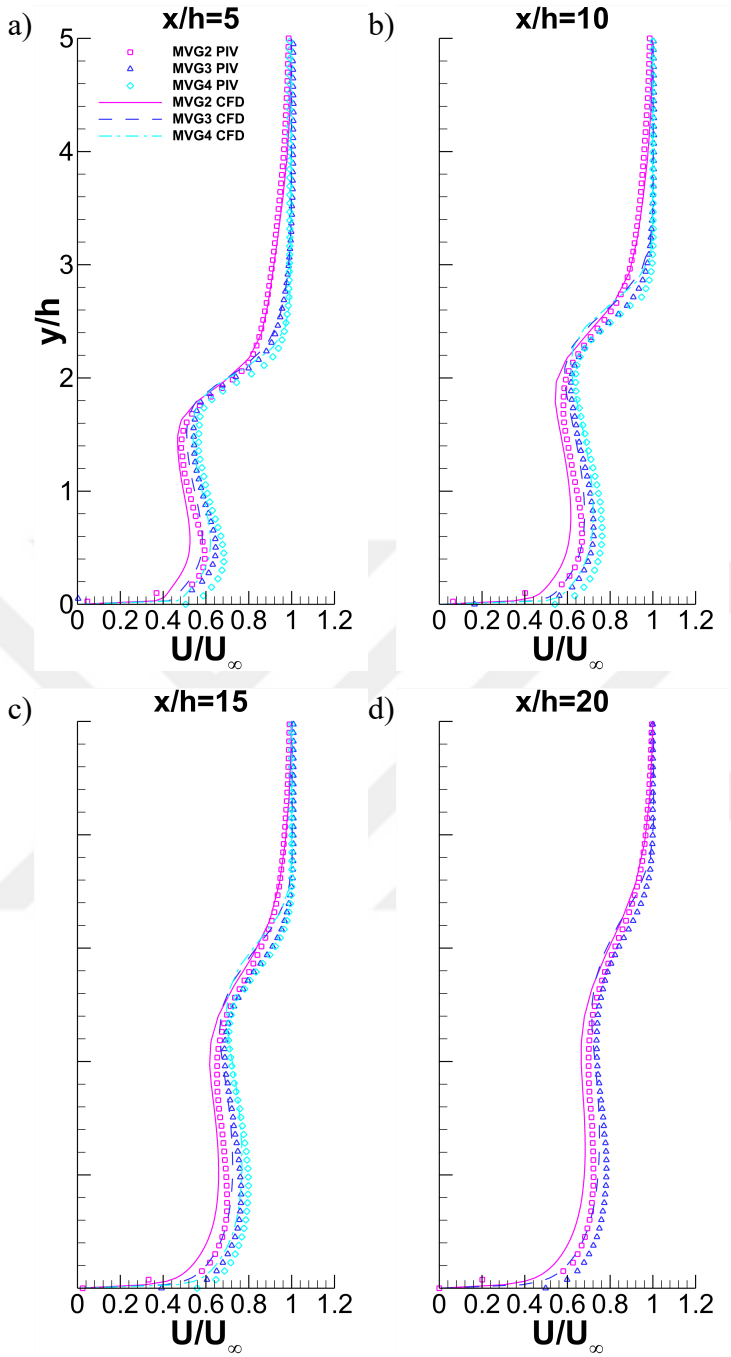

Figure 4.6 The comparison of simulation and experimental results in terms of normalized streamwise velocity. a) x/h=5, b) x/h=10, c) x/h=15, d) x/h=20.

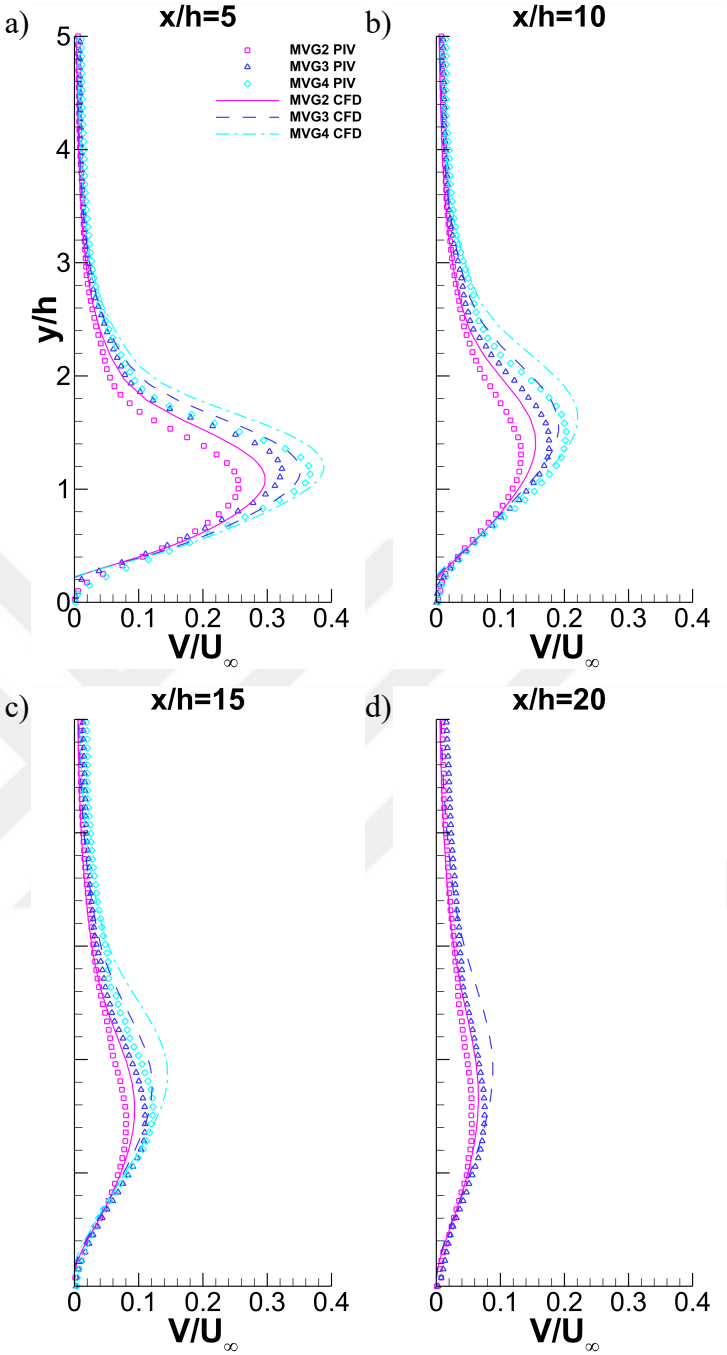

Figure 4.7 The comparison of simulation and experimental results in terms of wall-normal velocity. a) x/h=5, b) x/h=10, c) x/h=15, d) x/h=20.

The comparison of the results of numerical simulations and experiments in terms of the out-of-plane vorticity component (Ω_z) normalized by the height of MVGs and

the freestream velocity is given in Figure 4.8. Figure 4.8 also includes the profiles for MVG2, as the validation for MVG2 was only done for streamwise and wall-normal velocity components before. A satisfactory match is observed in the general profiles; however, similar to the streamwise velocity profiles, the values of the out-of-plane vorticity component are slightly underpredicted below y/h=1. For the maxima of the positive and negative values of the out-of-plane vorticity, a good agreement is achieved between the numerical simulation and experimental results. However, further downstream, the position of the minimum values (negative) is overpredicted by approximately 5%.

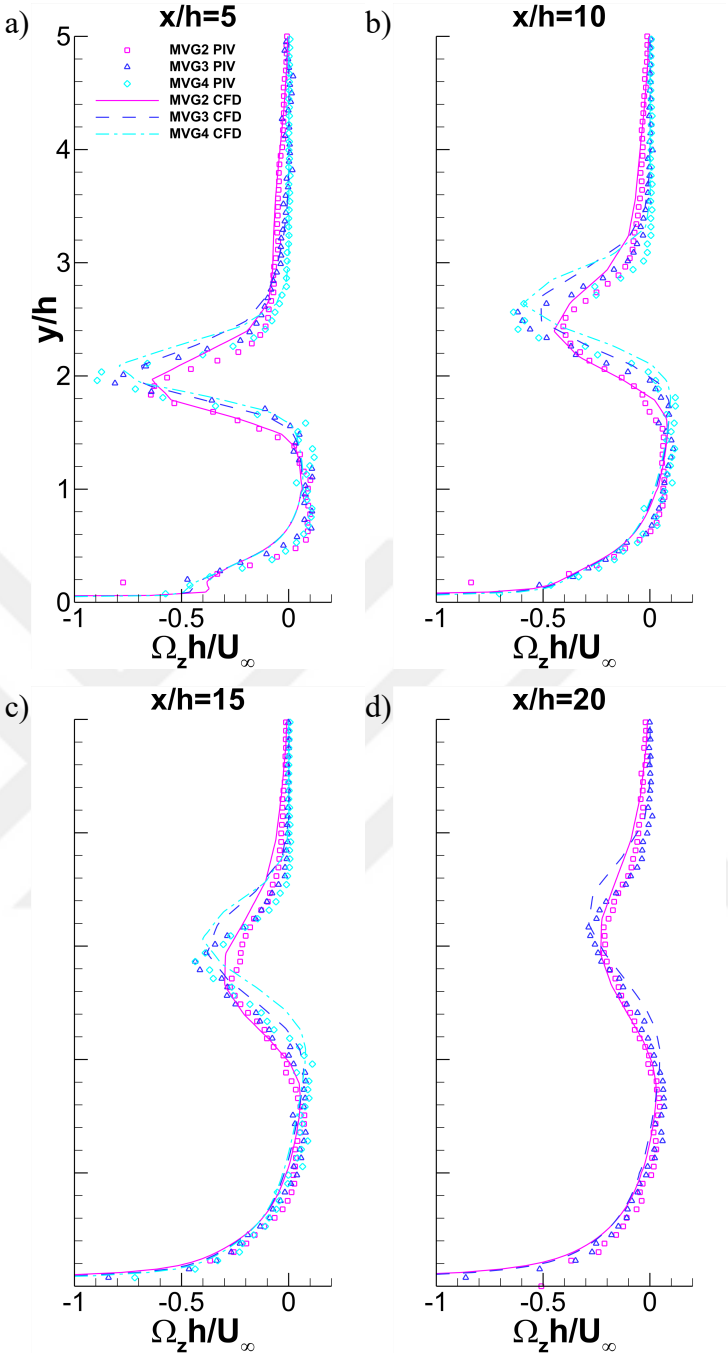

Figure 4.8 The comparison of simulation and experimental results in terms of normalized out-of-plane vorticity component. a) x/h=5, b) x/h=10, c) x/h=15, d) x/h=20.

CHAPTER 5

DECAY OF MVG WAKE AND THE HEIGHT EFFECT

The decay of ramp-type MVG wake is investigated for MVGs having five different h/δ ratios, emphasizing the effect of the device height. As mentioned before, the maximum dimensionless streamwise distances covered by the experimental measurements for MVG2, MVG3, and MVG4 are 39, 23, and 16 x/h, respectively (Figure 2.8). Therefore, the results of numerical simulations are employed to conduct a more comprehensive investigation of the height effect. Moreover, with the addition of two more MVGs, namely MVG5 and MVG6, the investigation regarding the height effects is extended. The height effects are investigated in terms of the streamwise velocity component, wall-normal velocity component, and out-of-plane vorticity component. However, in order to illustrate the decay of the MVG wakes in a better fashion, streamwise decay of the minimum streamwise velocity values (maximum velocity deficit) and the maximum wall-normal velocity values (maximum upwash velocity) and their positions are plotted for all the MVGs. Those plots include results from two studies conducted at supersonic freestream velocities (M=2) [74, 77], making it possible to compare the wakes of ramp-type MVGs in both subsonic and supersonic regimes. Furthermore, using the results of the three-dimensional numerical simulations to understand the three-dimensional effects of MVG height on the wake, the decay of the velocity components, including the spanwise velocity component (W), are discussed in spanwise planes (z-planes) and the decay of the streamwise vorticity is discussed in streamwise planes (x-planes). Lastly, the height effect on the drag in terms of the drag coefficients is discussed.

5.1 Comparison of MVGs and the Flow Conditions

The MVGs used for the wake decay investigation include the ones used for this study, MVG2, MVG3, MVG4, MVG5, and MVG6, along with two MVGs from Sun [77], namely MR3 and MR4, and three MVGs from Giepman [74], named as G6, G8, and G10 for the sake of comparison. Their properties are given in Table 5.1. The MVGs employed by Sun [77] have the same design as the MVGs used in this study (Figure 2.6). However, the design of the MVGs employed by Giepman [74] is slightly different, with a width of 5.3h and a chord of 6.7h. Some of the MVGs concerned have a comparable h/δ ratio, namely MVG4 and G6, MVG5 and G8, and MVG6, G10, and MR3. Even though the h/δ ratios are somewhat equivalent, the flow conditions of the three studies are different (Table 5.2). Therefore, this study differs from its supersonic counterparts conducted at Mach 2. Due to the subsonic flow conditions, the resulting boundary layer thickness in this study is remarkably higher than the others, as expected. Even though the momentum thickness is also higher than that in the supersonic studies, the subsonic flow conditions also induce a lower Reynolds number based on momentum thickness due to the low freestream velocity of 10.1 m/s.

Table 5.1 Dimensions of MVGs and their corresponding h/δ ratios.

MVG	h [mm]	w [mm]	c [mm]	α [°]	h/δ [-]
MVG2	20	122	138	24	0.18
MVG3	30	183	207	24	0.27
MVG4	40	244	276	24	0.36
MVG5	50	305	345	24	0.45
MVG6	60	366	414	24	0.54
G6 *[74]*	6	31.8	40.2	24	0.35
G8 *[74]*	8	42.4	53.6	24	0.46
G10 *[74]*	10	53	67	24	0.58
MR3 *[77]*	3	18.6	20.7	24	0.58
MR4 *[77]*	4	24.8	27.6	24	0.77

Table 5.2 Flow conditions of the three studies compared.

Study	U_∞ [m/s]	M_∞ [-]	δ [mm]	δ^* [mm]	θ [mm]	Re_θ [-]	H [-]
This Study	10.1	0.03	111.31	8.11	6.74	4016	1.20
Sun *[77]*	519	2	5.20	0.59	0.48	13600	1.23
Giepman *[74]*	493	2	17.30	2.10	1.70	67450	1.24

5.2 Decay of the Velocity Components

5.2.1 The Decay of Streamwise Velocity

The streamwise development of the streamwise velocity component (U) normalized by the freestream velocity is given in Figure 5.1 for MVG2 to MVG6 at various streamwise stations up to x/h=30. The maximum velocity deficit (U_{min}) values and their positions increase with the increasing device height. For example, at x/h=5, the maximum velocity deficit is 40% and 56% of the freestream velocity for MVG2 and MVG6, respectively. Moreover, the profiles show that the values of the maximum velocity deficit increase as the wake progresses downstream. In order to show these effects in a better fashion, the plot of decay of the maximum velocity deficit is given in Figure 5.2 (a). It was observed that the offset between the values of the maximum velocity deficit decreases as the MVG height increases, indicating that as the MVG height increases, the decay of the maximum velocity deficit starts to collapse. For example, at x/h=5, the maximum velocity deficit generated by MVG2 is 79.5% of that generated by MVG6, whereas, at x/h=20, it is 83.5%; however, for MVG5, the same percentages are 95.5% and 96.5%, respectively. Figure 5.2 also includes the supersonic results; the same general trend is recorded for both subsonic and supersonic results. Moreover, as the offsets between the curves decrease, i.e., as the MVG height increases, the curves start to collapse with the supersonic results for MVG5 and MVG6, with h/δ ratios of 0.45 and 0.54, whereas the MVGs at Mach 2 have h/δ ratios of 0.35, 0.46, and 0.58 for Giepman [74]; and 0.58 and 0.77 for Sun [77]. However, for the decay of the position of the maximum velocity deficit, the supersonic curves seem more dispersed than the decay of the maximum velocity deficit itself Figure 5.2. As the device height increases, a more substantial increase

is observed in the position of the maximum velocity deficit compared to the increase in the maximum velocity deficit itself. For example, the position of the maximum velocity deficit for MVG2 is 90% of that for MVG6, whereas at x/h=20, it is 65%. This is especially valid for MVG5 and MVG6, for which the increase in the position of the maximum velocity deficit seems to be going on further downstream. However, for smaller devices, i.e., MVG2, MVG3, and MVG4, the increase of the position of the maximum velocity deficit comes to a stop much earlier. The streamwise position, where the increase in the position of the maximum velocity deficit stops, increases with increasing device height, highlighting the fact that with smaller devices, the streamwise vortex pair decays faster. The same effect is observed with the Mach 2 data as the increase with MVGs having smaller h/δ ratios seems to be slowing down further downstream. Also, it should be noted that for the MVG with an h/δ ratio of 0.77 (MR4), the increase in the position of the maximum velocity deficit is still going on further downstream.

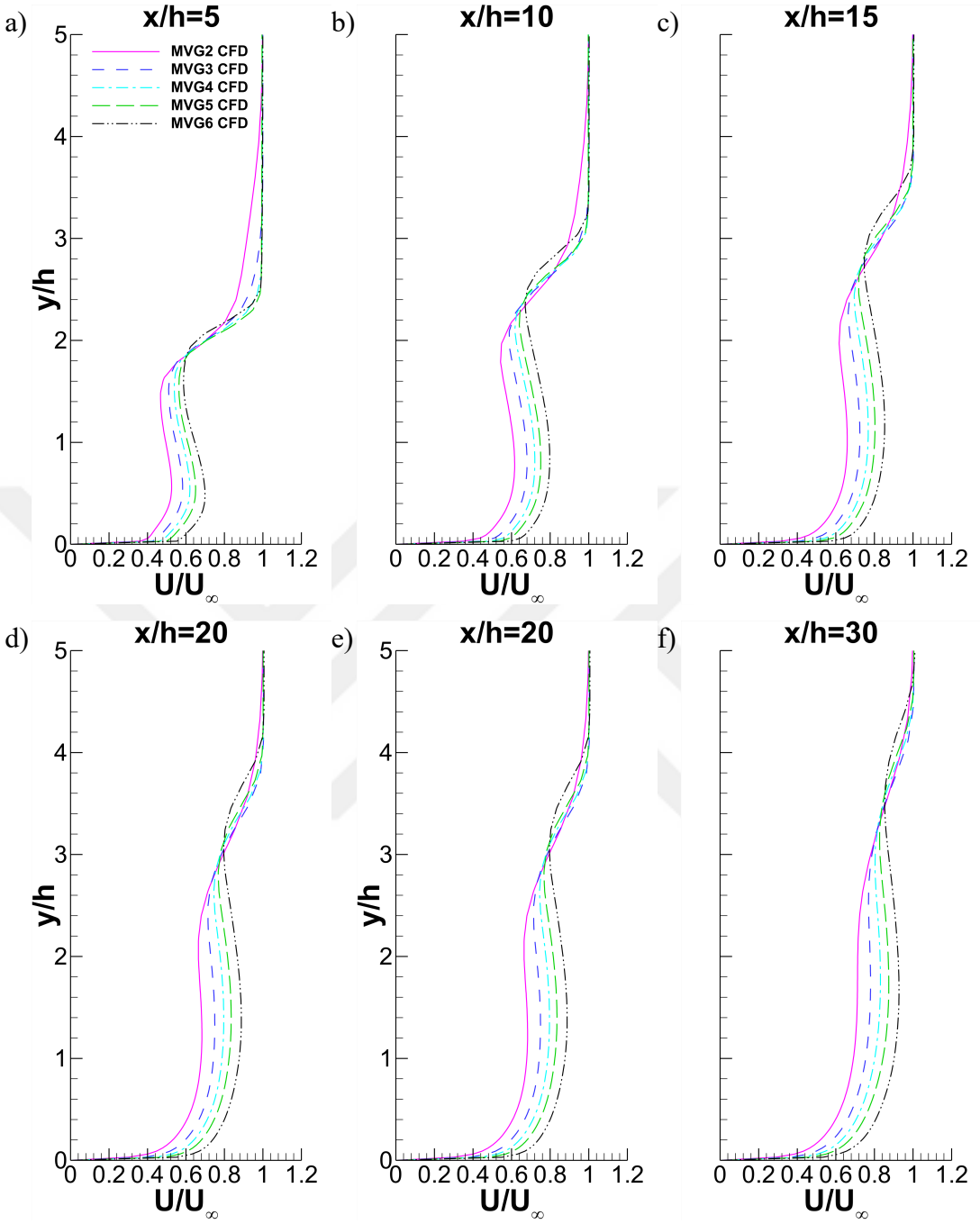

Figure 5.1 The streamwise development of the normalized streamwise velocity (U) at various streamwise stations.

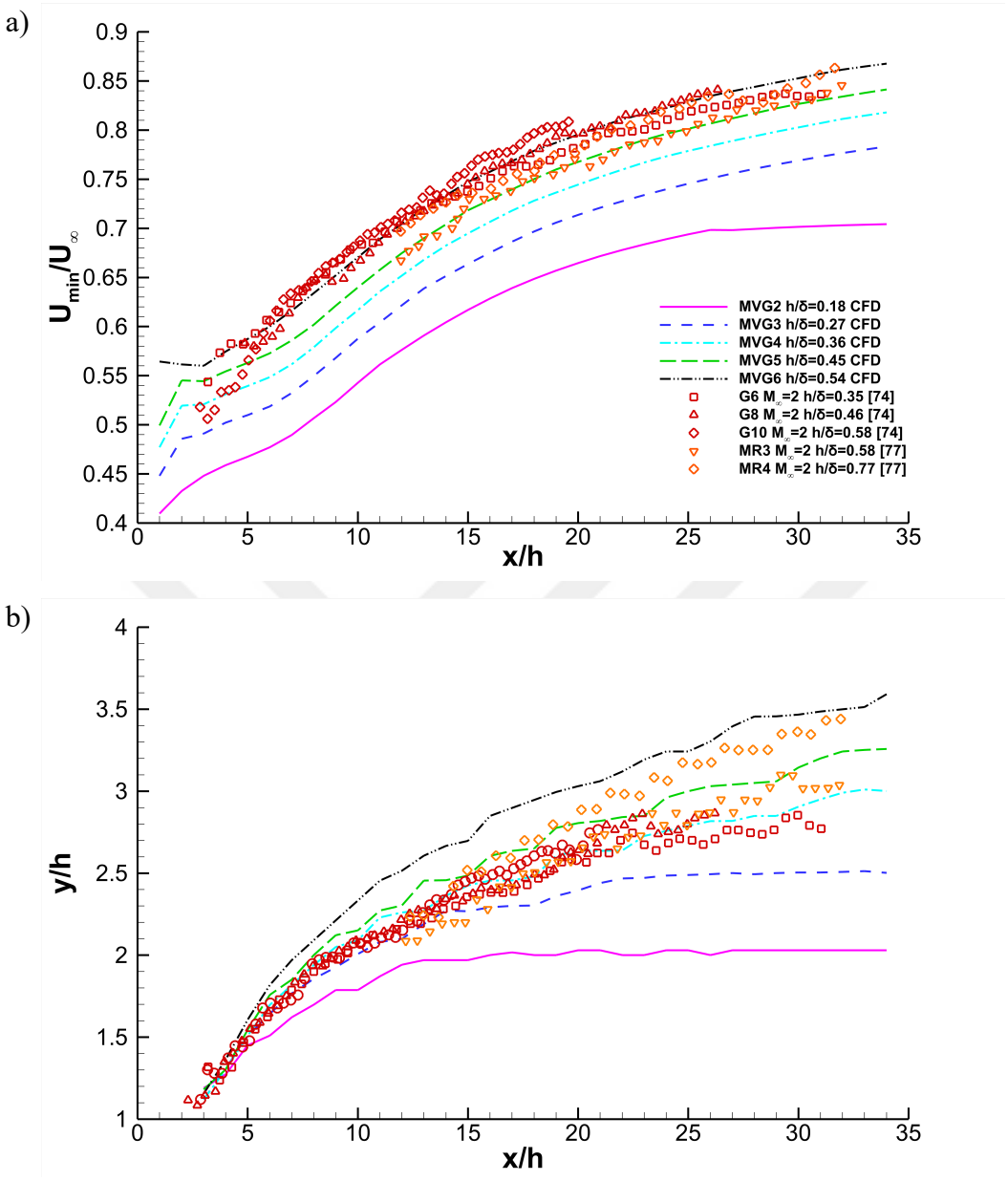

Figure 5.2 The decay of the properties of the streamwise velocity component: a) the decay of maximum velocity deficit, b) the decay of the position of maximum velocity deficit.

5.2.2 The Decay of Wall-Normal Velocity

The streamwise development of the wall-normal velocity component (V) normalized by the freestream velocity is given in Figure 5.3 for MVG2 to MVG6 at various streamwise stations up to x/h=30. As the MVG height increases, the maximum wall-normal velocity (i.e., the maximum upwash velocity) and its position increase in accordance with the experimental results. The maximum upwash velocity decreases as the wake decays further downstream, indicating the decay of the wake. To illustrate this, Figure 5.4 gives the decay of maximum upwash velocity and its position. To quantify, the maximum upwash velocity for MVG2 is 30% and 15% of the freestream velocity, whereas, for MVG6, it is 45% and 28% at x/h=5 and x/h=10, respectively. The positions corresponding to the maximum upwash velocity values are, for MVG2, y/h=1 and y/h=1.4, and for MVG6, y/h=1.3 and y/h=1.8 at x/h=5 and x/h=10, respectively. The Mach 2 data show a collapsing behavior for both the value and the position of the maximum upwash velocity, except the MVG, which has an h/δ ratio of 0.77 (MR4). While the subsonic data do not collapse in general, they seem to collapse with each other and the supersonic data further downstream for the decay of the maximum upwash velocity and at the near-wake region for the decay of its position. As seen from Figure 5.3 and Figure 5.4, the subsonic data do not collapse in general. However, they collapse with each other and with the supersonic data further downstream for the decay of maximum upwash velocity; meanwhile, the curves of the position of the maximum upwash velocity collapse at the near wake region.

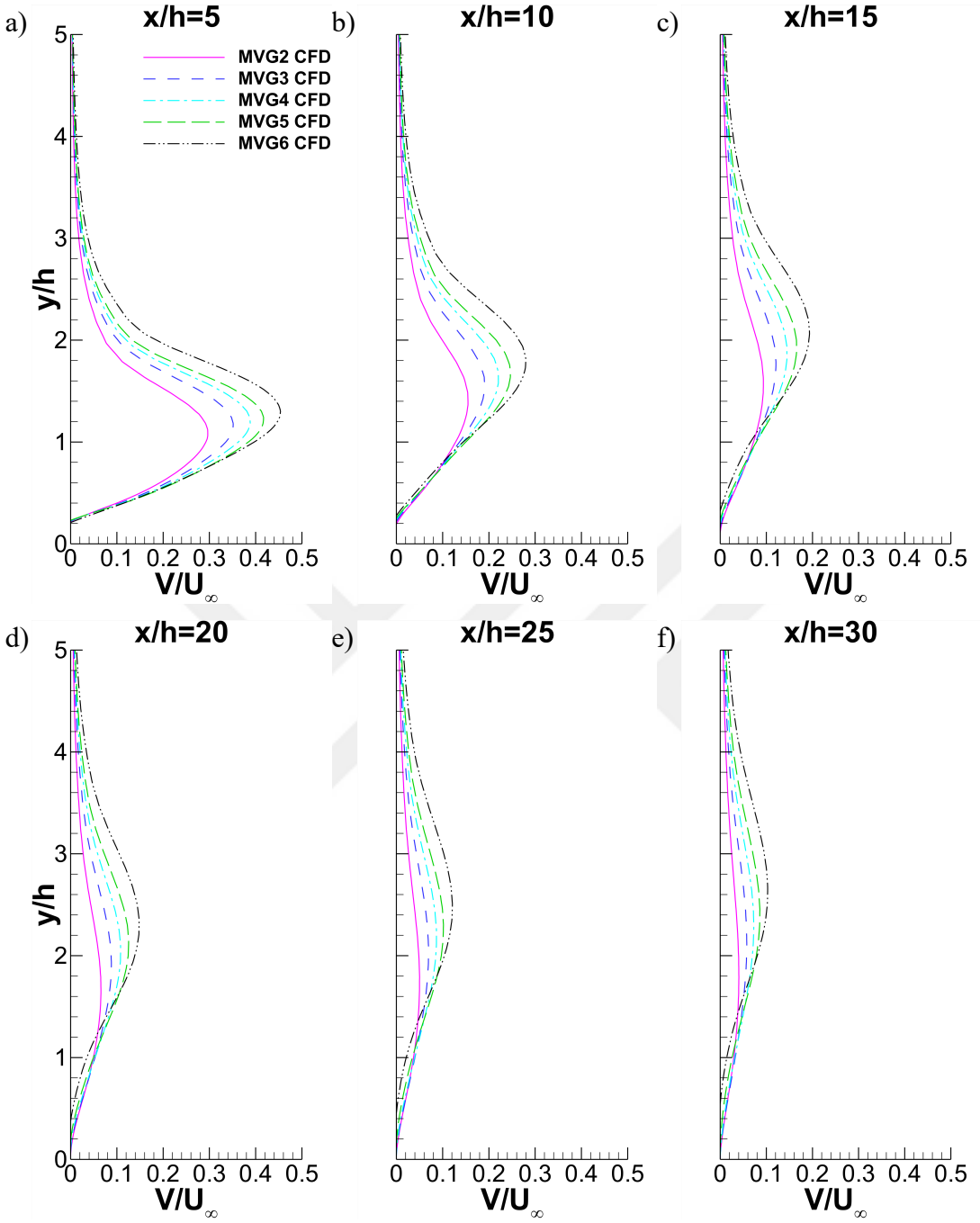

Figure 5.3 The streamwise development of the normalized wall-normal velocity (V) at various streamwise stations.

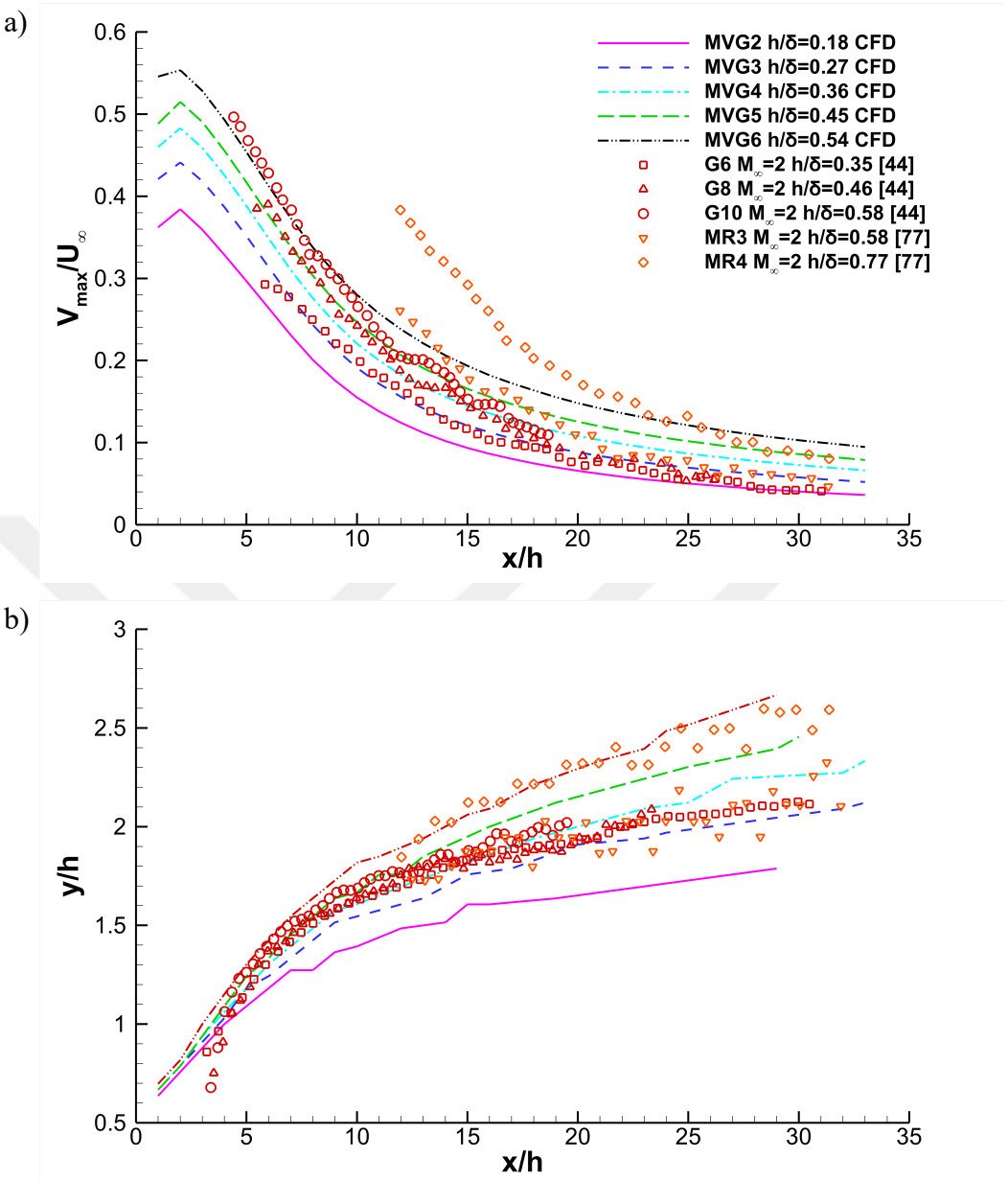

Figure 5.4 The decay of the properties of the wall-normal velocity component; top: the decay of maximum upwash velocity, bottom: the decay of the position of maximum upwash velocity.

5.2.3 Spanwise Investigation of the Velocity Components

The experimental results are acquired only at the streamwise-oriented symmetry plane (z/h=0) of the MVGs, and the numerical simulation results are presented again at the symmetry plane. However, to explore the three-dimensional effects of the MVGs on the wake, other spanwise planes (z-planes) should be investigated, as the three-dimensional numerical simulations allow. The z-planes used in this section are shown in Figure 5.5. They are compared in terms of streamwise, wall-normal, and spanwise velocity profiles (U, V, and W). The spanwise velocity component is not investigated in Chapter 4 since it is expected to be zero at the symmetry plane (z/h=0).

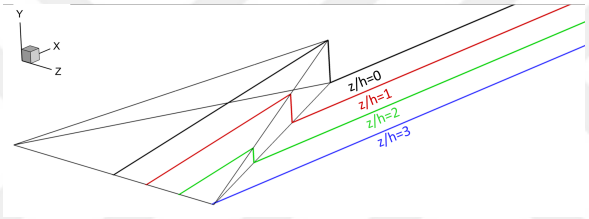

Figure 5.5 Z-planes used for the spanwise investigation.

The velocity profiles of streamwise, wall-normal, and spanwise components at z/h=0 to 3 for all the MVGs are given in Appendix A, with colors marking the z/h stations as seen in Figure 5.5. In order to compare the velocity profiles at different spanwise locations, comparisons are made using MVG2 and MVG6, as they are the smallest and largest MVGs investigated. The streamwise velocity profiles (U) are given in Figure 5.6, the wall-normal (V) velocity profiles are given in Figure 5.7, and the spanwise velocity profiles (W) are given in Figure 5.8. It is obvious that the effects of MVG6 are still not diminished at x/h=30; this fact is shown in sections 5.2.1 and 5.2.2 for the symmetry plane (z/h=0) in terms of streamwise and the wall-normal components. However, the spanwise investigations illustrate that even at z/h=1, the effects of MVG6 are observed on the streamwise and spanwise components seen at the streamwise distance as far as x/h=30. In contrast, the effects of MVG2 are observed to decay much earlier in the wake. For the wall-normal velocity, at z/h=1, the increase in both the value and position of the maximum upwash velocity seems

to be stopped after x/h=25. For the sake of comparison, the velocity profiles at x/h=30 and z/h=1 are plotted together for all the MVGs concerned (Figure 5.9). The diminishing effects of smaller MVGs and the long-lasting effects of larger ones can distinctly be seen along with the diminished wall-normal velocity component.

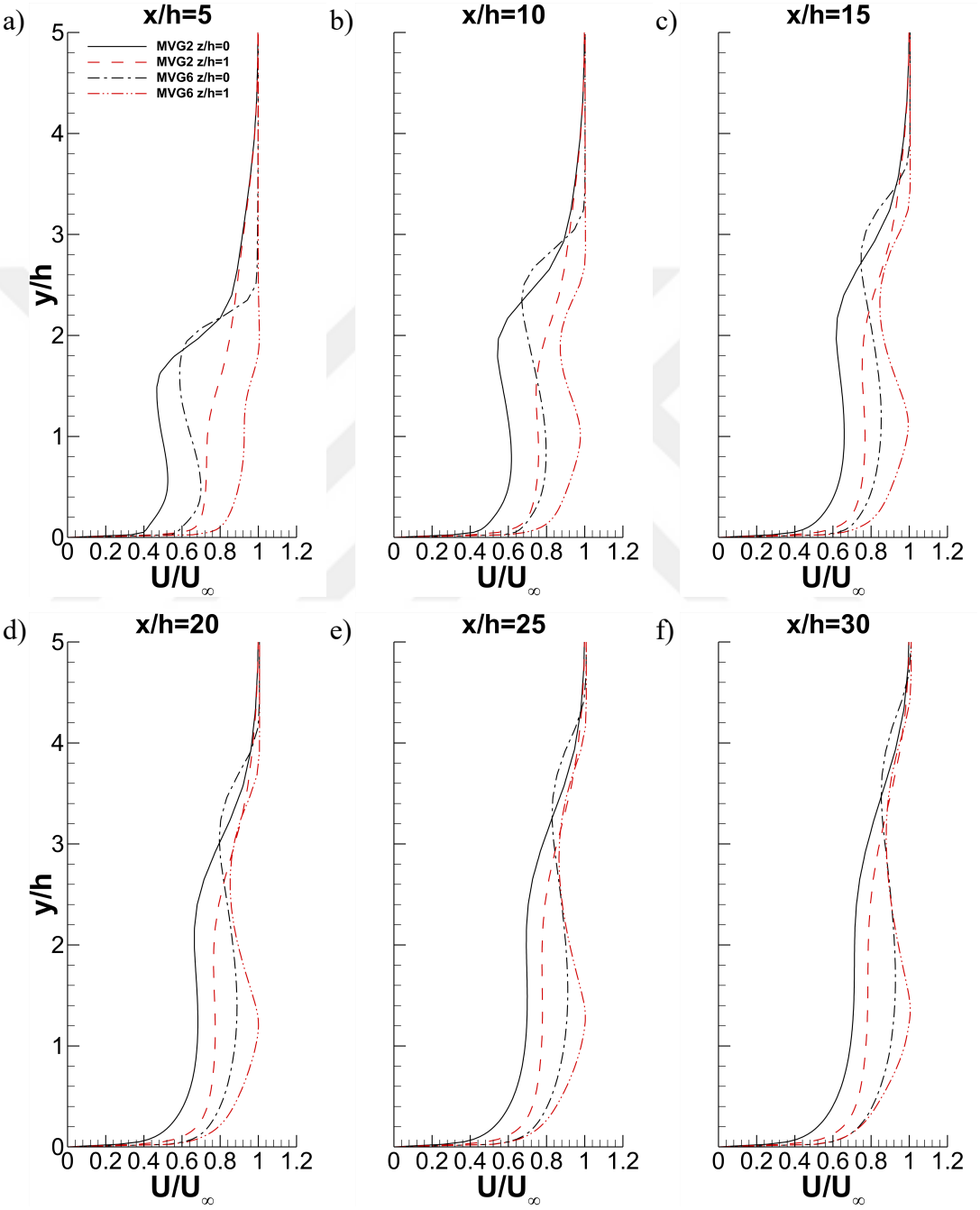

Figure 5.6 Comparison of the streamwise velocity component (U) at z/h=0 (black) and z/h=1 (red) for MVG2 and MVG6 at various streamwise stations.

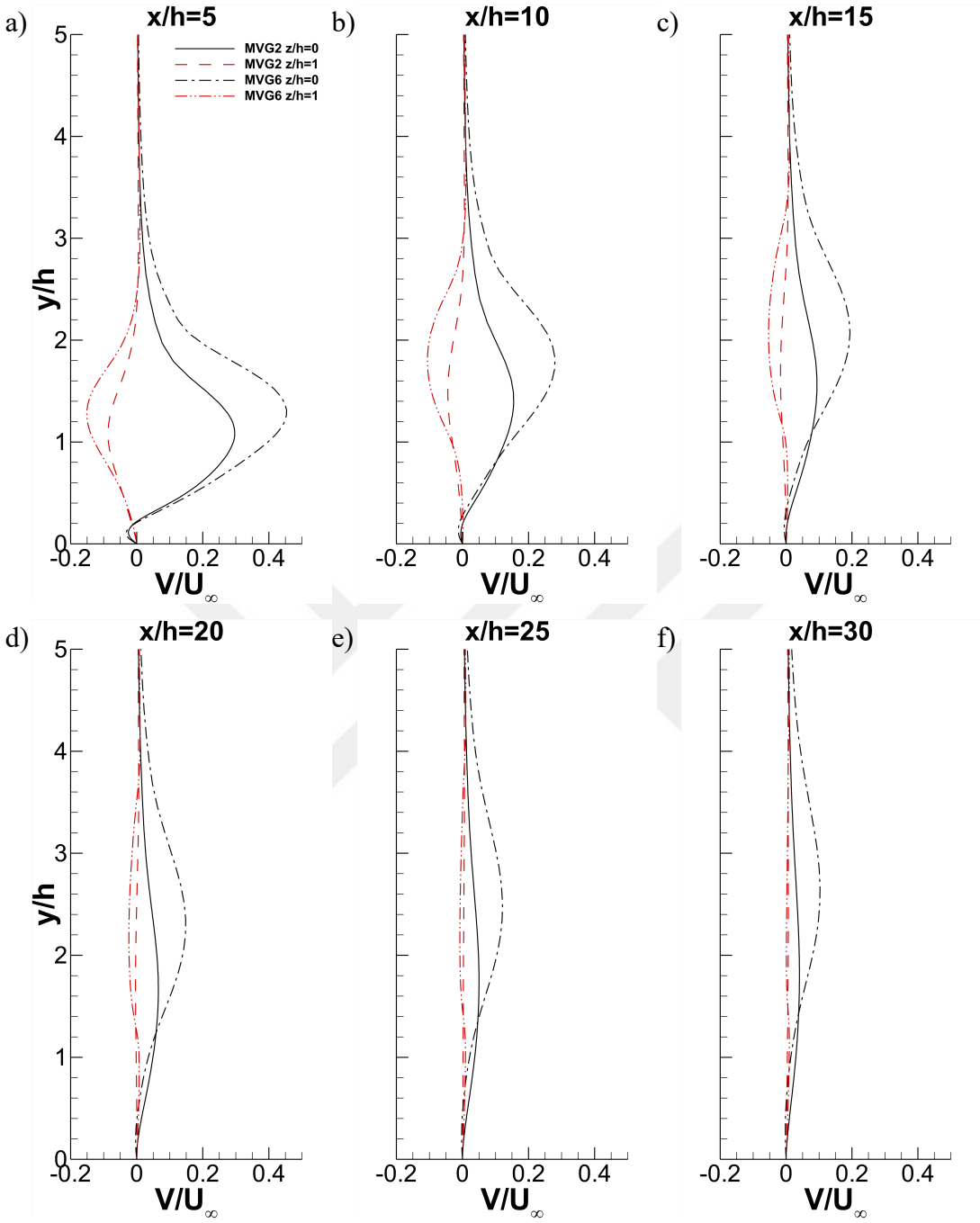

Figure 5.7 Comparison of the wall-normal velocity component (V) at z/h=0 (black) and z/h=1 (red) for MVG2 and MVG6 at various streamwise stations.

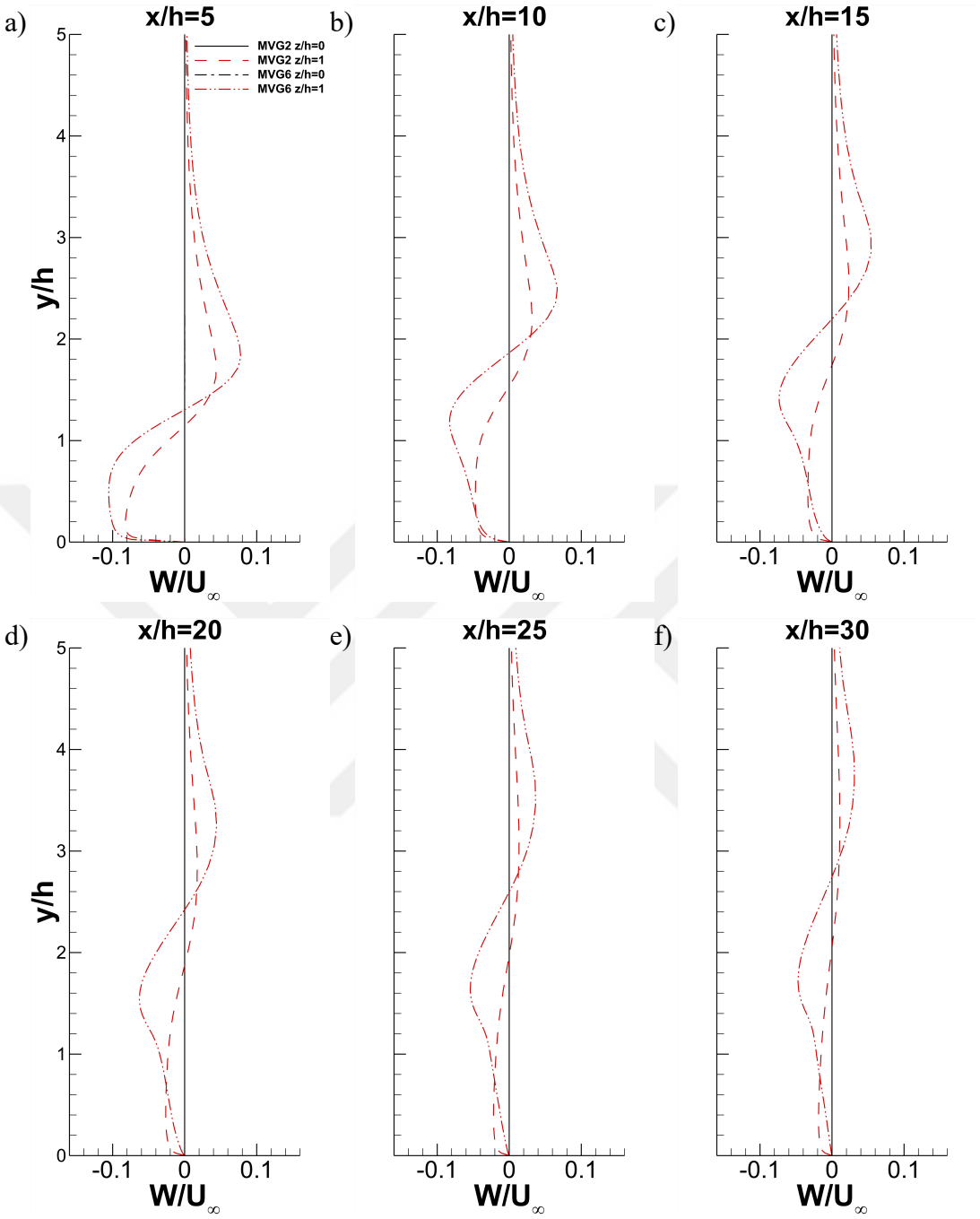

Figure 5.8 Comparison of the spanwise velocity component (W) at z/h=0 (black) and z/h=1 (red) for MVG2 and MVG6 at various streamwise stations.

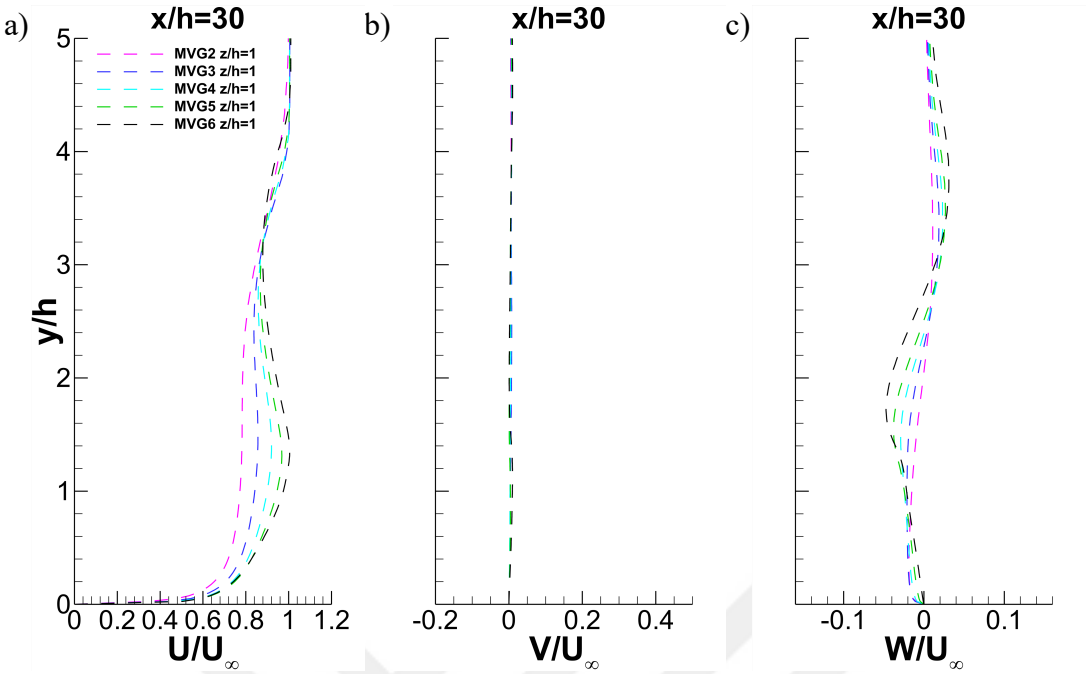

Figure 5.9 Comparison of the streamwise (U), wall-normal (V), and spanwise (W) velocity components at x/h=30 and z/h=1.

5.3 Decay of the Out-Of-Plane Vorticity Component

The height effect is also investigated in terms of the normalized out-of-plane vorticity component ($\Omega_z h/U_\infty$) in Figure 5.10 on the symmetry plane. Both positive and negative peaks of the out-of-plane vorticity component profiles increase in magnitude with increasing device height. As the device height increases, the effects in terms of out-of-plane vorticity persist further in the wake, with the positions of both peaks moving away from the wall. It was seen that the magnitudes of out-of-plane vorticity are nearly equalized at x/h=15 for all the MVGs, except for MVG2, for which the out-of-plane vorticity decays much faster. However, it should be noted that as the device height increases, the locations of both peaks also increase.

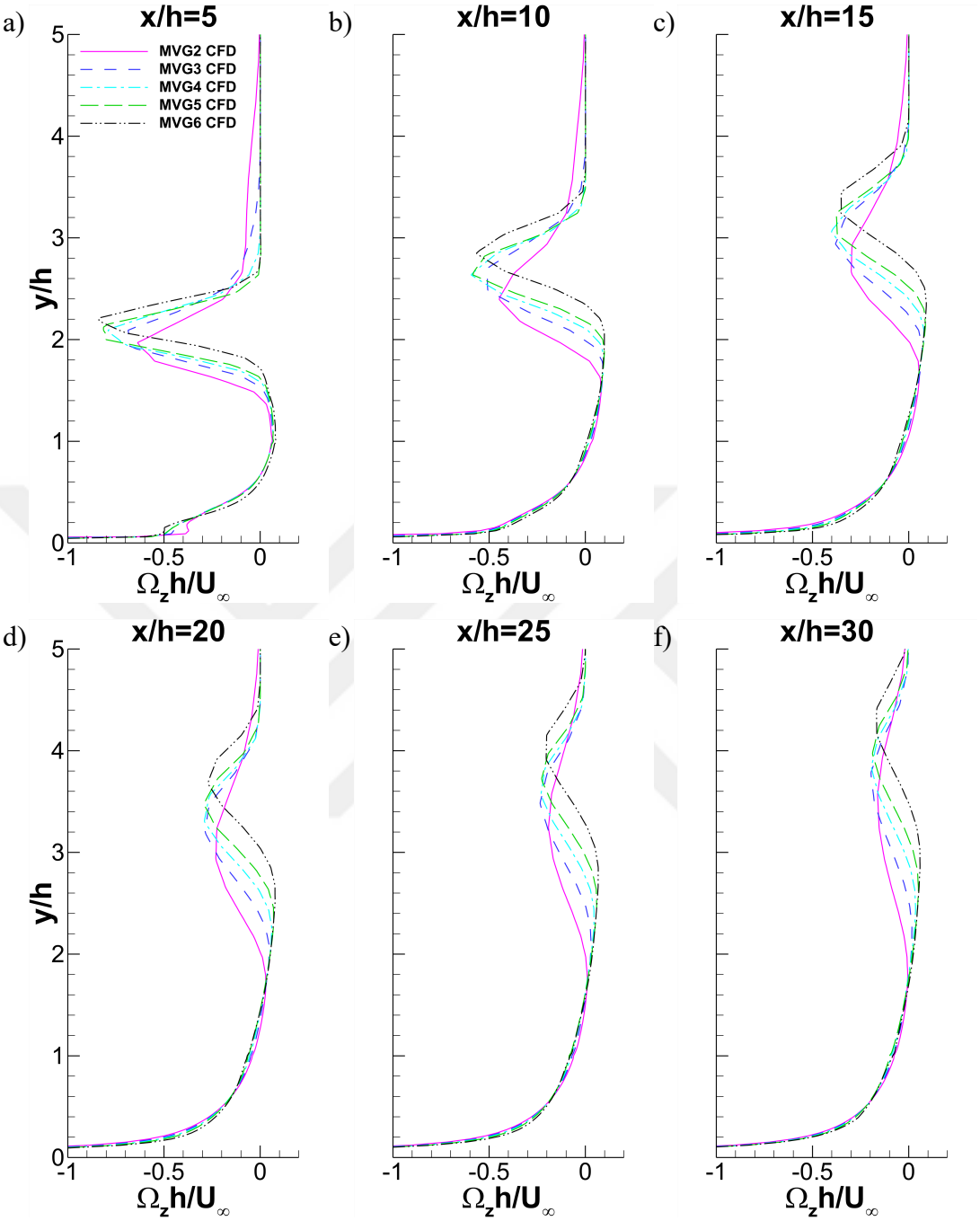

Figure 5.10 Comparison of MVGs of different heights in terms of normalized out-of-plane vorticity component (Ω_z) at various streamwise stations.

5.4 Decay of the Streamwise Vorticity Component

The decay of the normalized streamwise vorticity component ($\Omega_x h/U_\infty$) is shown in x-planes (streamwise planes) in Figure 5.11 at x/h=10 and in Appendix B at x/h=1, 5, and 15. These contours allow us to track the streamwise vortex pair and their lift-off as well as the development and decay of the secondary vortices. The streamwise vortex pair shows their effects as the variation in the vorticity field. An alternating positive and negative vorticity field is seen for both the primary and secondary vortex pairs in the contours. In Figure 5.11, half the boundary layer thickness (0.5δ) and the boundary thickness (δ) are marked with white and red lines, respectively. It should be noted that this investigation is made in terms of normalized distances (x/h, y/h, and z/h). That is the reason why the 0.5δ and δ lines for different MVGs vary in position, as 0.5δ is 55.655 mm and δ is 111.31 mm. The contours show the extent of the effect of the MVGs in terms of lift-off at various x/h planes. For example, in Figure 5.11, it can be observed that at x/h=10, the effects of vortices generated by MVG2 in terms of normalized streamwise vorticity do not reach 0.5δ. In comparison, the effects generated by MVG3 and MVG4 exceed the 0.5δ limit and get closer to boundary layer thickness. However, for MVG5 and MVG6, these effects seem to exceed the boundary layer thickness already. The same effects can be observed from the position of the maximum velocity deficit (Figure 5.2) and the position of the maximum upwash (Figure 5.4).

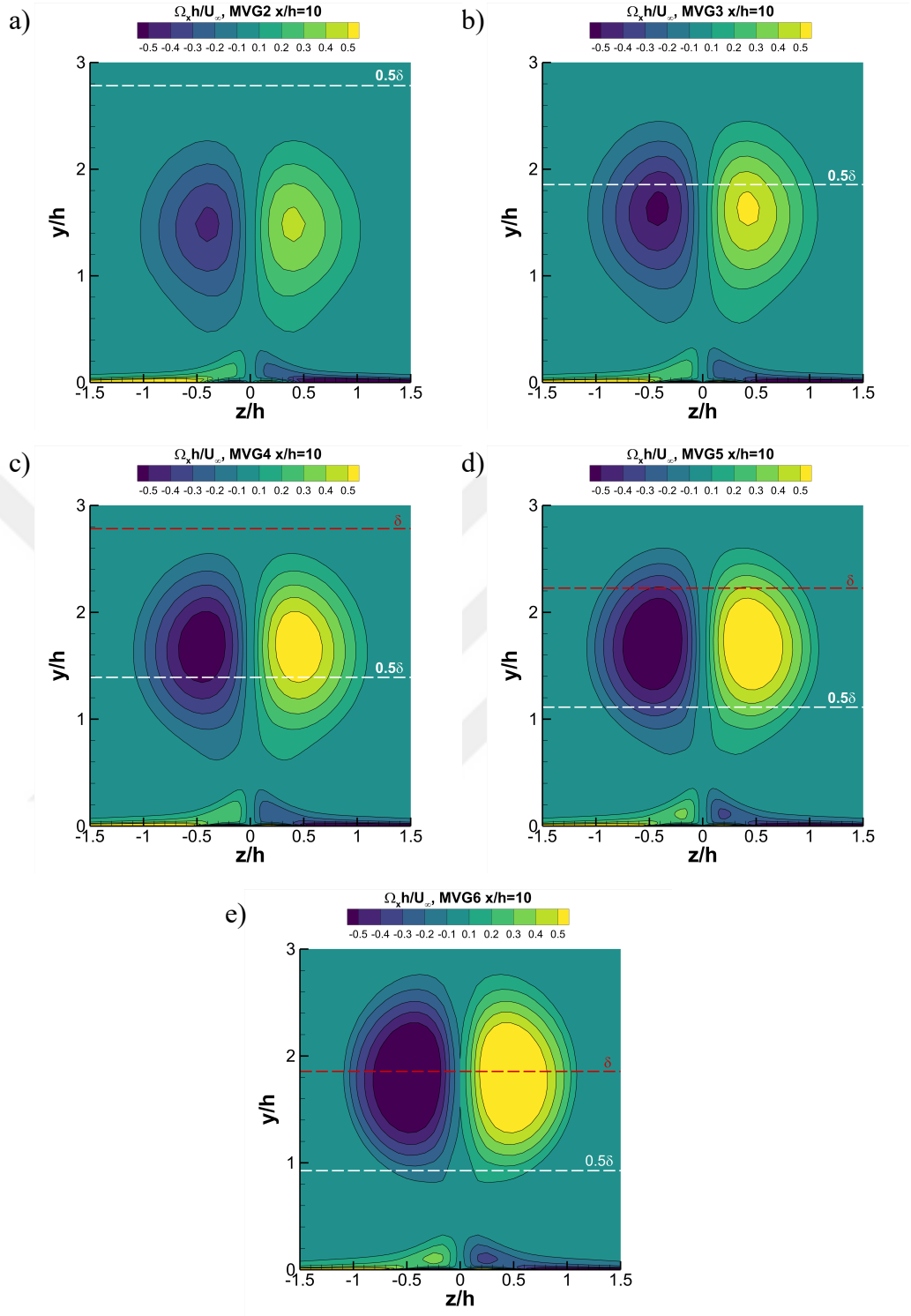

Figure 5.11 Contours of normalized streamwise vorticity component ($\Omega_x h/U_\infty$) shown over x-planes illustrating the counter-rotating vortices at x/h=10 for a) MVG2, b) MVG3, c) MVG4, d) MVG5, e) MVG6.

5.5 Decay of Vortex Strength

The findings regarding the decay parameters are closely associated with the streamwise decay of the vortex pair generated by the MVGs. In order to relate the discussion to the vortex pair, vortex strength, which clearly is a function of device Reynolds number (h^+) and downstream distance (x/h), is given as circulation (Γ) divided by the wall friction velocity of the undisturbed boundary layer (U_τ) and device height (h) [40].

$$\frac{\Gamma}{U_\tau h} = F\left(h^+, {}^{x}/_{h}\right) \quad [4.1]$$

Where the device Reynolds number is defined as,

$$h^+ = \frac{hU_\tau}{\upsilon} \quad [4.2]$$

Figure 5.12 clearly shows that the vortex strength increases with increasing device height. Moreover, the streamwise decay of the vortex strength can also be observed. Figure 5.12 also includes the data from Giepman [74]. In their study, that data were initially used to compare Mach number effects on the MVG wake. The data comprise the same MVG height (8 mm, G8) at different Mach numbers, thus the small change in h/δ ratios. Comparable general trends are recorded for subsonic and supersonic data similar to the other decay parameters discussed, and nearly the same vortex strength value is recorded for M_∞=2 and M_∞=1.5 cases. Although smaller vortex strength values for the M_∞=2.5 case are recorded in the region up to x/h=10, after this streamwise position, the values start to match with the others. As for the comparison with the subsonic data, for streamwise positions higher than x/h=10, the vortex strength values fall between those recorded for MVG5 and MVG6, having h/δ ratios of 0.45 and 0.54, respectively. It should also be noted that the M_∞=2.5 data shows a better match with MVG5 and MVG6.

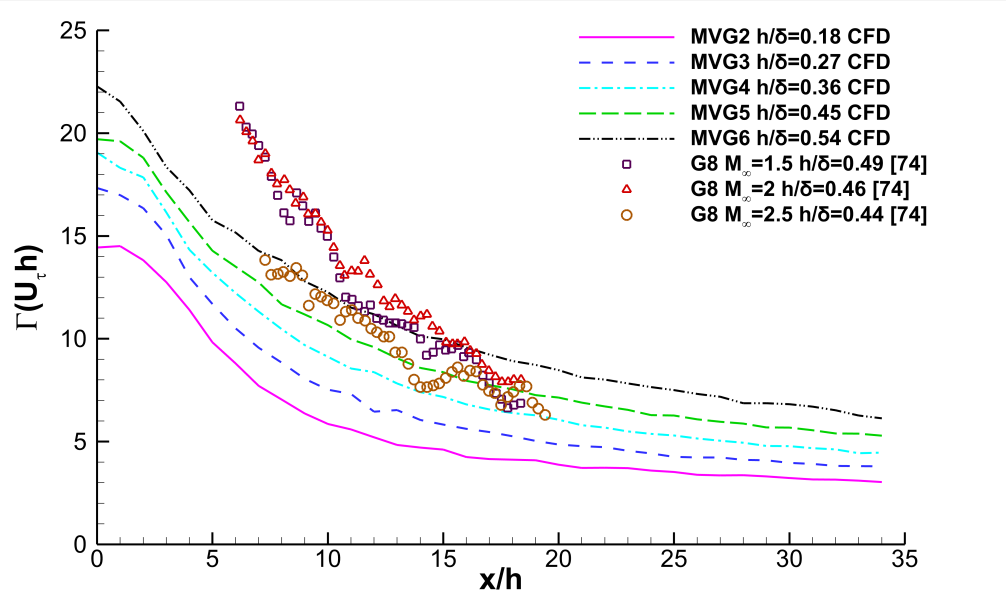

Figure 5.12 Decay of vortex strength compared with the supersonic data from [74] at different Mach numbers.

Ashill *et al.* [42] found that the vortex strength of MVGs having an effective device Reynolds number higher than 1400 falls into a single line. The effective device Reynolds number is calculated by using the effective height (h_e), which is found by equalizing the maximum vortex strength at five device heights downstream of the MVG ($\Gamma_5/U_\tau h$) to a single point using Figure 5.13.

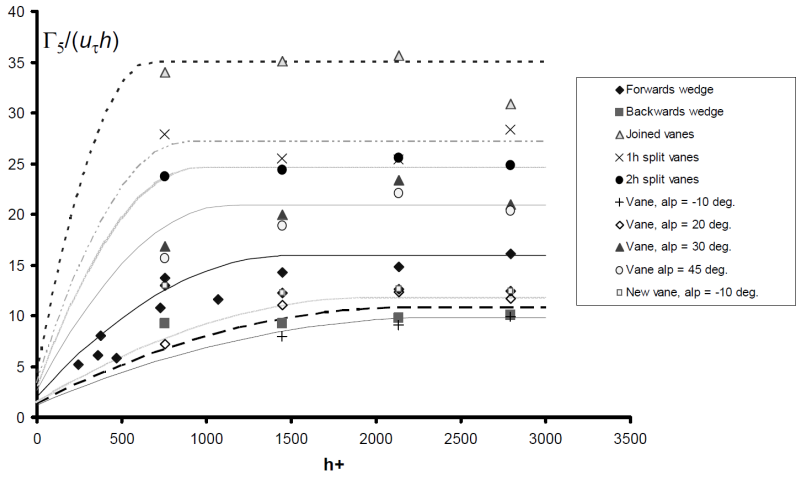

Figure 5.13 Non-dimensional circulation versus device Reynolds number for different MVGs at five device heights downstream of the MVGs [40].

They used the Forwards Wedge (ramp-type MVG) as the datum for that, so, for example, for the Joined Vanes type of MVG, the effective height is 2.2 times its actual height, whereas the effective height for the ramp-type MVG is the same as its actual height. Subsequently, when the vortex strength and device Reynolds number are calculated using the effective height, the resulting distribution is seen in Figure 5.14, which also includes the calculations for MVGs used in this study. Effective device Reynolds numbers for the MVGs used in this study are given in Table 5.3; for all MVGs, the effective Reynolds number is below 1400. Therefore, circulation of the vortices, hence the strength of the vortices, is not expected to scale with device height. In order to have a device with h_e^+=1400 for the undisturbed boundary layer investigated in this study, one must have an MVG with a device height of 66 mm, corresponding to a height-to-boundary layer thickness ratio of 0.59.

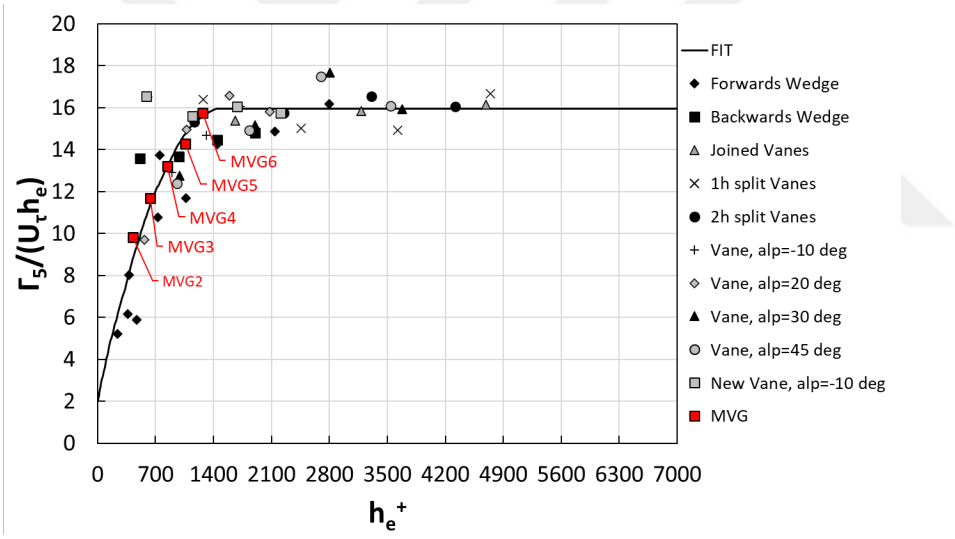

Figure 5.14. Vortex strength against the device Reynolds number using the effective device height [40].

Table 5.3 Effective Reynolds numbers for MVGs used in this study.

MVG	h [mm]	h/δ [-]	he^+ [-]
MVG2	20	0.18	423
MVG3	30	0.27	635
MVG4	40	0.36	847
MVG5	50	0.45	1058
MVG6	60	0.54	1270

5.6 Conclusion on the Height Effect Discussion

In this section, the effect of device height is discussed in terms of the velocity components and their decay. Moreover, the decay behaviors of the velocity components are investigated in various spanwise planes (z-planes), and the vortex pairs are examined in terms of streamwise vorticity components in streamwise planes (x-planes). Another critical aspect of the effect of the device height is the drag these devices induce. The plot of the drag coefficient versus the h/δ ratio given in Figure 5.15 shows a substantial increase in the drag coefficient with increasing device height.

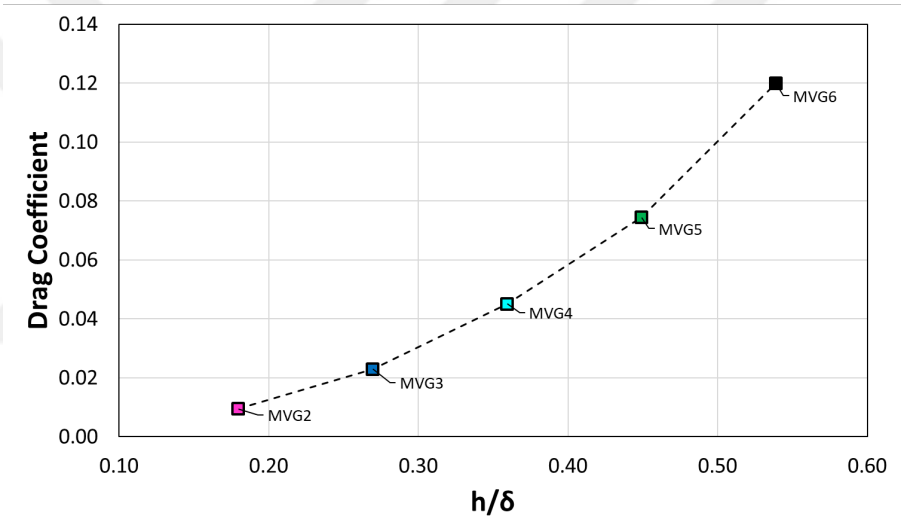

Figure 5.15 Drag coefficient versus the h/δ ratio.

The discussion in the previous sections regarding the height effects reveals that selecting the optimum MVG height is crucial and that there is one more caveat besides the drag forces added. As stated in the introduction section of this thesis, one of the main advantages of having a Micro Vortex Generator is to employ effects to control the boundary layer. After the boundary layer control is successful, their effects are removed since the vortices generated by MVGs decay well before compared to vortices generated by conventional vortex generators. If the decay is not complete after the downstream location where the boundary layer is required to be controlled, the lasting vortices would add an excess of three-dimensional effects. As seen from the plots (Figure 5.2 and Figure 5.4) and contours (Figure 5.11) given

in the height effects discussion, the larger the MVG, the further downstream its effects persist. These effects are also present in the spanwise planes outside the symmetry plane (Figure 5.6, Figure 5.7, and Figure 5.8). Moreover, when the positions of the vortex core centers are investigated, it can be seen that not only the effects of the streamwise vortex pair but also even the vortex core centers may exceed the undisturbed boundary layer thickness further downstream. This is illustrated in Figure 5.16 by plotting the vortex core centers, which are the locations of the minimum helicity [88], with respect to the coordinates nondimensionalized by the boundary layer thickness. For example, the vortex core centers do not exceed the boundary layer thickness up to $x/\delta=15$ for MVG2, MVG3, and MVG4; however, for MVG5, the cores of the streamwise vortex pair exceed the boundary layer thickness at $x/\delta=12.5$, and for MVG6 they exceed the boundary layer thickness at $x/\delta=6$.

This finding is usually given when comparing conventional vortex generators to micro vortex generators [38]; however, it is safe to make the same comparison between MVGs with different heights. Therefore, to avoid the excessive effects caused by the persisting vortices, an MVG height creates streamwise vortices just strong enough to overcome the separation, with less added drag as an extra benefit.

The device height, i.e., the h/δ ratio, is also influential regarding the similarity level of the wakes of ramp-type MVGs in subsonic conditions to their supersonic counterparts. As shown in the investigation of the decay parameters for the subsonic wake, as the h/δ ratio increases, the level of similarity to their supersonic counterparts is also increased. This is explained by the effective device Reynolds number getting closer to the level ($h_e^+=1400$) where the vortex strength of the MVGs falls into a single line. However, the maximum device Reynolds number for this study is approximately 1300 (MVG6), and it is known that the device Reynolds numbers for Sun [77] and Giepman [74] are well above 1400. It is concluded that for the values of the device Reynolds number that are higher than or close to a particular value, it is possible to create similar wakes regardless of the Mach number.

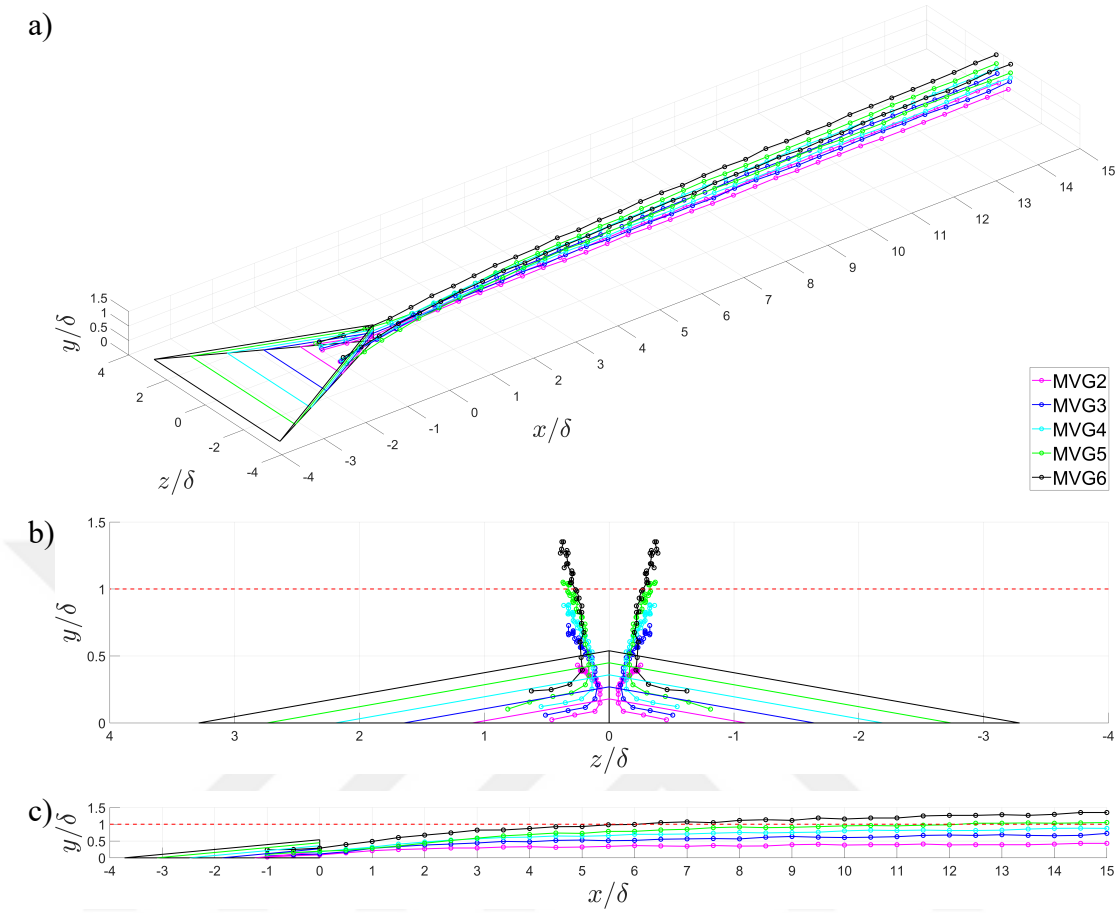

Figure 5.16 The locations of the vortex centers for MVG2, MVG3, MVG4, MVG5, and MVG6, boundary layer thickness shown with dashed red lines. a: 3D view, b: front view, c: side view.

CHAPTER 6

THE RAMP-TYPE MVG WAKE MODEL

The wake decay parameters discussed in Chapter 5 suggest that the ramp-type MVGs might be self-similar. Velocity profiles of ramp-type MVGs are scaled and shown to be self-similar in supersonic freestream velocities by Sun [77]. The self-similarity of the velocity profiles of ramp-type MVGs in subsonic freestream conditions is investigated by employing a similar scaling method to Sun [77]. Moreover, using the scaling equations derived from the subsonic results, a wake model named the Ramp-Type MVG Wake Model is suggested. The model is constructed using the experimental results for MVG2, MVG3, and MV4 with the addition of the numerical results for MVG5 and MVG6 in order to have more h/δ ratios included. Employing the suggested model, streamwise and wall-normal velocity profiles for MVGs used by Sun [77] and Giepman [74] are reconstructed and compared with the experimental results. In short, this part explains and discusses a way to model an MVG in supersonic flows using the results of subsonic studies.

6.1 Self-Similarity of the MVG Wake

The velocity profiles of MVGs can be scaled to show a self-similar collapsing profile, as demonstrated by Sun [77]. However, this study will employ a similar method to scale the velocity profiles using a different length scale.

For the streamwise velocity profiles, the scaling procedure and the parameters used for scaling are shown in the sketch in Figure 6.1. The velocity profiles are subtracted from the undisturbed boundary layer. The absolute value of the resulting maximum velocity deficit (Equation 6.2) is used as the velocity scale.

$$U_{Def} = |U_{BL} - U|_{max} \quad [6.1]$$

$$\overline{U} = \frac{U_{BL} - U}{U_{Def}} \quad [6.2]$$

For the normalization of the y-coordinate, the streamwise velocity profiles are shifted so that the maximum velocity deficit is at y=0 (Equation 6.3). In order to do that, a constant factor called y^* is used, which only governs the width on the normalized streamwise velocity component distribution (Figure 6.3) and the wake width (w_U), which is the wall-normal distance between the wall-normal positions corresponding to the first inflection point (U_1), in the reconstructed profiles (Figure 6.1). The constant y^* can take any value as long as self-similarity is achieved.

$$\overline{y} = \frac{y - y_{Udef}}{y^*} \quad [6.3]$$

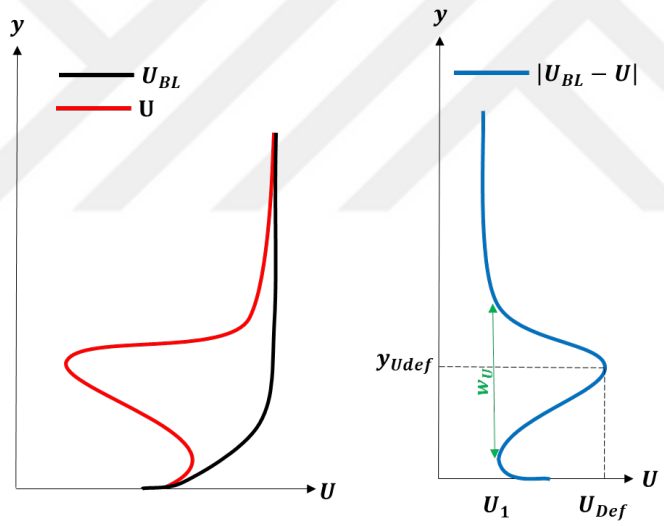

Figure 6.1 Sketches showing the subtraction of the streamwise velocity profile from the undisturbed boundary layer profile and the parameters used to scale the streamwise velocity profiles.

In the case of wall-normal velocity profiles, the scaling parameters are given in Figure 6.2. The maximum upwash velocity is used as the velocity scale, shown in Equation 6.4, and the resulting term is the normalized wall-normal velocity ($\bar{V}$).

$$\bar{V} = \frac{V}{V_{max}} \quad [6.4]$$

Furthermore, the velocity profile can be shifted in such a way that the maximum upwash velocity is at the zero wall-normal position (Equation 6.5) to account for the varying lift-off characteristics of different MVGs, the amount of shifting corresponds to the wake width (w_V). The wake width is calculated using a cut-off factor (k), which can take any value between 0 and 1, i.e., k can take any value that corresponds to a meaningful wake width.

$$w_V = y_{V2} - y_{V1} \quad [6.5]$$

To define the length scale, normalized maximum upwash velocity and wake width are used (Equation 6.6), where y_{Vmax} is the position of the maximum upwash velocity.

$$\bar{y} = \frac{y - y_{Vmax}}{w_V} \quad [6.6]$$

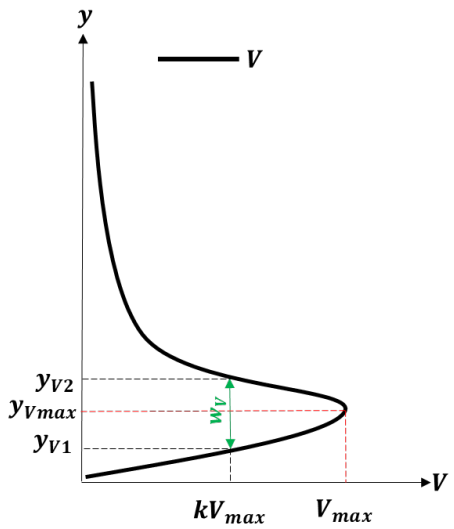

Figure 6.2 Sketch showing the scaling parameters for the wall-normal velocity component.

The normalization procedures for the streamwise and wall-normal velocity profiles are applied to the experimental results, and the resulting normalized curves for the streamwise and wall-normal velocity profiles at x/h=5, 10, 15 for all MVGs including x/h=20 for MVG2 and MVG3 are given in Figure 6.3. The normalized curves show that ramp-type MVGs exhibit self-similar behavior in terms of velocity profiles at subsonic freestream velocities with a Gaussian distribution.

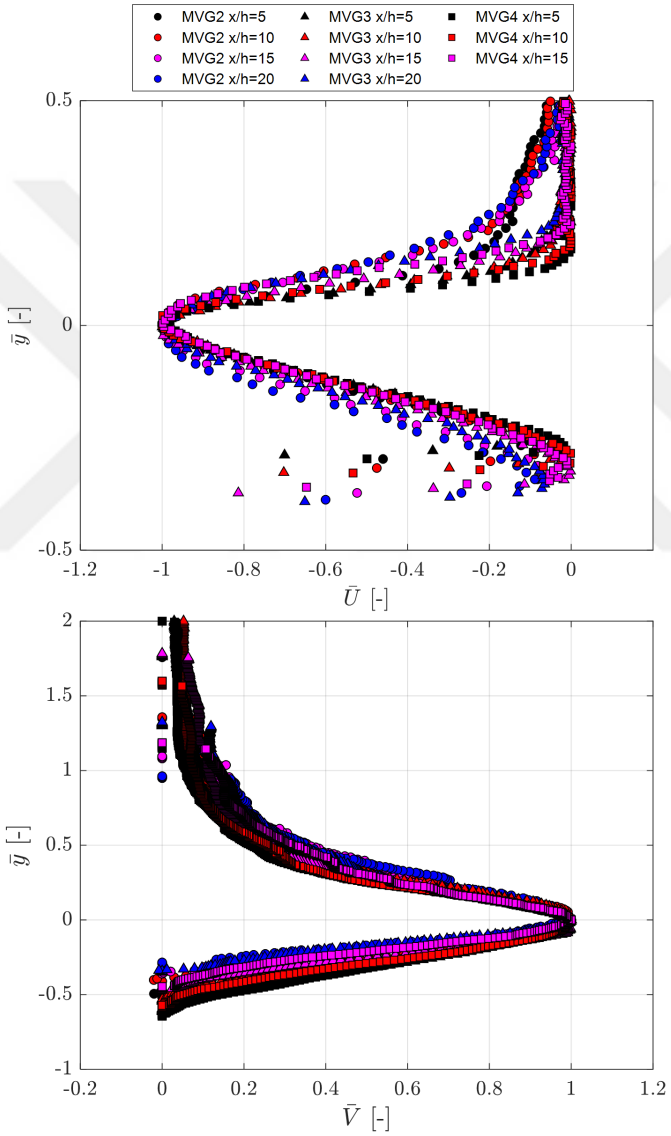

Figure 6.3 Normalized profiles for the streamwise velocity component (top) and the wall-normal velocity component (bottom).

6.2 Modeling of the Ramp-Type MVG Wakes

As the wakes of ramp-type MVGs are shown to be self-similar in terms of streamwise and wall-normal velocity profiles (Figure 6.3), the wake itself is modeled using a set of equations. A part of the mentioned equations is derived by fitting curves to various decay parameters. The curves are fit for the region x/h=10 to x/h=20 since the general trends of the decay curves are similar in that region. The model is named the Ramp-Type MVG Wake Model and is constructed using the experimental results for MVG2, MVG3, and MVG4; however, in order to extend the model to include more h/δ ratios, the numerical results of MVG5 and MVG6 are added. The model for both streamwise and wall-normal velocity components is constructed as follows,

1. Curves are fit for the decay parameters such that the curve-fitting equations with respect to x/h are in the form of

$$Decay\ Parameter = Coefficient\left(\frac{x}{h}\right)^{Power} \quad [6.7]$$

2. The coefficients for each decay parameter are found for each MVG in order to account for the h/δ ratio, then fit equations for coefficients for each decay parameter obtained in the form of:

$$Coefficient = ct_1\left(\frac{h}{\delta}\right) + ct_2 \quad [6.8]$$

3. Gaussian curves are fitted for the self-similarity curves for both streamwise and wall-normal velocity components.

By using Equations 6.7 and 6.8 together with the Gaussian curve fits, velocity profiles for both components are reconstructed.

6.2.1 Determination of the Model Equations

In this section, the decay parameters used for the model are explained. The equations of the decay parameters (Equation 6.7) are given together with the equations of corresponding coefficients (Equation 6.8). The distribution of the coefficients is compared with the distribution of the coefficients for MR3 and MR4 [77]. It should be noted that only the subsonic results are employed to construct the model, namely, the experimental results of MVG2, MVG3, and MVG4 and the numerical simulation results of MVG5 and MVG6.

6.2.1.1 Equations for the Streamwise Velocity Component

6.2.1.1.1 Decay of the Maximum Velocity Deficit

In order to model the streamwise velocity profiles, curves are fitted for the decay of the difference between the maximum velocity deficit and the undisturbed boundary layer ($U_{Def}=|U_{BL}-U|_{max}$) for the experimental results of MVG2, MVG3, and MVG4 and for the numerical simulation results of MVG5 and MVG6. The decay of U_{Def} is given in Figure 6.4 for both experimental and numerical simulation results for all the MVGs considered. It is observed that MVG5, MVG6, MR3, and MR4 [77], having the highest h/δ ratios, do not follow the general trend followed by others; this is the main reason for adding the numerical results of MVG5 and MVG6 to the model equations, and the difference between the behaviors of larger MVGs is most probably because of the fact that the streamwise vortex pair exceeds the boundary layer thickness encountering the higher-energy freestream flow after a certain streamwise distance (Figure 5.16).

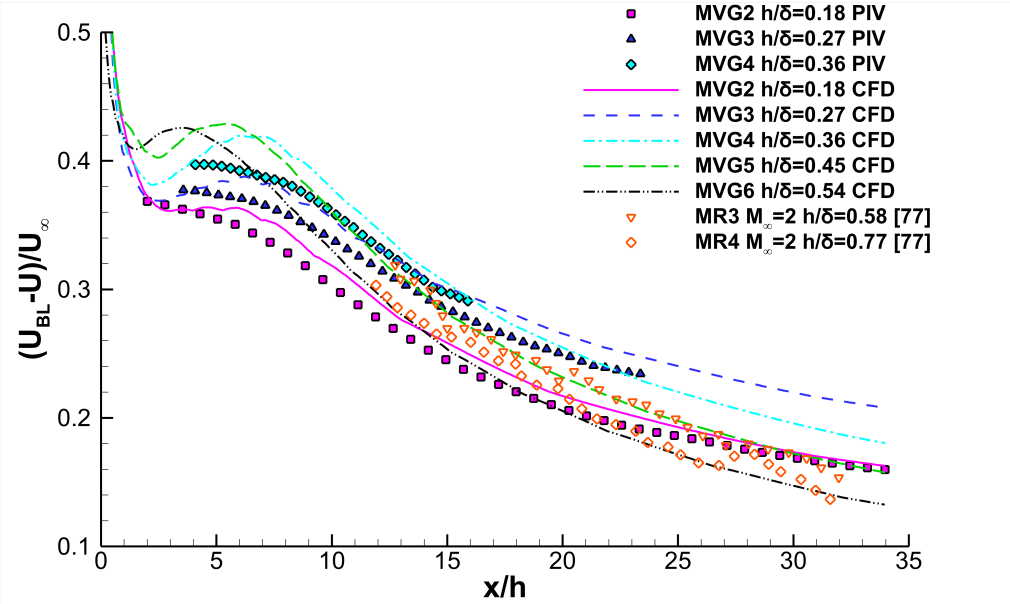

Figure 6.4 The decay of the difference between the maximum velocity deficit and the undisturbed boundary layer.

The curve-fitting equation used for the MVGs is given in Equation 6.9, where the power is -0.45, and the coefficient is named A.

$$U_{Def} = A\left(\frac{x}{h}\right)^{-0.45} \qquad [6.9]$$

The distribution of A with respect to h/δ is given in Figure 6.5, and its values are tabulated in Table 6.1. The distribution of A shows two different trends, with MVG4 being at the peak. One trend is rising with increasing h/δ for MVG2 and MVG3, and the other is falling with increasing h/δ for MVG5 and MVG6, showing that there might be an h/δ limit regarding the definition of a Micro Vortex Generator. This effect can also be explained by the fact that the streamwise vortex pair generated by the larger MVGs exceeds the boundary layer thickness (Figure 5.11).

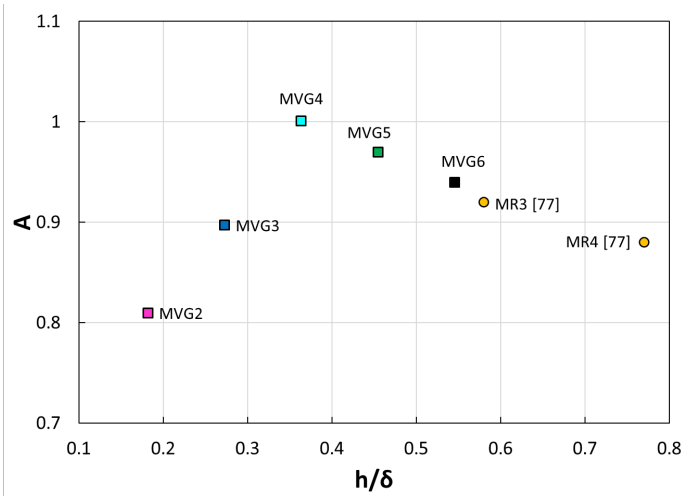

Figure 6.5 The distribution of the coefficient A.

Table 6.1 The coefficient values used for modeling the streamwise velocity component.

MVG	h/δ	A
MVG2	0.18	0.85
MVG3	0.27	0.95
MVG4	0.36	0.99
MVG5	0.45	0.97
MVG6	0.54	0.94
MR3 *[77]*	0.58	0.92
MR4 *[77]*	0.77	0.88

Due to having two different trends, two curves are fitted for the distribution of A with respect to h/δ seen in Figure 6.5 (Equations 6.10 and 6.11). Equation 6.10 (A_{rising}) is employed for the cases with h/δ less than 0.36, and Equation 6.11 ($A_{falling}$) is employed for the cases with h/δ greater than 0.36. Both equations can be used for MVG4 (h/ δ=0.36), as both result in approximately the same coefficient value. For MR3 and MR4, the curve-fitting equation predicts the coefficient with less than 1% error.

$$A_{rising} = 0.814\left(\frac{h}{\delta}\right) + 0.7063 \quad [6.10]$$

$$A_{falling} = -0.287\left(\frac{h}{\delta}\right) + 1.103 \quad [6.11]$$

6.2.1.1.2 Decay of the Position of the Maximum Velocity Deficit

In order to model the streamwise velocity component, the position of the maximum velocity deficit is also needed. Therefore, curves are fitted for the experimental results of MVG2, MVG3, and MVG4 and for the numerical simulation results for MVG5 and MVG6. The decay of the position of the maximum velocity for all the experimental and numerical simulation results, along with the curves of MR3 and MR4 [77], are given in Figure 6.6. Compared to the decay of the maximum velocity deficit (Figure 6.4), the curves for the decay of its position seem to be more scattered, and the agreement between the numerical simulation results and the experimental results is poorer. However, for the range of x/h=10 and 20, for which the curves are fit, both the behavior of the MVGs and the agreement between the experimental measurements and numerical simulation results are better compared to the other x/h stations.

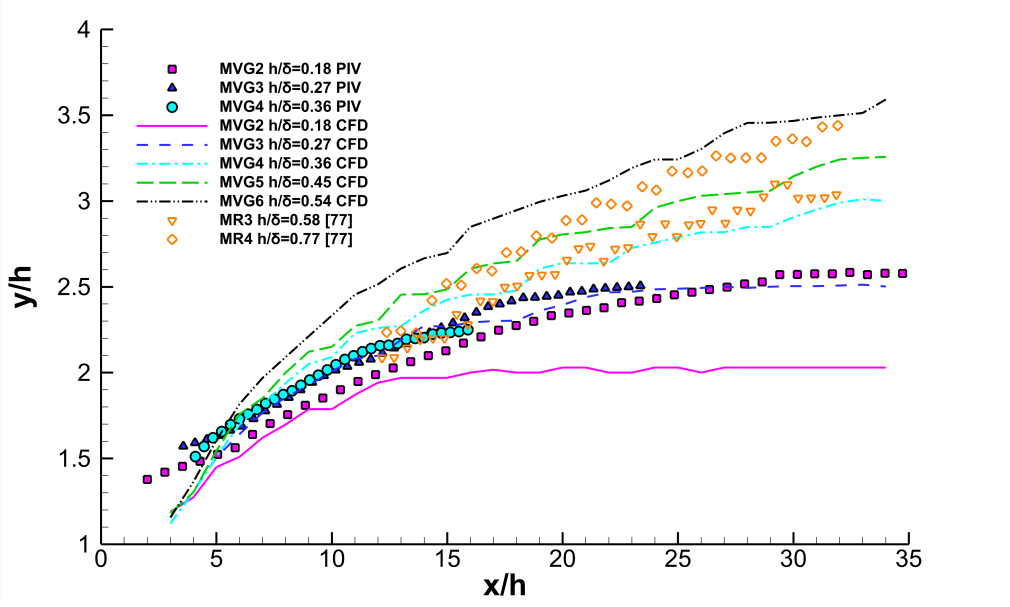

Figure 6.6 The decay of the position of maximum velocity deficit.

The curve-fitting equation for the decay of the maximum velocity deficit is given by Equation 6.12, where the coefficient is named B and the power is 0.27.

$$y_{Udef} = B\left(\frac{x}{h}\right)^{0.27} \quad [6.12]$$

The distribution of B with respect to h/δ is given in Figure 6.7, and the values of B are tabulated in Table 6.2. The values for the experimental and numerical simulation results follow an approximately linear curve. However, the results for MR3 and MR4 follow an entirely different curve. The curve fit equation is given by Equation 6.13. It should be noted that the curve-fitting excludes MR3 and MR4. The coefficient values for MVG2 to MVG6, when calculated using Equation 6.13, are within an error band of ±2%. However, for MR3 and MR4, as expected, the error is up to 25%. Therefore, a high discrepancy is expected regarding the position of the maximum velocity deficit when reconstructing their streamwise velocity profiles using the model.

$$B = 0.5838\left(\frac{h}{\delta}\right) + 0.9087 \quad [6.13]$$

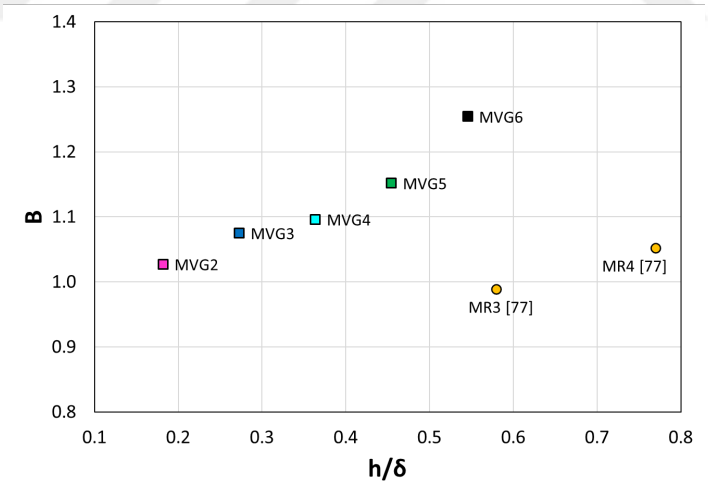

Figure 6.7 The distribution of the coefficient B.

Table 6.2 The values of A for the MVGs used to construct the model and for MVGs from [77].

MVG	h/δ	A
MVG2	0.18	1.03
MVG3	0.27	1.07
MVG4	0.36	1.09
MVG5	0.45	1.15
MVG6	0.54	1.25
MR3 *[77]*	0.58	0.98
MR4 *[77]*	0.77	1.05

6.2.1.2 Reconstruction of Streamwise Velocity Profiles of Supersonic MVG Wakes

The streamwise velocity profiles from Sun [77] and Giepman [74], which are acquired at supersonic freestream velocities for ramp-type MVGs, are reconstructed using the Ramp-Type MVG Wake Model. Information on the flow conditions and the MVGs is given in Table 5.1. Figure 6.8 gives the reconstructed streamwise velocity profiles at three streamwise stations for MR3 and MR4, having h/δ ratios of 0.58 and 0.77, respectively. At x/h=12, the model predicts the maximum velocity deficit with an error of 9% and 5% for MR3 and MR4, respectively. In comparison, the error percentages of the model predictions for the position of the maximum velocity deficit for MR3 and MR4 are 17% and 25%, respectively. As the wake progresses further, the error for the maximum velocity deficit stays approximately the same for MR3; however, for MR4, which has a much higher h/δ value compared to the MVGs used to construct the model, the error increases up to 20% at x/h=32. In the case of the position of the maximum velocity deficit, the error percentages for both MR3 and MR4 decrease to approximately 5% as the velocity profiles flatten as the wake progresses downstream. The decrease can be explained by the distribution of the decay of the position of maximum velocity deficit seen in Figure 6.6, as the curves of MR3 and MR4 start to collapse and exhibit similar trends with MVG5 and MVG6 further downstream after approximately x/h=17.

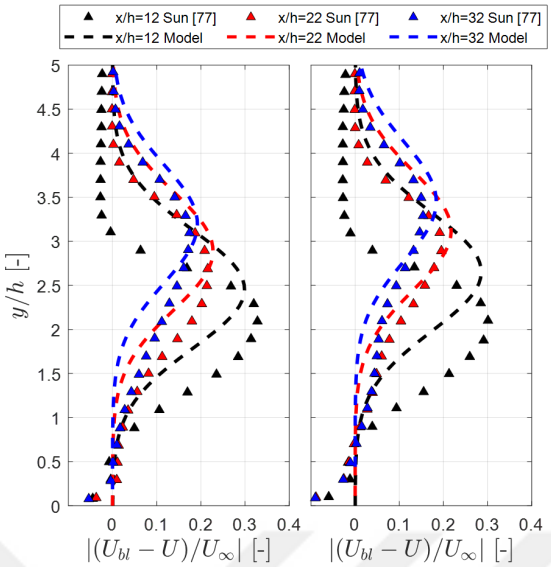

Figure 6.8 Reconstruction of the streamwise velocity profiles for left: MR3 (h/δ=0.58) and right: MR4 (h/δ=0.77) from [77].

The reconstruction of the streamwise velocity profiles for G8 [74], which has an h/δ ratio of 0.46, is given in Figure 6.9. A better general distribution is achieved for this case compared to the cases of MR3 and MR4, especially in the region between the wall and the position of the maximum velocity deficit. At x/h=10, the model predicts the maximum velocity deficit with an error of 7%, whereas its position is predicted with an error of 9%. Similar to the case of MR3 and MR4, the error in the predictions regarding the maximum velocity deficit increases and that regarding its position decreases as the wake progresses downstream, as they are approximately 24% and 6% at x/h=20, respectively.

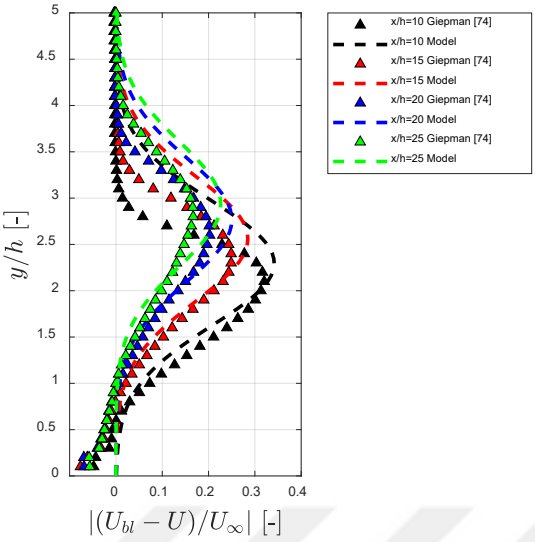

Figure 6.9 Reconstruction of the streamwise velocity profiles for G8 (h/δ=0.46) from [74].

6.2.1.3 Equations for the Wall-Normal Velocity Component

6.2.1.3.1 Decay of the Maximum Upwash Velocity

The value of the maximum upwash velocity (V_{max}) is needed in order to model the wall-normal velocity profiles of MVGs. To that end, curves are fitted for the decay of the maximum upwash velocity for MVG2, MVG3, and MVG4 using the experimental results and for MVG5 and MVG6 using the numerical simulation results. The numerical and experimental results are shown in Figure 6.10, along with the results for MR3 and MR4. A satisfactory agreement between the experimental and numerical simulation results is achieved, and the general trends of MR3 and MR4 exhibit similarity to their subsonic counterparts. However, it should be noted that the maximum upwash velocity values for MR3 and especially MR4 are higher than their subsonic counterparts, particularly at the region of x/h=12 to 17, indicating a more significant upwash motion.

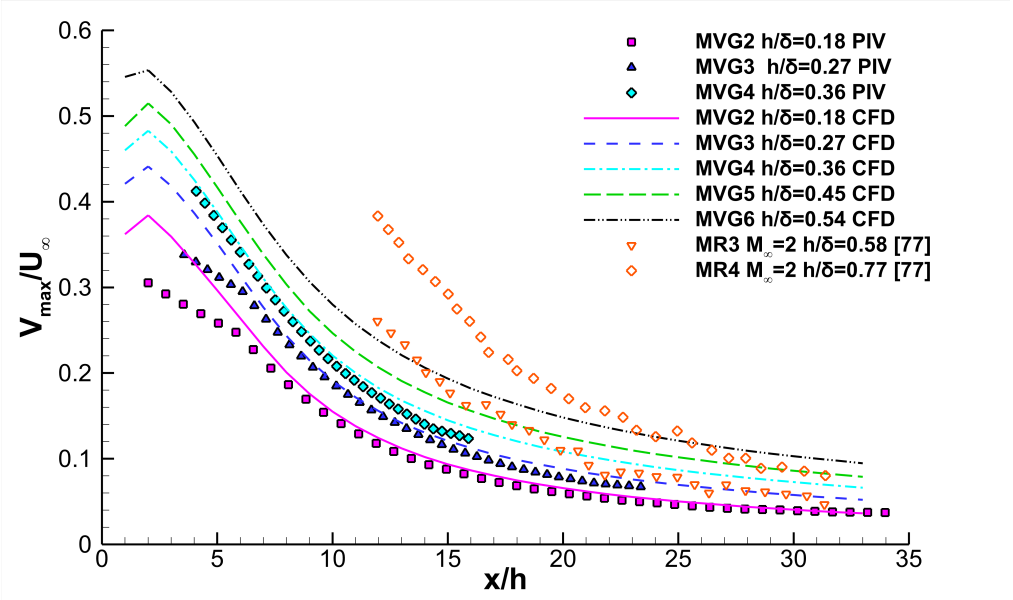

Figure 6.10 The decay of the maximum upwash velocity.

The wake width (w_V) exhibits the same linear distribution for all the MVGs concerned, and Equation 6.14 gives the wake width distribution.

$$w_V = 0.13\left(\frac{x}{h}\right) + 0.9 \qquad [6.14]$$

The curve-fitting equation for the maximum upwash velocity is given by Equation 6.15, where the coefficient is named C, and the power is -1.3.

$$V_{max} = C\left(\frac{x}{h}\right)^{-1.3} \qquad [6.15]$$

Figure 6.11 gives the distribution of the coefficient C with respect to h/δ, and values of C are tabulated in Table 6.3, with the actual values for MR3 and MR4. A curve is fitted through the values for MVG2 to MVG6. The distribution of coefficient C is linear, unlike the distribution of coefficient A (Figure 6.5), which is defined by two different curves. This behavior is probably because the wall-normal velocity component is less affected by the freestream flow when the vortices exceed the boundary layer in contrast to the streamwise velocity component (Figure 5.16). The resulting curve equation is given in Equation 6.16, and the C value for MR3 is predicted with a 5% error, whereas that for MR4 is predicted with an approximately 20% error.

$$C = 7.9513\left(\frac{h}{\delta}\right) + 1.2435 \quad [6.16]$$

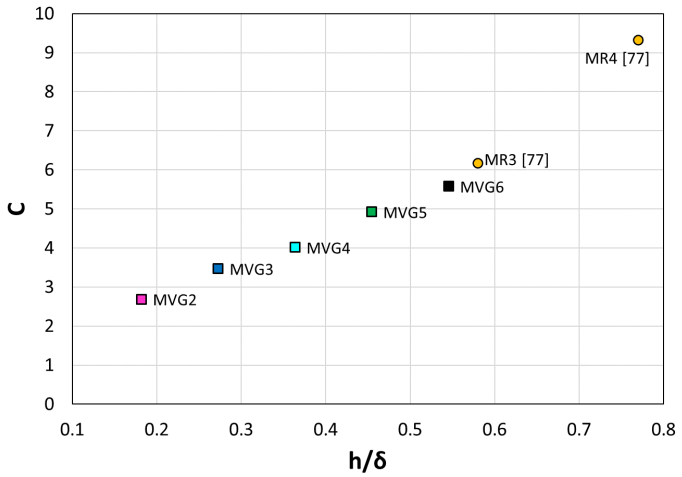

Figure 6.11 The distribution of the coefficient C.

Table 6.3 The values of C for the MVGs used to construct the model and for MVGs from [77].

MVG	h/δ	C
MVG2	0.18	2.69
MVG3	0.27	3.47
MVG4	0.36	4.01
MVG5	0.45	4.92
MVG6	0.54	5.58
MR3 *[77]*	0.58	6.17
MR4 *[77]*	0.77	9.32

6.2.1.3.2 Decay of the Position of the Maximum Upwash Velocity

In order to reconstruct the wall-normal velocity profiles, the position of the maximum upwash velocity with respect to x/h should be known. To that end, curves are fit for the results in a similar manner to the other decay parameters. The decay of the position of the maximum upwash velocity is given in Figure 6.12. A similar general trend is observed for all the MVGs considered. However, it was also observed that the numerical simulations overpredicted the position of the maximum upwash velocity.

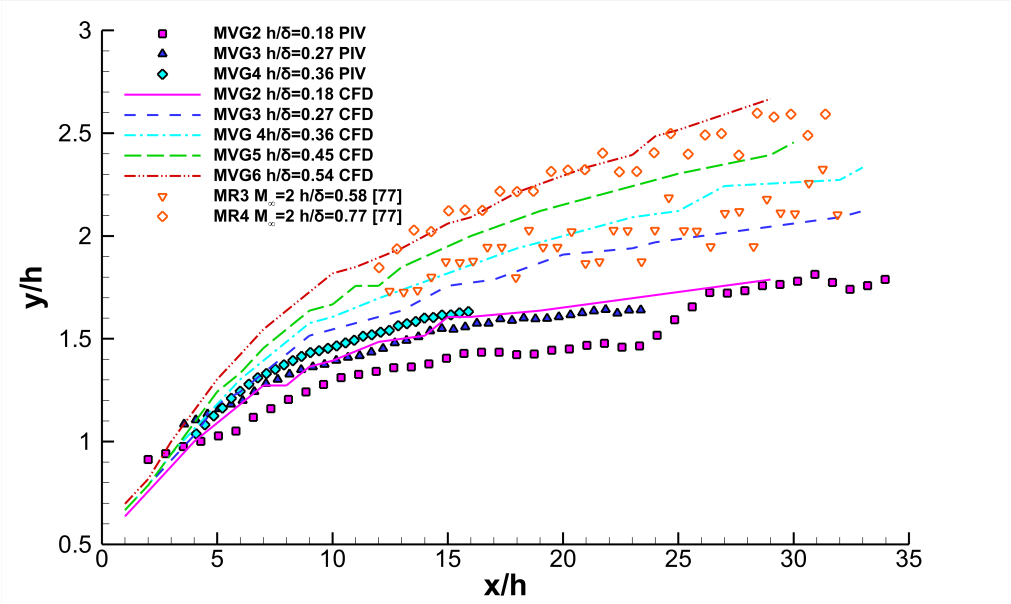

Figure 6.12 The decay of position of the maximum upwash velocity.

The curve-fit equation for the position of the maximum upwash velocity is given by Equation 6.17, where the coefficient is named D, and the power is 0.23.

$$y_{Vmax} = D\left(\frac{x}{h}\right)^{0.23} \quad [6.17]$$

Figure 6.13 gives the distribution of the coefficient D, and the values are tabulated in Table 6.4. The curve fit equation for D is given by Equation 6.18. The values for MR3 and MR4 exhibit a linear behavior; however, they do not follow the trend of the other MVGs. The predictions using Equation 6.18 resulted in errors of approximately 10% for both MR3 and MR4.

$$D = 0.836\left(\frac{h}{\delta}\right) + 0.6 \quad [6.18]$$

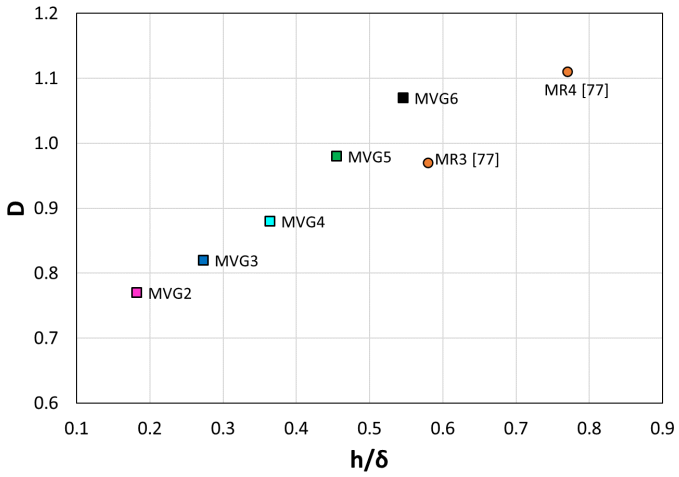

Figure 6.13 The distribution of the coefficient D.

Table 6.4 The values of D for the MVGs used to construct the model and for MVGs from [77].

MVG	h/δ	D
MVG2	0.18	0.77
MVG3	0.27	0.82
MVG4	0.36	0.88
MVG5	0.45	0.98
MVG6	0.54	1.07
MR3 *[77]*	0.58	0.97
MR4 *[77]*	0.77	1.11

6.2.1.4 Reconstruction of Wall-Normal Velocity Profiles of Supersonic MVG Wakes

The wall-normal velocity profiles from Sun [77] and Giepman [74], which are acquired at supersonic freestream velocities for ramp-type MVGs, are reconstructed using the Ramp-Type MVG Wake Model. Information on the flow conditions and the MVGs is given in Table 5.1. The reconstructions of the wall-normal velocity profiles at various streamwise stations for MR3 and MR4 are given in Figure 6.14. A satisfactory agreement is achieved between the model and the experimental results regarding the general trends of the wall-normal velocity profiles. At x/h=12 for MR3, the value of maximum upwash velocity is predicted by the model with an error of 3%, whereas for MR4, the error is more than 15%, as expected since MR4 creates a

more significant upwash velocity in that region (Figure 6.10). The prediction errors in terms of the maximum upwash velocity further downstream increase to the levels of 10% for MR3 and decrease to approximately 7% at x/h=22 for MR4. Better accuracy in terms of the position of the maximum upwash velocity is achieved for both MR3 and MR4. The maximum error regarding the position of the maximum upwash velocity is as low as 1% for MR3 and 4% for MR4.

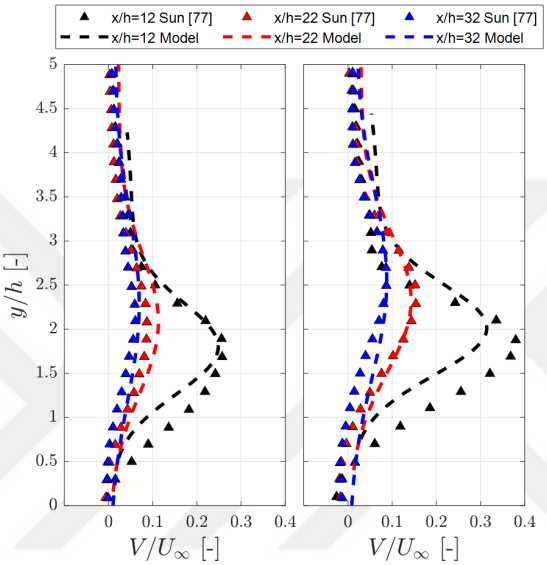

Figure 6.14 Reconstruction of the wall-normal velocity profiles for left: MR3 (h/δ=0.58) and right: MR4 (h/δ=0.77) from [77].

Figure 6.15 gives the reconstruction of the wall-normal velocity profiles for G8 having an h/δ ratio of 0.46. Similarly to the reconstruction of the profiles of MR3 and MR4, the general trends of the wall-normal profiles are predicted well with the model. Moreover, the maximum upwash velocity and its positions are predicted with satisfactory accuracy for most of the streamwise positions. The error percentages regarding the value of the maximum upwash velocity and its position are at the level of 5%. At x/h=25, however, the error regarding the maximum upwash velocity is increased even though the general trend of the profile is captured well.

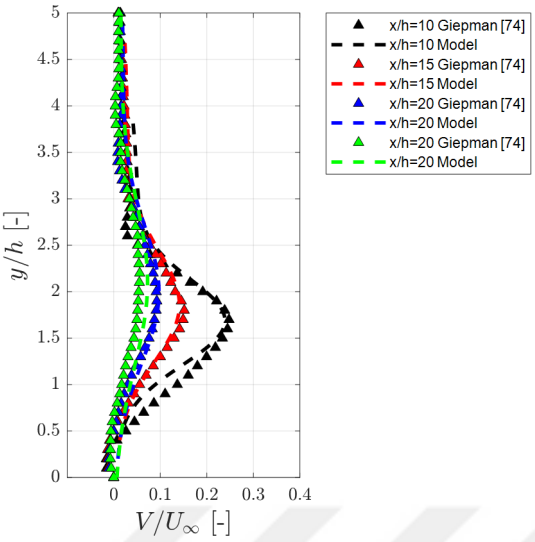

Figure 6.15 Reconstruction of the wall-normal velocity profiles for G8 (h/δ=0.46) from [74].

CHAPTER 7

CONCLUSION

This study investigates the wake characteristics of Micro Vortex Generators (MVGs) in a subsonic flow regime. First, the wakes generated by three ramp-type MVGs with different h/δ ratios are characterized experimentally using a two-dimensional two-component particle image velocimetry technique. The experimental results are complemented with three-dimensional numerical simulations for five different h/δ ratios ranging from 0.18 to 0.54. The effect of the device height, or the h/δ ratio, is investigated in terms of velocity components, vorticity distributions, turbulence properties, and various decay parameters, such as maximum streamwise velocity deficit and maximum upwash velocity, using five different device heights employing the experimental and numerical results. The self-similarity of the ramp-type MVG wake in terms of streamwise and wall-normal velocity components is investigated. The wake flow properties are then compared to similar types of MVGs operating in the supersonic regime available from the literature. The experimental and numerical results reveal general operating principles and wake decay characteristics in the low subsonic flow regime, which display similar characteristics to MVGs of similar h/δ values operating at supersonic conditions. It is shown that the vortex strength, and thus mixing and wake decay characteristics, depend on the effective device Reynolds number regardless of the Mach number. A wake model is suggested using the self-similarity of the ramp-type MVGs and the wake decay parameters. Using the detailed investigation of the decay parameters for the modeling efforts, a method to designate the limit between MVGs and conventional (δ-scale) vortex generators is suggested based on the wake deficit decay characteristics. The model is then used to reconstruct wakes of ramp-type MVGs in supersonic flow regimes from the literature.

Below is the list of the main conclusions of this study:

- In accordance with the studies in the literature, the results showed that as the wake progresses downstream, the counter-rotating vortex pair lifts off from the wall and decays further downstream. The results also show that with increasing MVG height, the strength and the lift-off of the vortex pair increase.
- The effect of the device height is clearly seen from the turbulence properties, especially from the wall-normal velocity fluctuations. The effect of the secondary vortices, which are much smaller in size compared to the primary vortex pair, is seen in the contours and profiles of velocity fluctuations in the near wake (x/h=2). A concentration of peaks on the upper part of the wake, indicating the shear layer, is seen in both streamwise and wall-normal velocity fluctuations. Moreover, the increase seen in the fluctuations, i.e., the peaks, is explained by Herges [65] as a consequence of the presence of the streamwise vortex pair. However, as the peaks are concentrated at the shear layer where the vigorous motion of the K-H instability is dominant, it indicates the presence of the K-H instability, which is already shown by Sun [77] in supersonic flow regimes.
- SPOD analysis showed that the K-H instability is present and dominant in subsonic MVG wakes as they are in their supersonic counterparts. The contribution of the K-H instability is found to be increasing with increasing device height, which might be associated with the increased vortex strength generated by the larger devices. The presence of the K-H instability is one more aspect of similarity to the supersonic MVG wakes, and it illustrates that the peaks seen in the velocity fluctuations are most probably due to the vigorous undulations caused by the K-H instability itself.
- The results of the numerical study showed good agreement with the experimental results in terms of streamwise velocity component (U), wall-normal velocity component (V), and out-of-plane vorticity component (Ω_z). The general agreement is sufficient with some levels of disparities to use the numerical simulation results for the investigation of the height effect on the wake and decay parameters.

- Investigation of the height effect on various decay parameters with MVGs having five different h/δ ratios showed that,
    - As the device height increased, the maximum velocity deficit increased, which also increased as the wake progressed downstream. Interestingly, as the h/δ ratio increases, the offset between the curves of the decay of the maximum velocity decreases, indicating that there might be a limit on the h/δ ratio, after which the increase of the maximum velocity deficit slows down.
    - General trends for the subsonic wakes are observed to be similar to their supersonic counterparts, especially for the maximum velocity deficit. For both flow regimes, the curves of the maximum velocity deficit show a collapsing behavior as the h/δ ratio increases. However, this is not valid for the position of the maximum velocity deficit, as the decay curves behave much more dispersed than their behavior regarding the maximum velocity deficit itself.
    - The investigation on the decay of wall-normal velocity showed that as the h/δ ratio increases, the maximum upwash velocity increases, as expected. The maximum upwash velocity decreases as the wake develops downstream, indicating the decay of the wake. The position of the maximum wall-normal velocity also increases with the increasing h/δ ratio, indicating that a stronger vortex pair is generated with larger devices. As the wake progresses downstream, the position of the maximum upwash velocity also increases, indicating the lift-off of the vortex pair.
    - For the subsonic ramp-type MVG wake, the maximum upwash velocity and its position do not show a collapsing behavior in general; however, they seem to collapse with each other and the supersonic data further downstream for the decay of the maximum upwash velocity and at the near-wake region for the decay of its position. The same general trends are recorded for the subsonic and supersonic decay of the maximum upwash velocity and its position.

- The spanwise investigation of the streamwise (U), wall-normal (V), and spanwise (W) velocity components showed that the effects of larger MVGs do not diminish further downstream. This is especially important at the out-of-symmetry planes (i.e., z/h=1), as it is seen that the streamwise and spanwise components are not still totally decayed for MVG6 at x/h=30 and z/h=1 indicating that the there might be excess three-dimensional effects still present in the wake further downstream.
- The drag coefficients of the ramp-type MVGs increase excessively with increasing height. This fact, together with the possibility of having persisting excess three-dimensional effects after the flow control is achieved, shows that, in order to select the optimum device dimensions, care must be given to choosing a device height that is as small as possible to achieve the flow control to avoid the excessive effects caused by the persisting vortices.
- The investigation of the streamwise vorticity component (Ω_x) in streamwise planes (x-planes) illustrates that the vortex pair generated by the MVGs starts to reach and even exceeds the undisturbed boundary layer thickness as the device height increases, indicating the possibility of persisting excess effects of the vortex pair after the desired boundary layer control is achieved.

- The investigation of the decay parameters showed that for the ramp-type MVGs in subsonic flow conditions, as the h/δ ratio increases, the similarity level with their supersonic counterparts also increases. This behavior is explained using the effective Reynolds number and vortex strength values at five device heights downstream. As a result, as the device Reynolds number increased, the vortex strength values of MVGs at five device heights downstream fell into a single line. Therefore, It is concluded that for the values of the device Reynolds number that are higher than or close to a particular value (i.e., 1400), it is possible to create similar wakes regardless of the Mach number.

- A modified method similar to the one used by Sun [77] for self-similarity is suggested, and it is revealed that the ramp-type MVGs in subsonic flow conditions exhibit a self-similar behavior in terms of the velocity components. The self-similarity allows for scaling the MVG wake regardless of the h/δ ratios.
- The wake model suggested for the ramp-type MVG wakes is used to reconstruct the wakes of ramp-type MVGs in supersonic flow conditions. The model achieved the general trends in terms of the streamwise velocity component with a good agreement in the maximum velocity deficit. However, the position of the maximum velocity deficit is modeled with high error percentages. It is seen that the model errors increased with increasing h/δ ratio. The model achieved a better agreement regarding the wall-normal velocity component compared to that achieved in the streamwise velocity component. A better agreement is achieved for the velocity profiles of both velocity components when the results of Giepman [74] are reconstructed, compared to the reconstruction of the results of Sun [77], even though the MVG used by the former has a different design. This is explained by the fact that the h/δ ratios used by Sun [77] are much higher than those used in this study or by Giepman [74].
- Investigating the decay parameters for the modeling effort allowed us to examine the decay behavior of ramp-type MVGs with five different heights and two MVGs with varying heights from [77] in detail. In contrast to the other decay parameters, decay of the maximum velocity deficit (Figure 6.5) showed that there might be a limit of h/δ as the plot of the coefficient values shows an acute difference after h/δ=0.36.

A future research effort is suggested for the investigation of the ramp-type MVG wake employing a tomographic PIV in order to gain insight into the three-dimensional organization of the wake. Moreover, performing an experimental campaign with a higher sampling rate is suggested to have a more in-depth discussion on the instabilities. The instantaneous organization of the flow and the

vortices in streamwise (x-direction, wall-normal (y-direction), and spanwise (z-direction) planes and their SPOD analysis would produce exciting results, especially on the effects of the unsteady feature, namely the Kelvin-Helmholtz instability on the supposedly steady streamwise vortex pair.

Conducting measurements and numerical simulations employing ramp-type MVGs having various designs is also suggested, which would produce results for improving the wake model further. These results would be used to compare the effects of the chord, the width, and the angle of the ramp-type MVGs on the wake. Furthermore, they would also be used to have a more comprehensive comparison with the wakes of ramp-type MVGs in supersonic flow regimes. Another suggestion regarding the wake model is to compare it with the wake of different types of MVGs, such as vane-type MVGs.

For the supersonic aspect of this study, conducting experiments and numerical simulations at supersonic flow conditions is also suggested. However, it should be noted that access to a supersonic wind tunnel and finding a slot to conduct experiments in a supersonic wind tunnel is expected to be a difficult task, which also obstructs the efforts for a validated numerical simulation case. That is why conducting measurements at subsonic flow regimes with different MVG designs and using the results to compare with the existing results of their supersonic counterparts is suggested. However, to this end, adding more h/δ ratios with the aim of having effective device Reynolds numbers higher than 1400 to investigate the region in subsonic flow regimes where the vortex strength is linear is also suggested.

A deeper investigation of the limit that separates the MVGs from their δ-scale counterparts is needed. The limit suggested in this study solely arises from the change in the behavior of larger MVGs in terms of the maximum velocity deficit. However, this effect might also come from the fact that the streamwise vortices created by larger MVGs exceed the boundary layer thickness further downstream. Consideration must be given to the definition of MVGs. Instead of limiting them by h/δ, a new limit might be defined by the strength or the lift-off behavior of the streamwise vortex pair.

REFERENCES

[1] NASA, "Solar System Exploration," 12 August 2019. [Online]. Available: https://solarsystem.nasa.gov/resources/2486/hubbles-new-portrait-of-jupiter/?category=planets_jupiter. [Accessed 26 February 2023].

[2] Journey to the Microcosmos, "Stentors: Single-Celled Giants," Journey to the Microcosmos, 8 July 2019. [Online]. Available: https://youtu.be/PZoaKzEXzi8. [Accessed 26 February 2023].

[3] M. Gad-El-Hak, Flow Control: Passive, Active, and Reactive Flow Management, Cambridge University Press, 2000.

[4] M. S. Genç, Ü. Kaynak and H. Yapici, "Performance of transition model for predicting low Re aerofoil flows without/with single and simultaneous blowing and suction," *European Journal of Mechanics - B/Fluids,* vol. 30, pp. 218-235, 2011.

[5] K. Zaman and D. McKinzie, "Control of laminar separation over airfoils by acoustic excitation," in *27th Aerospace Sciences Meeting, 9-12 January 1989*, Reno, NV, 1989.

[6] M. S. Genç, İ. Karasu, H. H. Açıkel, M. T. Akpolat and G. Özkan, "Acoustic Control of Flow Over NACA 2415 Aerofoil at Low Reynolds Numbers," in *Sustainable Aviation: Energy and Environmental Issues*, T. H. Karakoc, M. B. Ozerdem, M. Z. Sogut, C. O. Colpan, O. Altuntas and E. Açıkkalp, Eds., Cham, Springer International Publishing, 2016, p. 375–420.

[7] J. W. Gregory and M. N. Tomac, "A review of fluidic oscillator development and application for flow control," in *43rd Fluid Dynamics Conference, 24-27 June*, San Diego, CA, 2013.

[8] L. J. Souverein and J.-F. Debiève, "Effect of air jet vortex generators on a shock wave boundary layer interaction," *Experiments in Fluids,* vol. 49, pp. 1053-1064, 2010.

[9] J. Wang and L. Feng, Flow Control Techniques and Application, Cambridge University Press, 2018.

[10] D. Hermann, S. Blem and A. Gülhan, "Experimental study of boundary-layer bleed impact on ramjet inlet performance," *Journal of Propulsion and Power,* vol. 27, no. 6, pp. 1186-1195, 2011.

[11] Ö. Harputlu, T. Aksu, M. T. Akpolat, E. Arısoy and C. Çıtak, "Effect of Bleed System On Air Intake Performance," in *10th Ankara International Aerospace Conference, 18-20 September 2019*, Ankara, 2019.

[12] H. D. Taylor, "The Elimination of Diffuser Separation By Vortex Generators," United Aircraft Corporation, Report No. R-4012-3, June, 1947.

[13] L. J. Lina and W. H. Reed, "A Preliminary Flight Investigation of the Effects of Vortex Generators On Seperation Due to Shock," National Advisory Committee for Aeronautics, Research Memorandum, RM L50J02, Langley Air Force Base, VA, 1950.

[14] G. B. McCullough, G. E. Nitzberg and J. A. Kelly, "Preliminary investigation of the delay of turbulent flow seperation by means of wedge-shaped bodies," National Advisory Committee for Aeronautics, Research Memorandum, RM A50L12, Moffet Field, CA, 1951.

[15] C. C. Wood, "Preliminary Investigation of the Effects of Rectangular Vortex Generators On the Performance of A Short 1.9:1 Straight-Wall Annular Diffuser," National Advisory Committee for Aeronautics, Research Memorandum, RM L51G09, Langley Field, VA, 1951.

[16] J. A. Weiberg and G. B. McCullough, "Wind-Tunnel Investigation At Low Speed of A Twisted and Cambered Wing Swept Back 63° With Vortex Generators and Fences," National Advisory Committee for Aeronautics, Research Memorandum, RM A52A17, Moffet Field, CA, 1952.

[17] E. F. Valentine and R. B. Carroll, "Effects of Some Primary Variables of Rectangular Vortex Generators On the Static-Pressure Rise Through A Short Diffuser," National Advisory Committee for Aeronautics, Research Memorandum, RM L52B13, Langley Field, VA, 1952.

[18] G. Hieser, "An investigation at transonic speeds of the effects of fences, drooped nose, and vortex generators on the aerodynamic characteristics of a wing-fuselage combination having a 6-percent-thick, 45° sweptback wing," National Advisory Committee for Aeronautics, Research Memorandum, Langley Field, VA, 1953.

[19] N. M. McFadden, G. A. Rathert and R. S. Bray, "The Effectiveness of Wing Vortex Generators in Improving the Maneuvering Characteristics of A Swept-Wing Airplane at Transonic Speeds," National Advisory Committee for Aeronautics, Technical Note 3523, Moffet Field, CA, 1955.

[20] G. J. Morris and L. J. Lina, "A Limited Flight Investigation of the Effect of Three Vortex-Generator Configurations On the Effectiveness of A Plain Flap On An Unswept Wing," National Advisory Committee for Aeronautics, Technical Note 3536, Langley Field, VA, 1955.

[21] G. B. Schubauer and W. G. Spangenberg, "Forced mixing in boundary layers," *Journal of Fluid Mechanics,* vol. 8, no. 1, pp. 10-32, 1960.

[22] W. Calarese, W. P. Crisler and G. L. Gustafson, "Afterbody drag reduction by vortex generators," in *AIAA 23rd Aerospace Sciences Meeting, January 14-17*, Reno, NV, 1985.

[23] A. A. Afjeh, T. G. Keith and A. Fateh, "Predicted aerodynamic performance of a horizontal-axis wind turbine equipped with vortex generators," *Journal of Wind Engineering and Industrial Aerodynamics,* vol. 33, no. 3, pp. 515-529, 1990.

[24] Z. Zhao, R. Jiang, J. Feng, H. Liu, T. Wang, W. Shen, M. Chen, D. Wang and Y. Liu, "Researches on vortex generators applied to wind turbines: A review," *Ocean Engineering,* vol. 253, 2022.

[25] P. Dvorak, "Windpower Engineering & Development, UpWind solution case study on impact of vortex generators on wind turbine blades," 16 October 2013. [Online]. Available: https://www.windpowerengineering.com/upwind-solution-case-study-impact-vortex-generators-wind-turbine-blades/. [Accessed 20 February 2023].

[26] L. Gao, H. Zhang, Y. Liu and S. Han, "Effects of vortex generators on a blunt trailing-edge airfoil for wind turbines," *Renewable Energy,* vol. 76, pp. 303-311, 2015.

[27] A. M. Kuethe, "Effect of streamwise vortices on wake properties associated with sound generation," *Journal of Aircraft,* vol. 9, no. 10, pp. 715-719, 1972.

[28] Z. Sun, "Micro vortex generators for boundary layer control: principles and applications," *International Journal of Flow Control,* vol. 7, no. (1-2), 2015.

[29] A. E. Holmes, P. K. Hickey, W. R. Murphy and D. A. Hilton, "The application of sub-boundary layer vortex generators to reduce canopy "Mach Rumble" interior noise of the Gulfstream III," in *AIAA 25th Aerospace Sciences Meeting, January 12-15*, Reno, NV, 1987.

[30] R. P. Goss, "Acoustic program for the Grumman Gulfstream II," in *AIAA 3rd Aircraft Design and Operations Meeting, July 12-14*, Seattle, WA, 1971.

[31] B. Dunbar, "NASA Langley Research Center," 22 April 2008. [Online]. Available: https://www.nasa.gov/centers/langley/news/factsheets/Micro-VG.html. [Accessed 15 February 2023].

[32] J. Zaninger, "AIRLINERS.NET," 25 Septemnber 2008. [Online]. Available: https://www.airliners.net/photo/USA-Air-Force/Gulfstream-Aerospace-C-20B-Gulfstream-III-G-1159A/1404340/L. [Accessed 15 February 2023].

[33] D. Rao and T. Kariya, "Boundary-layer submerged vortex generators for separation control - An exploratory study," in *1st National Fluid Dynamics Conference, 25-28 July*, Cincinnati, OH, 1988.

[34] J. C. Lin, F. G. Howard and G. V. Selby, "Small submerged vortex generators for turbulent flow separation control," *Journal of Spacecraft and Rockets,* vol. 27, no. 5, pp. 503-507, 1990.

[35] J. C. Lin, F. G. Howard, D. M. Bushnell and G. V. Selby, "Investigation of several passive and active methods for turbulent flow separation control," in *AIAA 21st Fluid Dynamics, Plasma Dynamics and Lasers Conference, June 18-20*, Seattle, WA, 1990.

[36] J. C. Lin, G. V. Selby and F. G. Howard, "Exploratory study of vortex-generating devices for turbulent flow separation control," in *AIAA 29th Aerospace Sciences Meeting, January 7-10*, Reno, NV, 1991.

[37] M. Kerho, S. Hutcherson, R. F. Blackwelder and R. H. Liebeck, "Vortex generators used to control laminar seperation bubbles," *Journal of Aircraft,* vol. 30, no. 3, pp. 315-319, 1993.

[38] J. C. Lin, "Control of turbulent boundary-layer separation using micro-vortex generators," in *30th AIAA Fluid Dynamics Conference, June 28-July 1*, Norfolk, VA, 1999.

[39] G. Godard and M. Stanislas, "Control of a decelerating boundary layer. Part 1: Optimization of passive vortex generators," *Aerospace Science and Technology,* vol. 10, no. 3, pp. 181-191, 2006.

[40] P. R. Ashill, J. L. Fulker and K. C. Hackett, "A review of recent developments in flow control," *The Aeronautical Journal,* vol. 109, no. 1095, pp. 205-232, 2005.

[41] J. C. Lin, "Review of research on low-profile vortex generators to control boundary-layer separation," *Progress in Aerospace Sciences,* vol. 38, no. 4-5, pp. 389-420, 2002.

[42] P. R. Ashill, J. L. Fulker and K. C. Hackett, "Research at DERA on sub boundary layer vortex generators (SBVGs)," in *39th Aerospace Sciences Meeting and Exhibit, 8-11 January 2001*, Reno, NV, 2001.

[43] P. R. Ashill, J. L. Fulker and K. C. Hackett, "Studies of flows induced by sub boundary layer vortex generators (SVBGs)," in *40th AIAA Aerospace Sciences Meeting & Exhibit, 14-17 January 2002*, Reno, NV, 2002.

[44] C. M. Velte and M. O. L. Hansen, "Investigation of flow behind vortex generators by stereo particle image velocimetry on a thick airfoil near stall," *Wind Energy,* vol. 16, no. 5, pp. 775-785, 2012.

[45] P. Martínez-Filgueira, U. Fernandez-Gamiz, E. Zulueta, I. Errasti and B. Fernandez-Gauna, "Parametric study of low-profile vortex generators," *International Journal of Hydrogen Energy,* vol. 42, no. 28, pp. 17700-17712, 2017.

[46] Y. Yan, E. Avital, J. Williams and J. Cui, "CFD analysis for the performance of micro-vortex generator on aerofoil and vertical axis turbine," *Journal of Renewable and Sustainable Energy,* vol. 11, p. 043302, 2019.

[47] T. C. Tai, "Effect of Midwing Vortex Generators on V-22 Aircraft Forward-Flight Aerodynamics," *Journal of Aircraft,* vol. 40, no. 4, pp. 623-630, 2003.

[48] A. A. T. Syahin, M. Zinnyrah, N. A. Azfar, I. Said, A. C. Idris, M. R. A. Rahman and M. R. Saad, "Effect of micro-ramp vortex generator in improving aerodynamics performance of wing-in-ground craft fuselage," *PERINTIS eJournal,* vol. 11, no. 1, pp. 61-69, 2021.

[49] J. M. Delery, "Shock wave/turbulent boundary layer interaction and its control," *Progress in Aerospace Sciences,* vol. 22, no. 4, pp. 209-280, 1985.

[50] H. Babinsky, Y. Li and C. W. Pitt-Ford, "Microramp control of supersonic oblique shock wave/boundary layer interactions," *AIAA Journal,* vol. 47, no. 3, pp. 668-675, 2009.

[51] D. V. Gaitonde, "Progress in shock wave/boundary layer interactions," *Progress in Aerospace Sciences,* vol. 72, pp. 80-99, 2015.

[52] A. N. Smith, H. Babinsky, J. L. Fulker and P. R. Ashill, "Shock-Wave/Boundary-Layer Interaction Control Using Streamwise Slots in Transonic Flows," *Journal of Aircraft,* vol. 41, no. 3, pp. 540-546, 2004.

[53] H. Ogawa, H. Babinsky, M. Pätzol and T. Lutz, "Shock-wave/boundary-layer interaction control using three-dimensional bumps for transonic wings," *AIAA Journal,* vol. 46, no. 6, pp. 1442-1452, 2008.

[54] S. Roy, J. P. S. Sandhu and S. Ghosh, "Drag reduction in transonic shock-wave/boundary-layer interaction using porous medium: a computational study," *Shock Waves,* vol. 31, pp. 117-132, 2021.

[55] B. Küsters and H. A. Schreiber, "Compressor cascade flow with strong shock-wave/boundary-layer interaction," *AIAA Journal,* vol. 36, no. 11, pp. 2072-2078, 1998.

[56] R. Szwaba, P. Kaczynski and P. Doerffer, "Roughness effect on shock wave boundary layer interaction area in compressor fan blades passage," *Aerospace Science and Technology,* vol. 85, pp. 171-179, 2019.

[57] H. Babinsky and J. K. Harvey, Shock Wave-Boundary-Layer Interactions, Cambridge: Cambridge University Press, 2011.

[58] E. Arısoy, M. T. Akpolat, T. Aksu, C. Çıtak and Ö. Harputlu, "Study on shock wave-boundary layer interaction on a mixed compression air intake," in *10th Ankara International Aerospace Conference, 18-20 September*, Ankara, Türkiye, 2019.

[59] W. Xie, Z. Wu, A. Yu and S. Guo, "Control of severe shock-wave/boundary-layer interactions in hypersonic inlets," *Journal of Propulsion and Power,* vol. 34, no. 3, pp. 614-623, 2018.

[60] W. Huang, H. Wu, Y. Yang, L. Yan and S. Li, "Recent advances in the shock wave/boundary layer interaction and its control in internal and external flows," *Acta Astronautica,* vol. 174, no. 4, pp. 103-122, 2020.

[61] D. C. McCormick, "Shock-boundary layer interaction control with low-profile vortex generators and passive cavity," in *30th Aerospace Sciences Meeting & Exhibit, January 6-9*, Reno, NV, 1992.

[62] J. S. Mounts and T. J. Barber, "Numerical analysis of shock-induced separation alleviation using vortex generators," in *30th Aerospace Sciences Meeting & Exhibit, January 6-9*, Reno, NV, 1992.

[63] S. Lee and E. Loth, "Supersonic boundary layer interactions with various micro-vortex generator geometries," in *39th AIAA Fluid Dynamics Conference, 22-25 June 2009*, San Antonio, TX, 2009.

[64] B. H. Anderson, J. Tinapple and L. Surber, "Optimal control of shock wave turbulent boundary layer interactions using micro-array actuation," in *3rd AIAA Flow Control Conference, 5-8 June*, San Francisco, CA, 2006.

[65] T. Herges, E. Kroeker, G. Elliott and C. Dutton, "Micro-ramp flow control of normal shock/boundary layer interactions," in *47th AIAA Aerospace Sciences Meeting Including The New Horizons Forum and Aerospace Exposition, 5-8 January*, Orlanda, FL, 2009.

[66] H. Babinsky, N. J. Makinson, C. E. Morgan and , "Micro-vortex generator flow control for supersoinc engine inlets," in *45th AIAA Aerospace Sciences Meeting and Exhibit, 8-11 January 2007*, Reno, NV, 2007.

[67] J. M. Oorebeek, W. R. Nolan and H. Babinsky, "Comparison of bleed and micro-vortex generator effects on supersonic boundary-layers," in *50th AIAA Aerospace Sciences Meeting including the New Horizons Forum and Aerospace Exposition, 09-12 January*, Nashville, TN, 2012.

[68] D. Baruzzini, N. Domel and D. N. Miller, "Fundamental challenges of micro-vanes and micro-ramps for high-speed inlet applications: a computational fluid dynamics investigation," in *45th AIAA/ASME/SAE/ASEE Joint Propulsion Conference & Exhibit, 2-5 August*, Denver, CO, 2009.

[69] S. Ghosh, J. Choi and J. R. Edwards, "Numerical simulations of effects of micro vortex generators using immersed-boundary methods," *AIAA Journal,* vol. 48, no. 1, pp. 92-103, 2010.

[70] Z. Sun, F. F. J. Schrijer, F. Scarano and B. W. van Oudheusden, "The three-dimensional flow organization past a micro-ramp in a supersonic boundary layer," *Physics of Fluids,* vol. 24, no. 055105, 2012.

[71] Z. Sun, F. F. J. Schrijer, F. Scarano and B. W. van Oudheusden, "Decay of the supersonic turbulent wakes from micro-ramps," *Physics of Fluids,* Vols. 26, 025115, 2014.

[72] Z. Sun, F. Scarano, B. W. van Oudheusden and F. F. J. Schrijer, "Numerical and experimental investigations of the supersonic microramp wake," *AIAA Journal,* vol. 52, no. 7, pp. 1518-1527, 2014.

[73] Q. Li and C. Liu, "LES for supersonic ramp control flow using MVG at M=2.5 and Reθ=1440," in *48th AIAA Aerospace Sciences Meeting Including the New Horizons Forum and Aerospace Exposition*, Orlando, FL, 2010.

[74] R. H. M. Giepman, "Flow control for oblique shock wave reflections," Ph.D. Dissertation, Delft University of Technology, Delft, Netherlands, 2016.

[75] R. H. M. Giepman, A. Srivastava, F. J. Schrijer, B. W. van Oudheusden and , "Mach and Reynolds Number Effects on the Wake Properties of Microramps," *AIAA Journal,* vol. 54, no. 11, pp. 3481-3494, 2016.

[76] S. Discetti and A. Ianiro, Experimental Aerodynamics, Boca Raton, FL: CRC Press, 2017.

[77] Z. H. Sun, "Micro Ramps in Supersonic Turbulent Boundary Layers: An experimental and numerical study," PhD Thesis, Delft University of Technology, 2014.

[78] B. Anderson, J. Tinapple and L. Surber, "Optimal Control of Shock Wave Turbulent Boundary Layer Interactions Using Micro-Array Actuation," in *3rd AIAA Flow Control Conference, 05-08 June*, San Fransisco, CA, 2006.

[79] J. L. Lumney, "Coherent Structures in Turbulence," in *Transition and Turbulence*, Madison, WI, Academic Press, 1981, pp. 215-242.

[80] L. Sirovich, "TURBULENCE AND THE DYNAMICS OF COHERENT STRUCTURES PART I: COHERENT STRUCTURES," *Quarterly of Applied Mathematics,* vol. 45, no. 3, pp. 561-571, 1987.

[81] Q. Li, Y. Yan, X. Wang and C. Liu, "The Interaction between Vortex Rings and Oblique Shocks by the MVG Controlled Ramp Flow at M=2.5," in *49th AIAA Aerospace Sciences Meeting including the New Horizons Forum and Aerospace Exposition 4 - 7 January 2011*, Orlando, Florida, 2011.

[82] X. Dong, S. Charkrit, X. Truong and C. Liu, "POD Study on vortex Structures in MVG wake," in *AIAA Scitech 2019 Forum*, San Diego, CA, 2019.

[83] Dong, X., X. Cai, Y. Dong and C. Liu, "POD analysis on vortical structures in MVG wake by Liutex core line identification," *Journal of Hydrodynamics,* vol. 32, pp. 497-509, 2020.

[84] Y. Wang, Y. Gao, J. Liu and C. Liu, "Explicit formula for the Liutex vector and physical meaning of vorticity based on the Liutex-Shear decomposition," *Journal of Hydrodynamics,* vol. 31, pp. 464-474, 2019.

[85] S. Charkrit and C. Liu, "Vortex core and POD analysis on hairpin vortex formation in flow transition," *arXiv preprint, arXiv:1912.01975,* 2019.

[86] F. R. Menter, "Two-equation eddy-viscosity turbulence models for engineering applications," *AIAA Journal,* vol. 32, no. 8, pp. 1598-1605, 1994.

[87] F. R. Menter, "Zonal Two Equation k-w Turbulence Models For Aerodynamic Flows," in *23rd Fluid Dynamics, Plasmadynamics, and Lasers Conference*, Orlando, FL, 1993.

[88] Y. Levy, D. Degani and A. Seginer, "Graphical Visualization of Vortical Flows by Means of Helicity," *AIAA Journal,* vol. 28, no. 8, pp. 1347-1352, 1990.

APPENDICES

A. Spanwise Investigation of Velocity Profiles

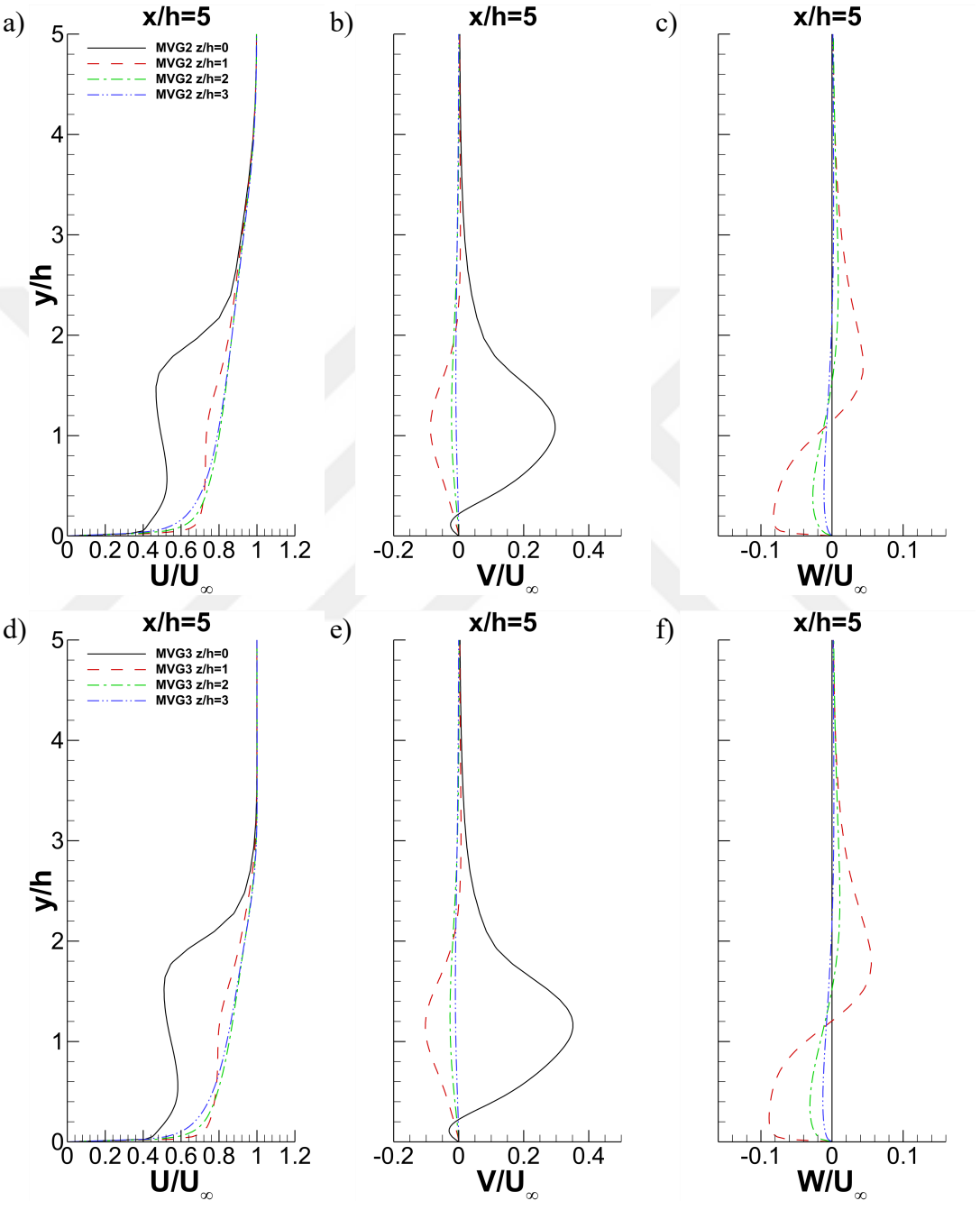

Figure A.8.1 Comparison of the velocity components, first column: U, second column: V, and third column: W, at x/h=5 and z/h=0 to 3 for MVG2 (top row) and MVG3 (bottom row).

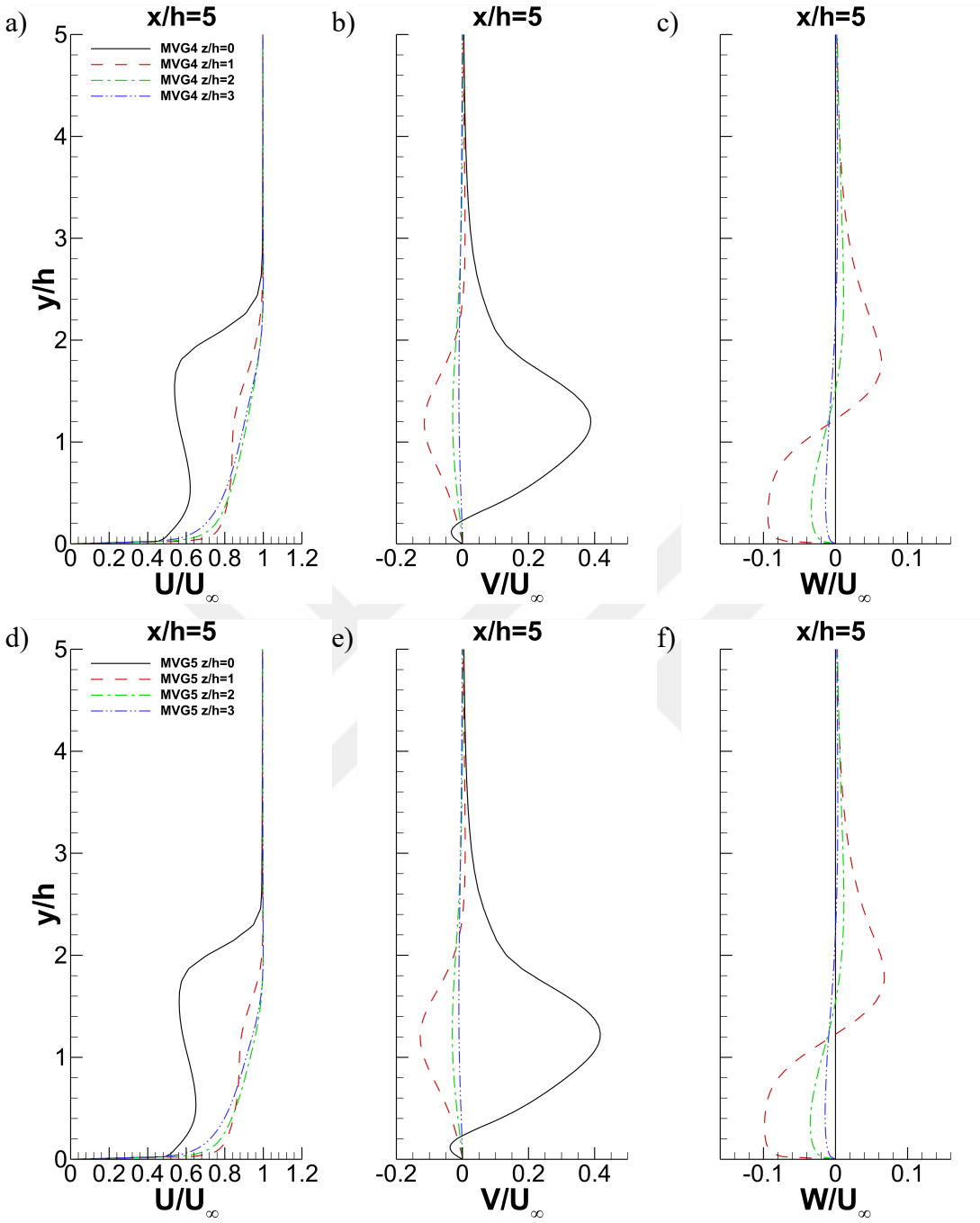

Figure A.8.2 Comparison of the velocity components, first column: U, second column: V, and third column: W, at x/h=5 and z/h=0 to 3 for MVG4 (top row) and MVG5 (bottom row).

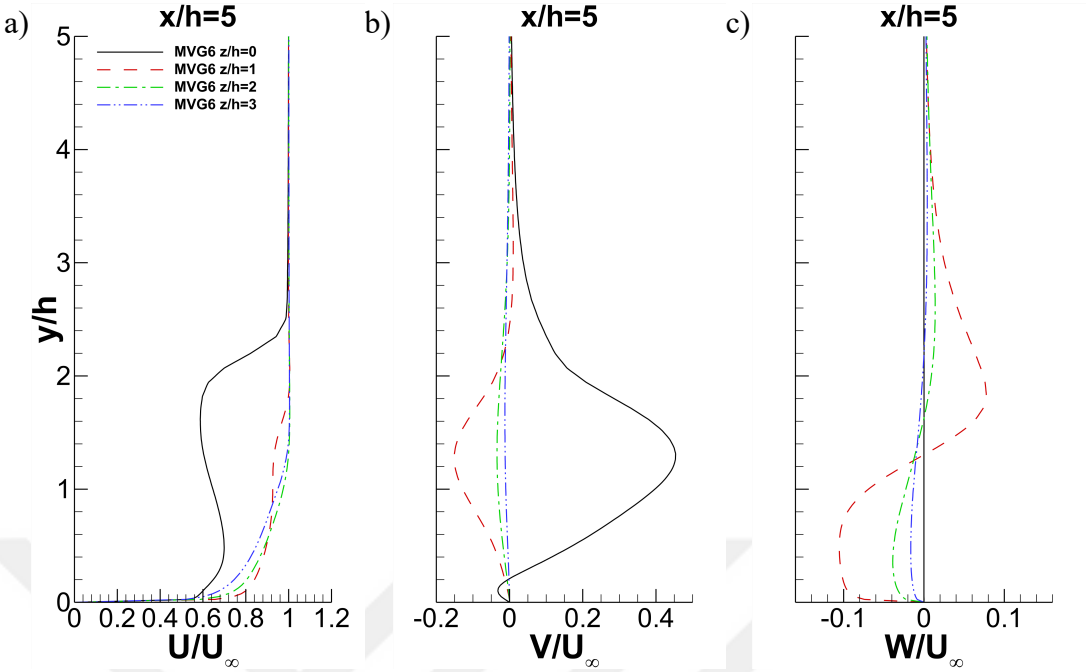

Figure A.8.3 Comparison of the velocity components, first column: U, second column: V, and third column: W, at x/h=5 and z/h=0 to 3 for MVG6.

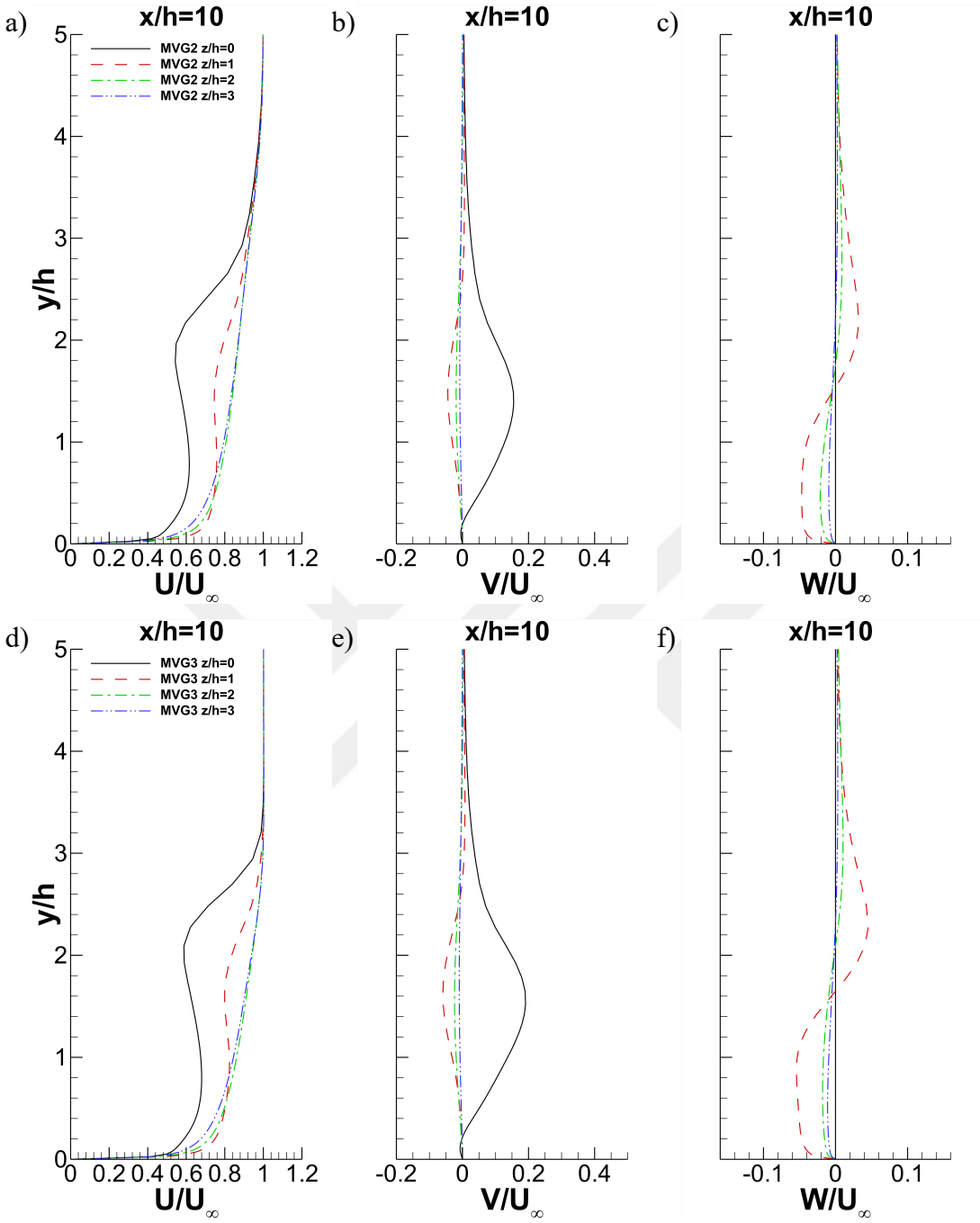

Figure A.8.4 Comparison of the velocity components, first column: U, second column: V, and third column: W, at x/h=10 and z/h=0 to 3 for MVG2 (top row) and MVG3 (bottom row).

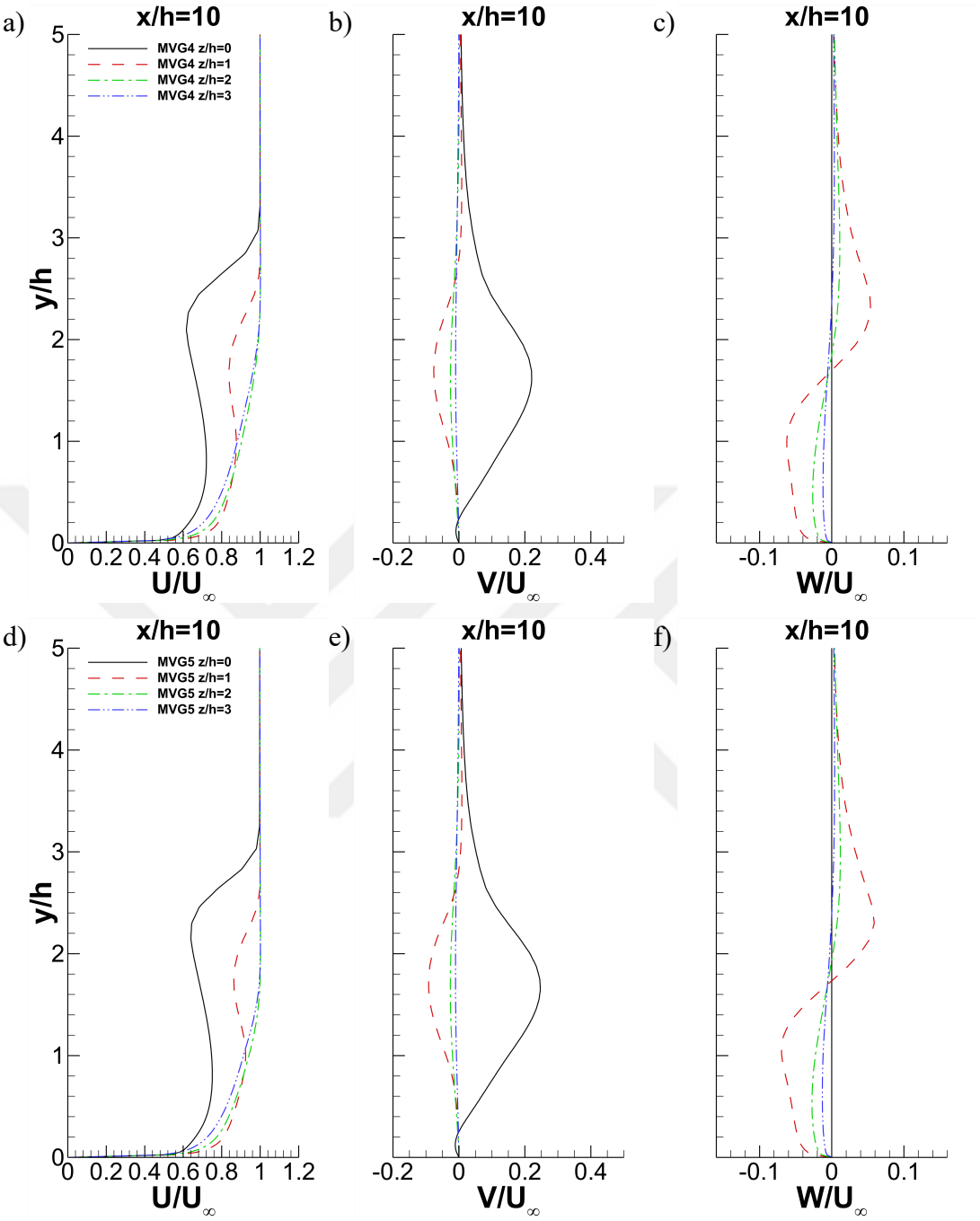

Figure A.8.5 Comparison of the velocity components, first column: U, second column: V, and third column: W, at x/h=10 and z/h=0 to 3 for MVG4 (top row) and MVG5 (bottom row).

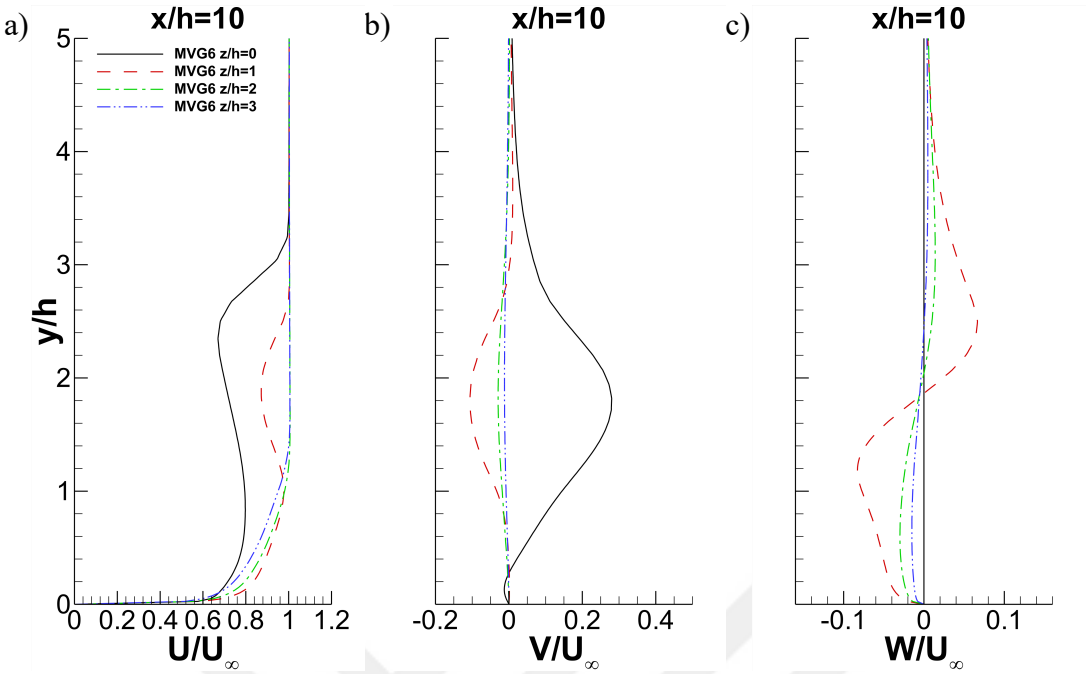

Figure A.8.6 Comparison of the velocity components, first column: U, second column: V, and third column: W, at x/h=10 and z/h=0 to 3 for MVG6.

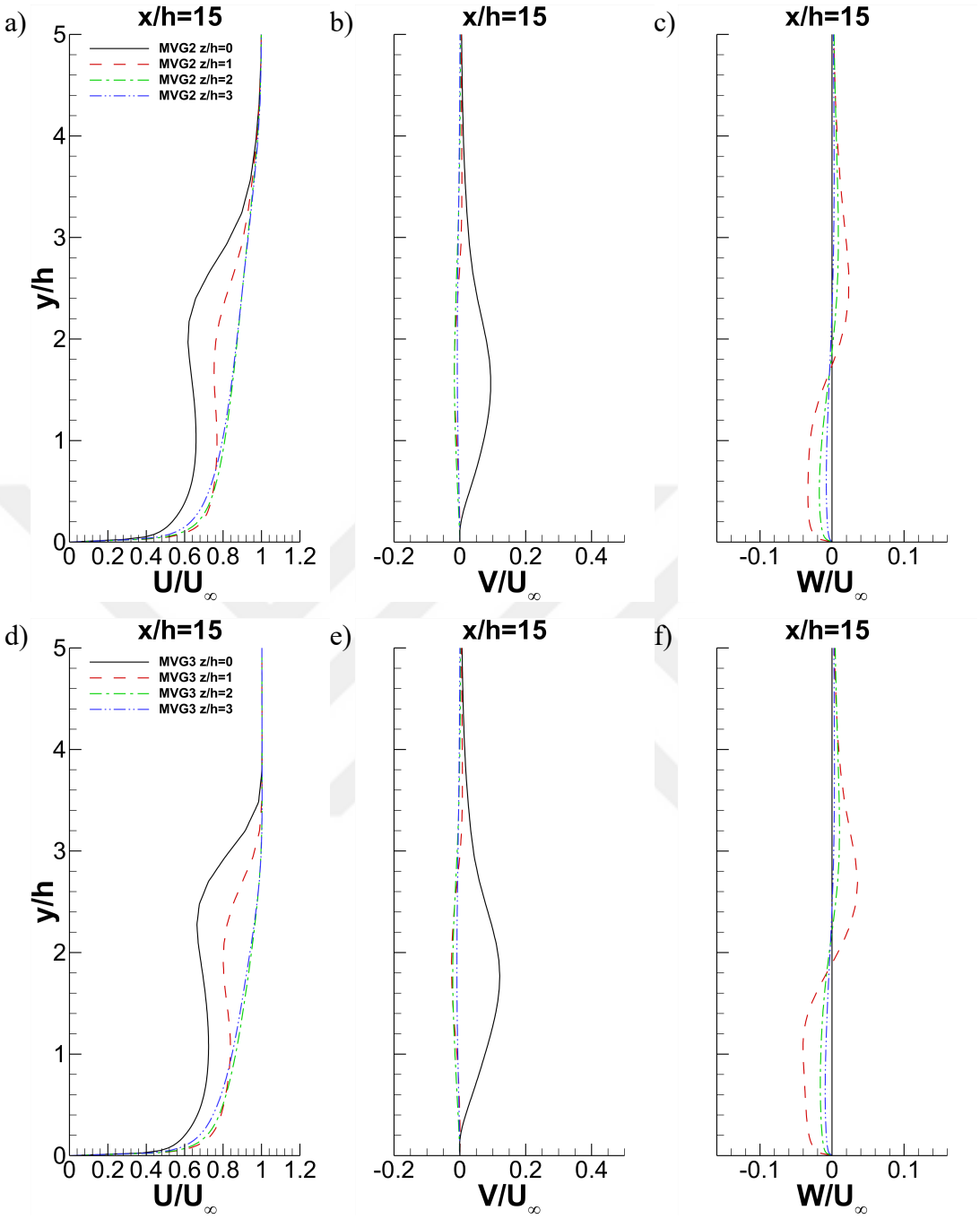

Figure A.8.7 Comparison of the velocity components, first column: U, second column: V, and third column: W, at x/h=15 and z/h=0 to 3 for MVG2 (top row) and MVG3 (bottom row).

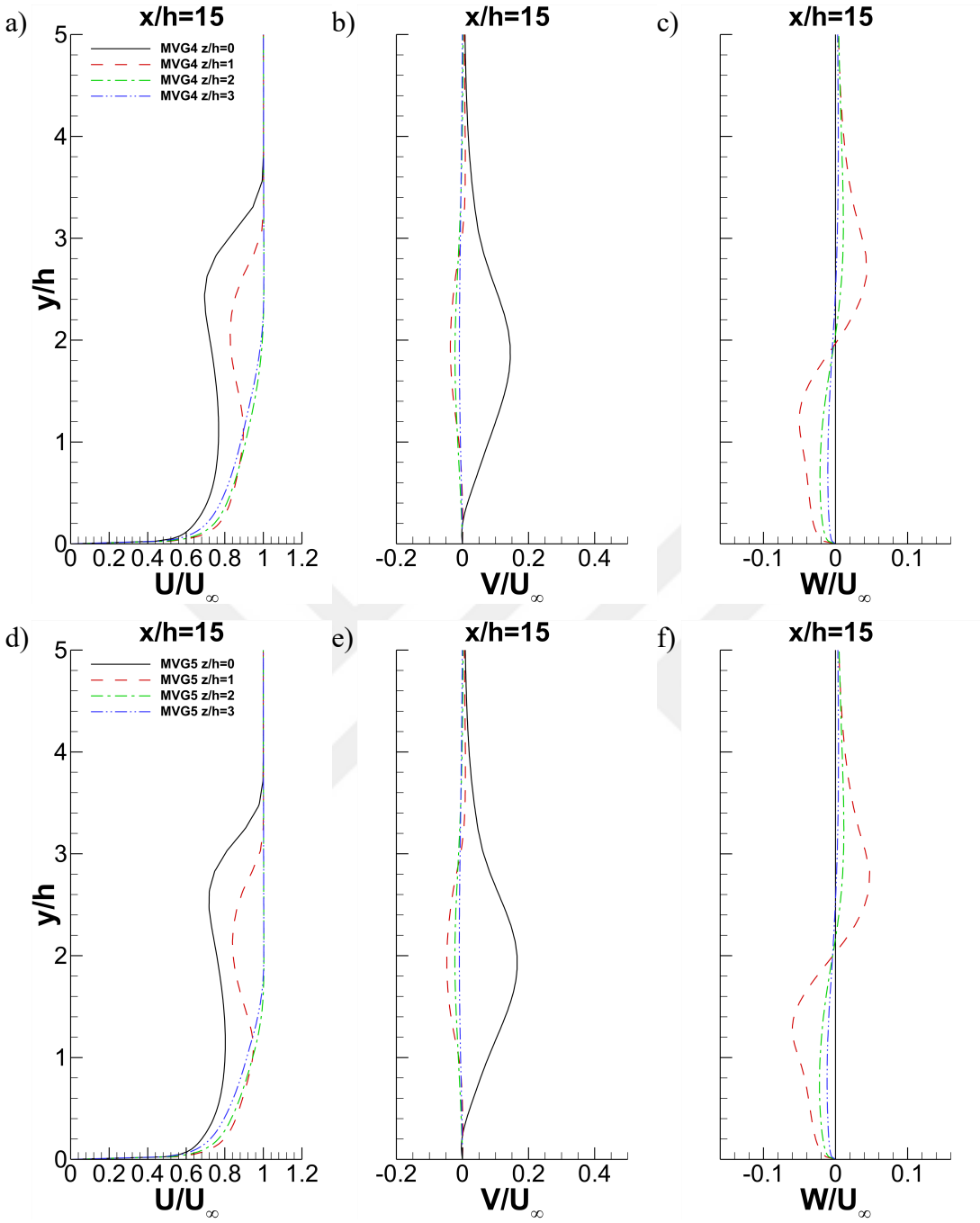

Figure A.8.8 Comparison of the velocity components, first column: U, second column: V, and third column: W, at x/h=15 and z/h=0 to 3 for MVG4 (top row) and MVG5 (bottom row).

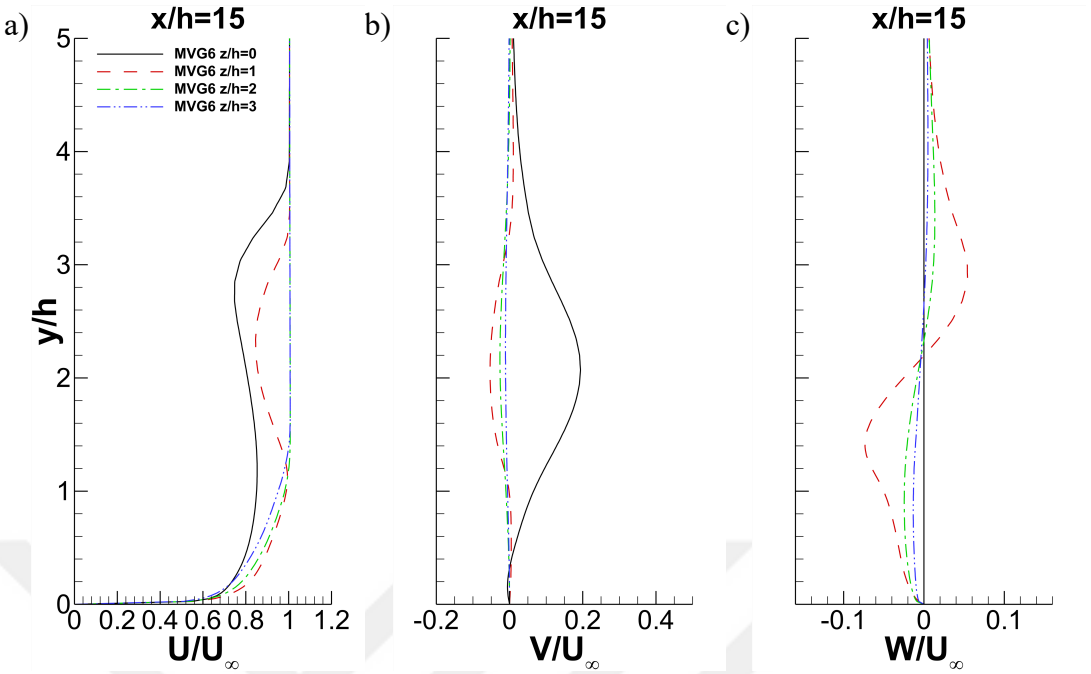

Figure A.8.9 Comparison of the velocity components, first column: U, second column: V, and third column: W, at x/h=15 and z/h=0 to 3 for MVG6.

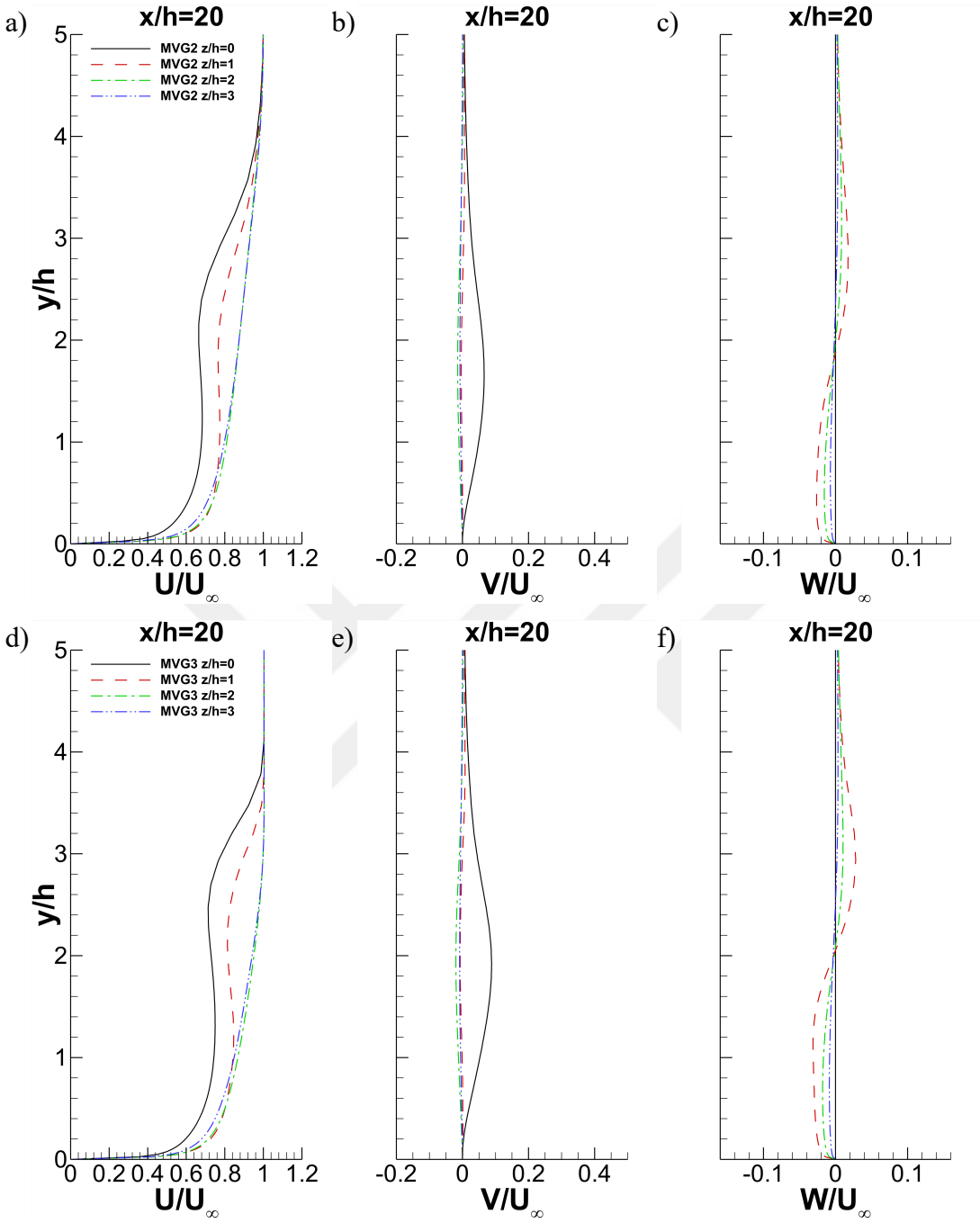

Figure A.8.10 Comparison of the velocity components, first column: U, second column: V, and third column: W, at x/h=20 and z/h=0 to 3 for MVG2 (top row) and MVG3 (bottom row).

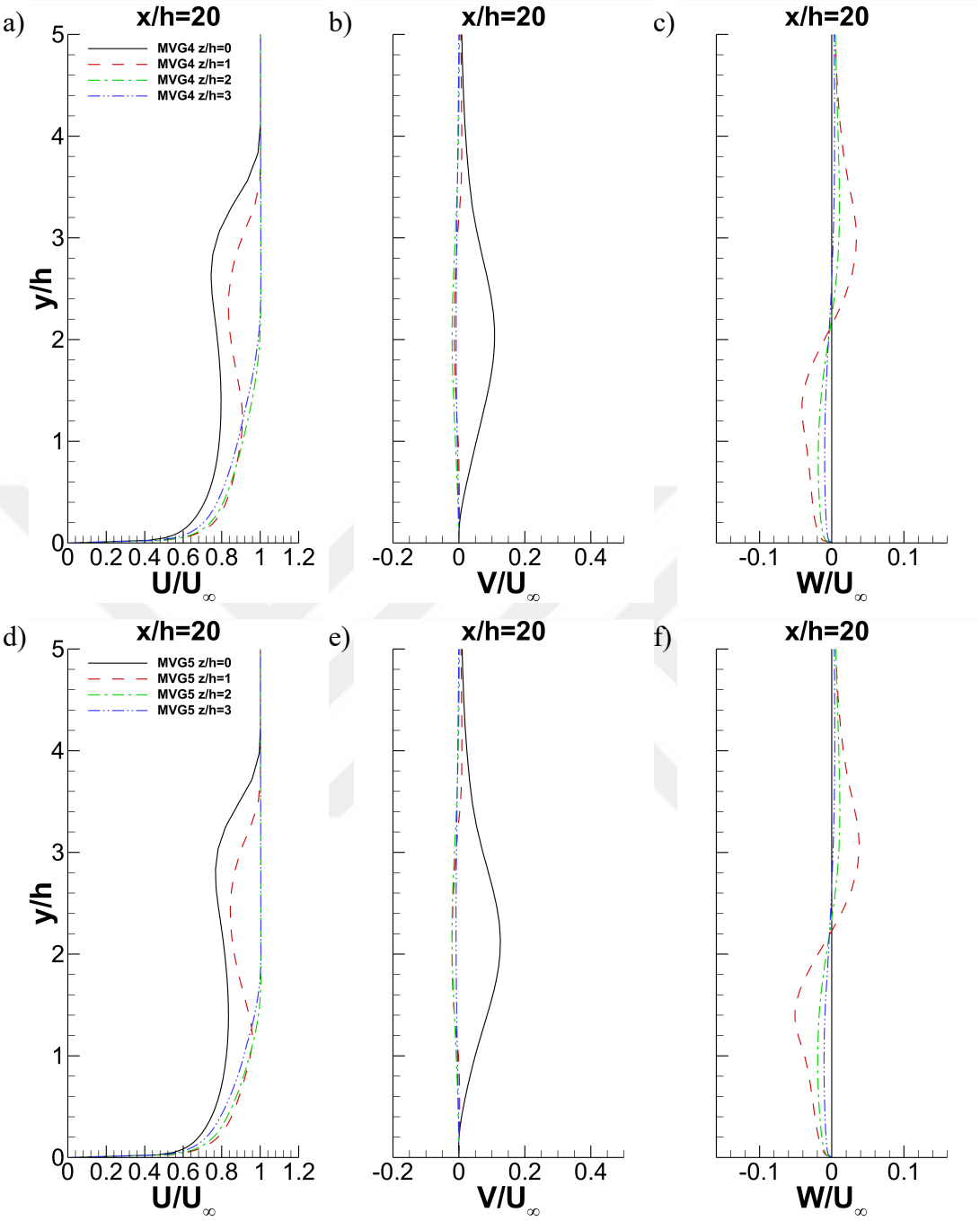

Figure A.8.11 Comparison of the velocity components, first column: U, second column: V, and third column: W, at x/h=20 and z/h=0 to 3 for MVG4 (top row) and MVG5 (bottom row).

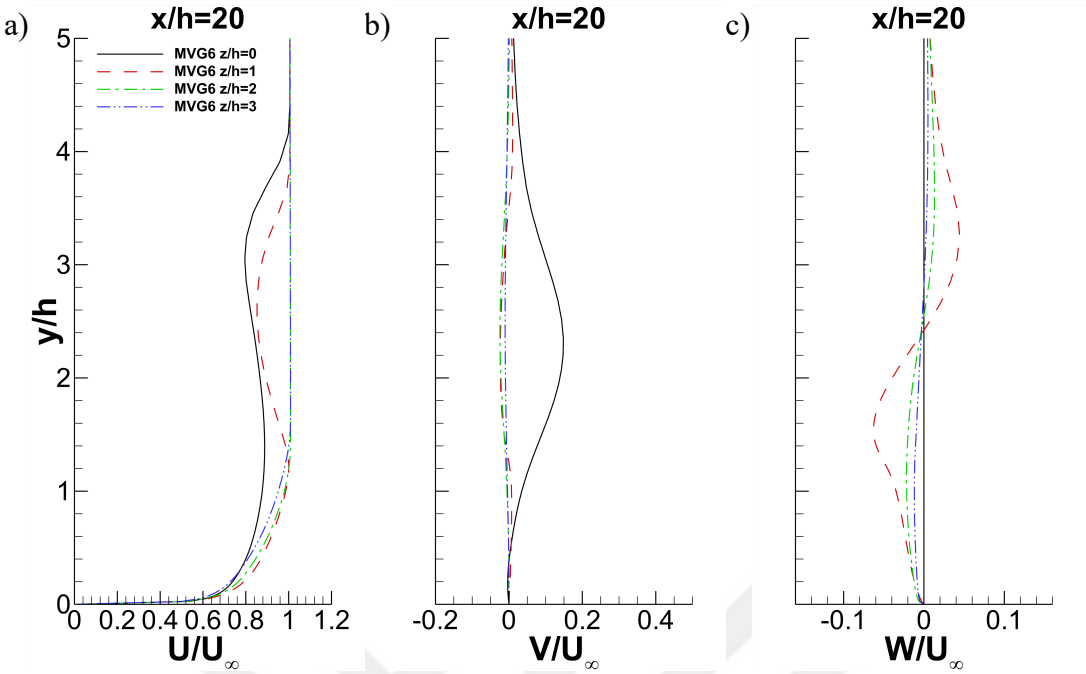

Figure A.8.12 Comparison of the velocity components, first column: U, second column: V, and third column: W, at x/h=20 and z/h=0 to 3 for MVG6.

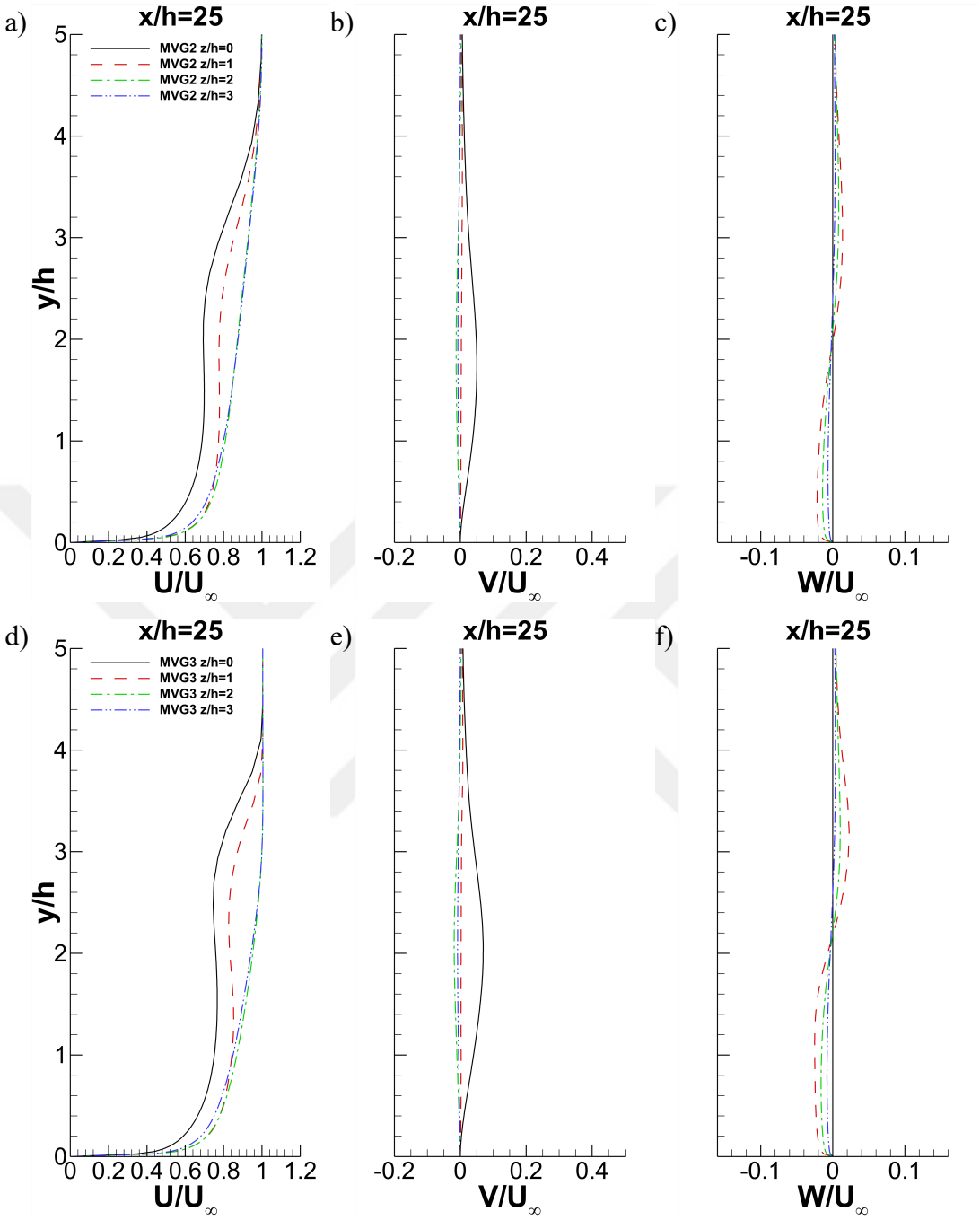

Figure A.8.13. Comparison of the velocity components, first column: U, second column: V, and third column: W, at x/h=25 and z/h=0 to 3 for MVG2 (top row) and MVG3 (bottom row).

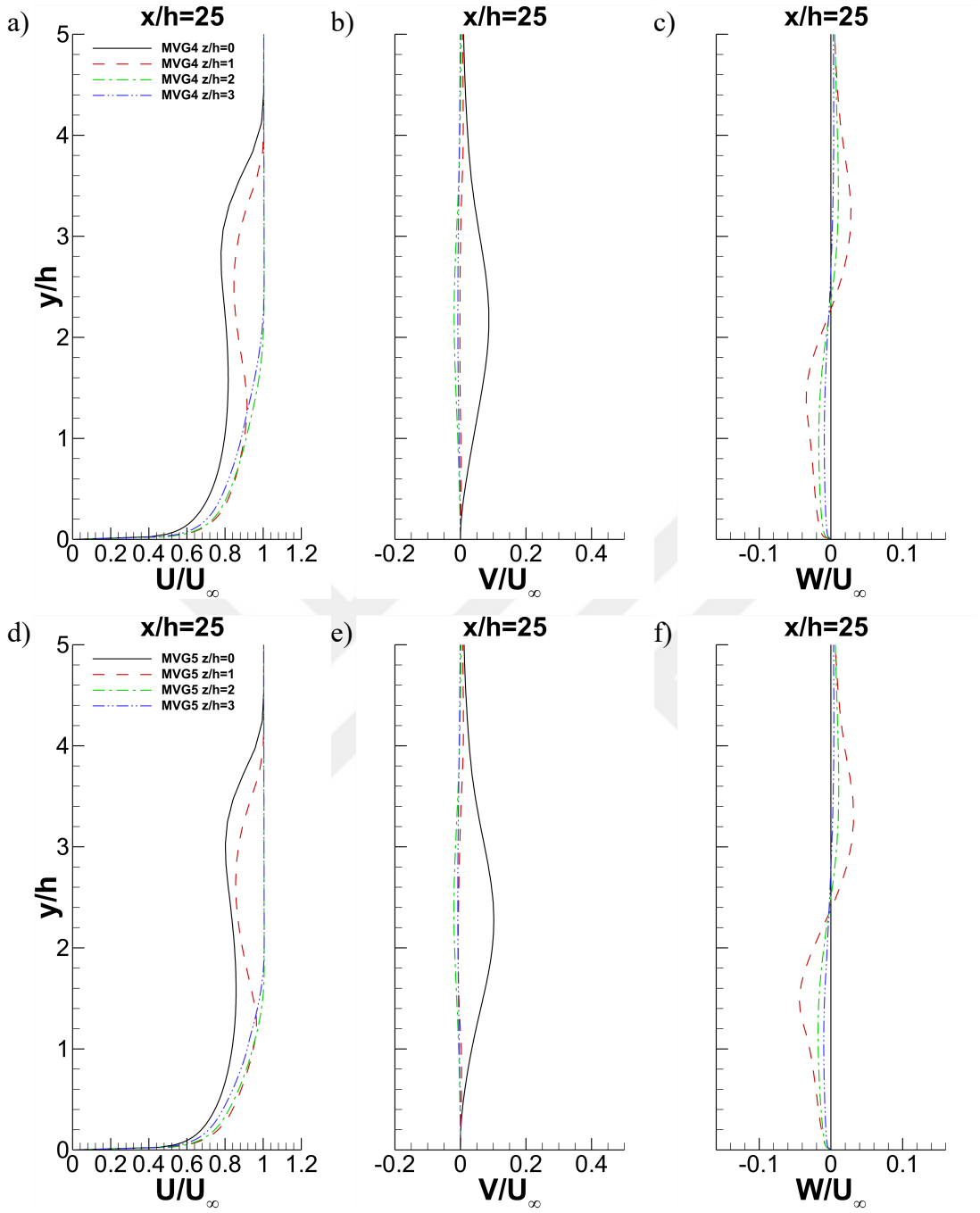

Figure A.8.14. Comparison of the velocity components, first column: U, second column: V, and third column: W, at x/h=25 and z/h=0 to 3 for MVG4 (top row) and MVG5 (bottom row).

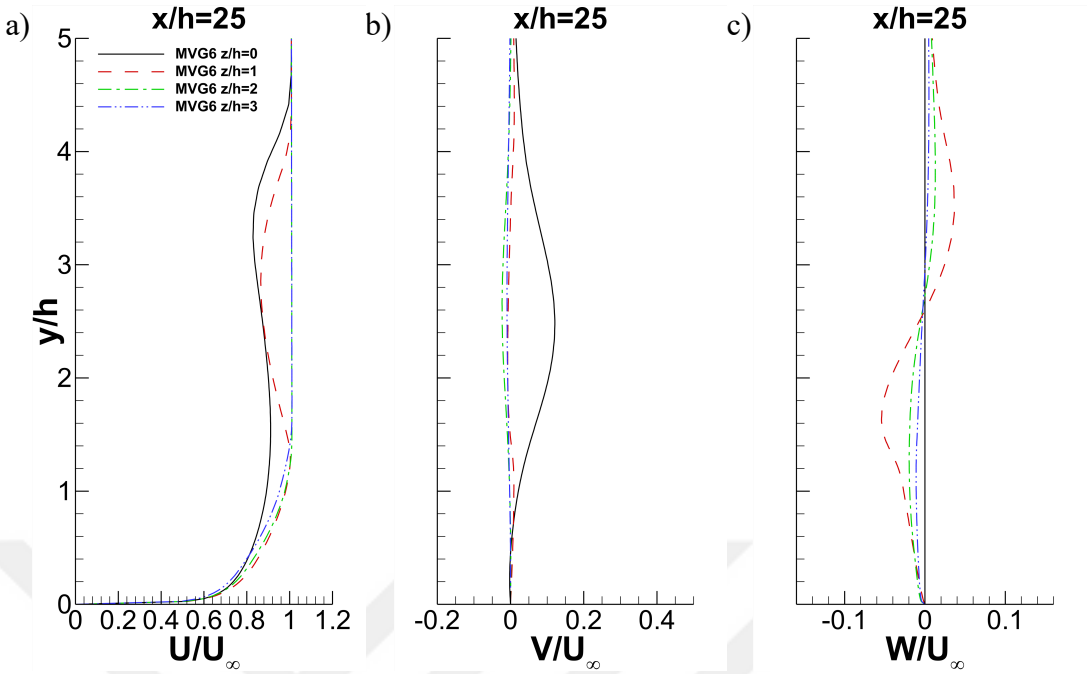

Figure A.8.15. Comparison of the velocity components, first column: U, second column: V, and third column: W, at x/h=25 and z/h=0 to 3 for MVG6.

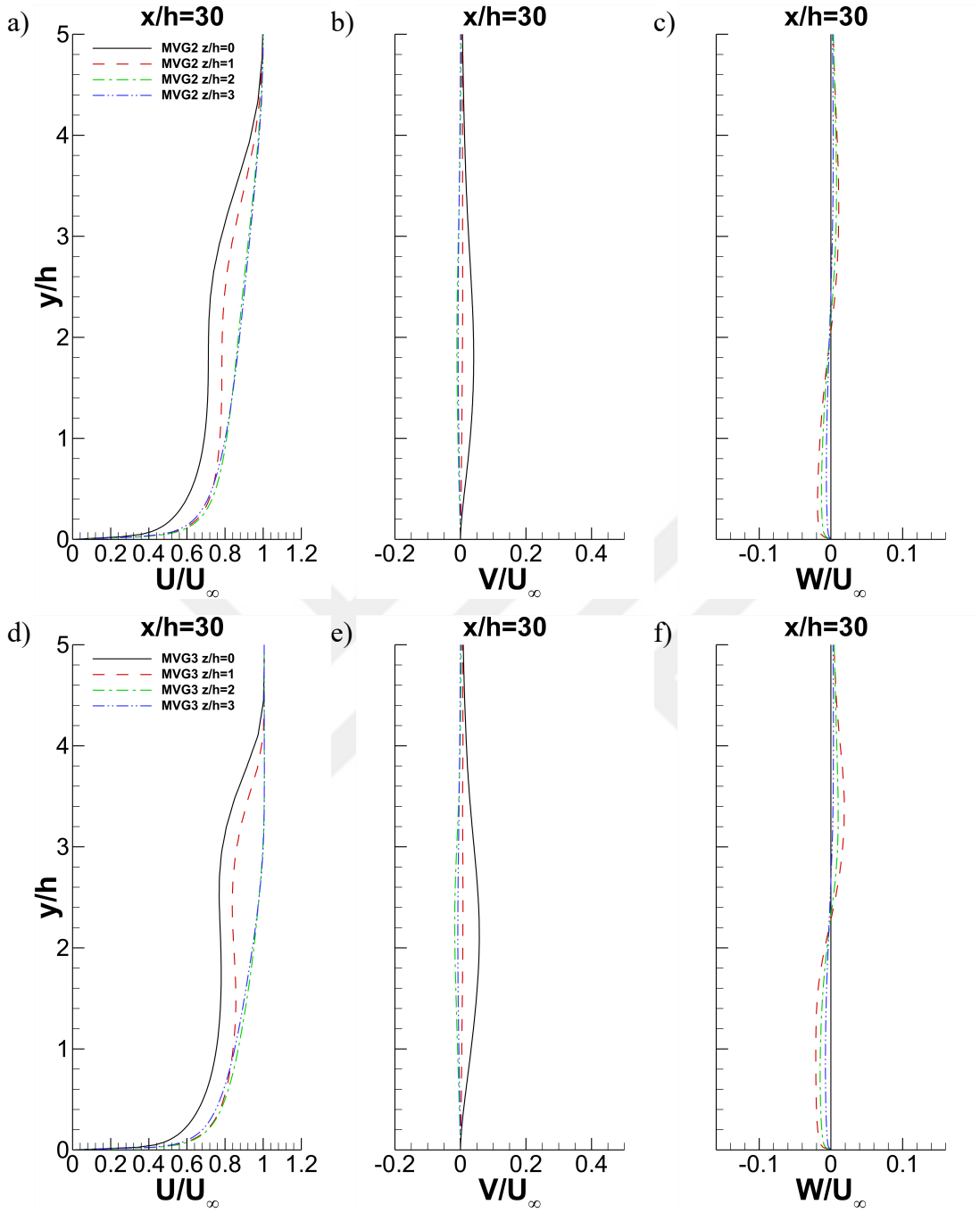

Figure A.8.16. Comparison of the velocity components, first column: U, second column: V, and third column: W, at x/h=30 and z/h=0 to 3 for MVG2 (top row) and MVG3 (bottom row).

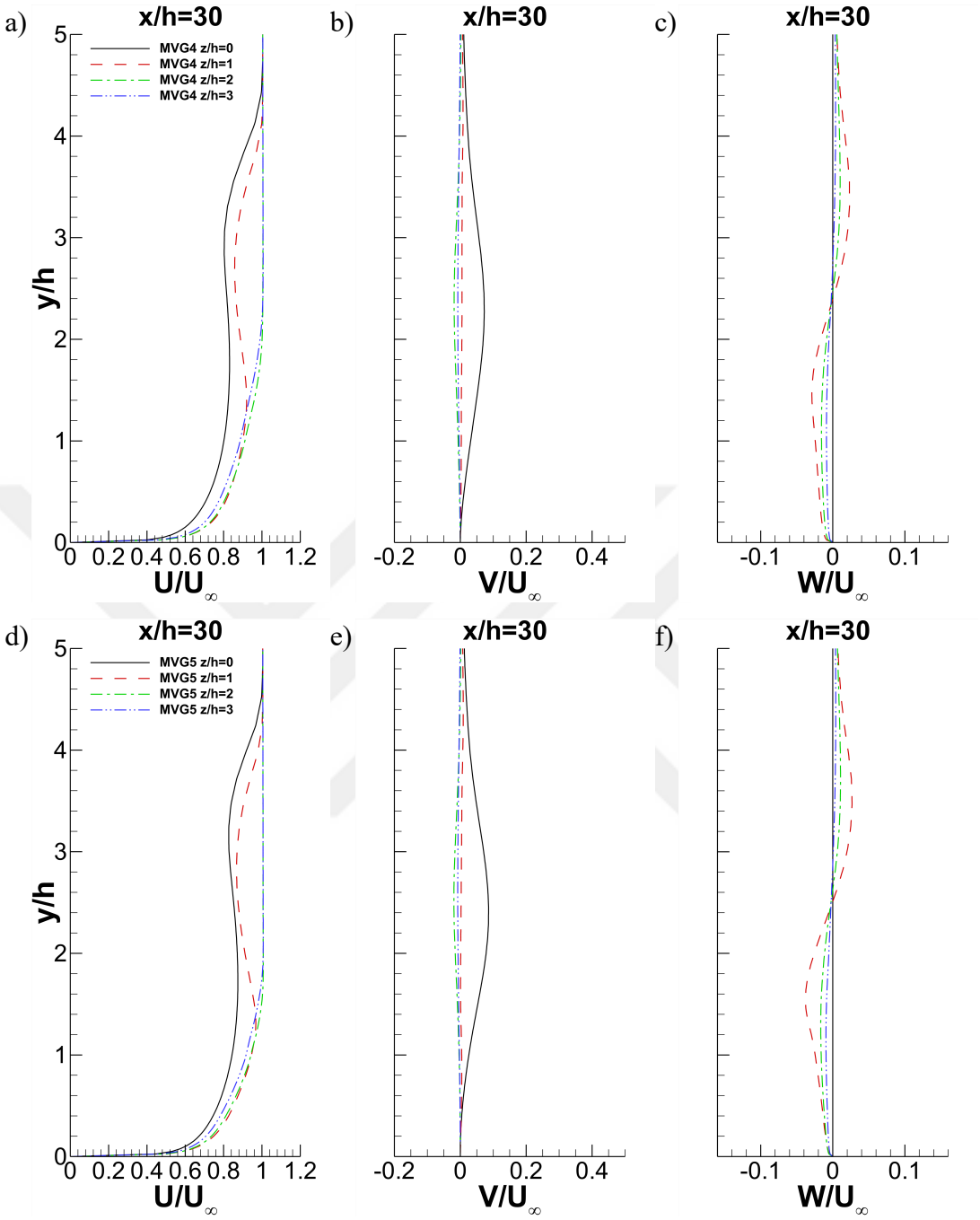

Figure A.8.17. Comparison of the velocity components, first column: U, second column: V, and third column: W, at x/h=30 and z/h=0 to 3 for MVG4 (top row) and MVG5 (bottom row).

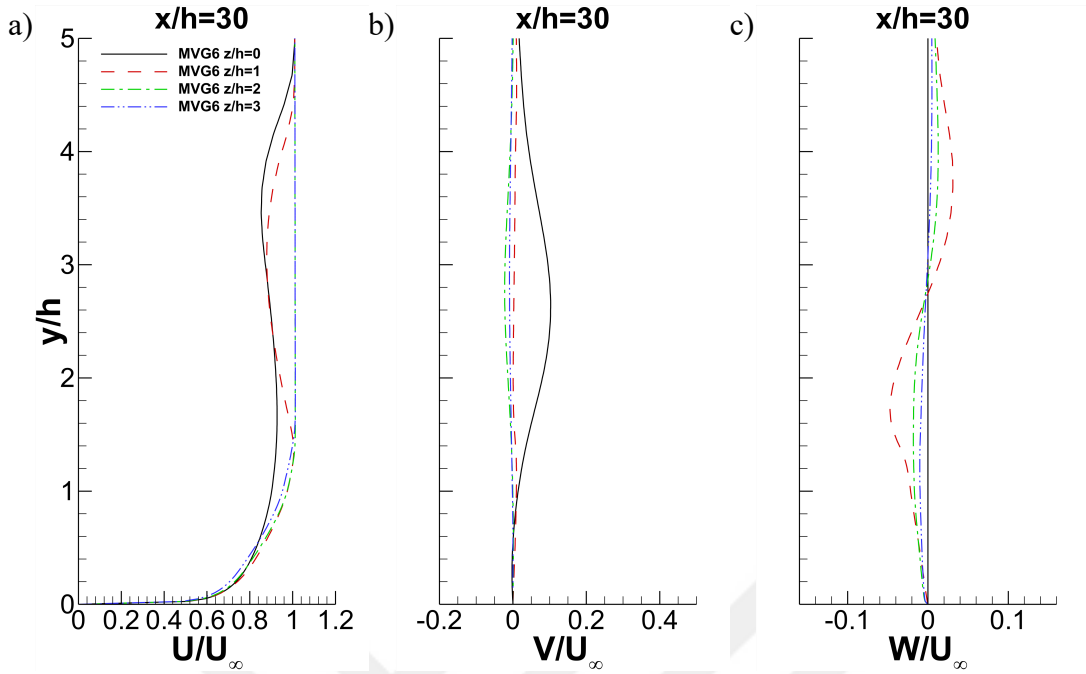

Figure A.8.18. Comparison of the velocity components, first column: U, second column: V, and third column: W, at x/h=30 and z/h=0 to 3 for MVG6.

B. Decay of the Streamwise Vorticity Component

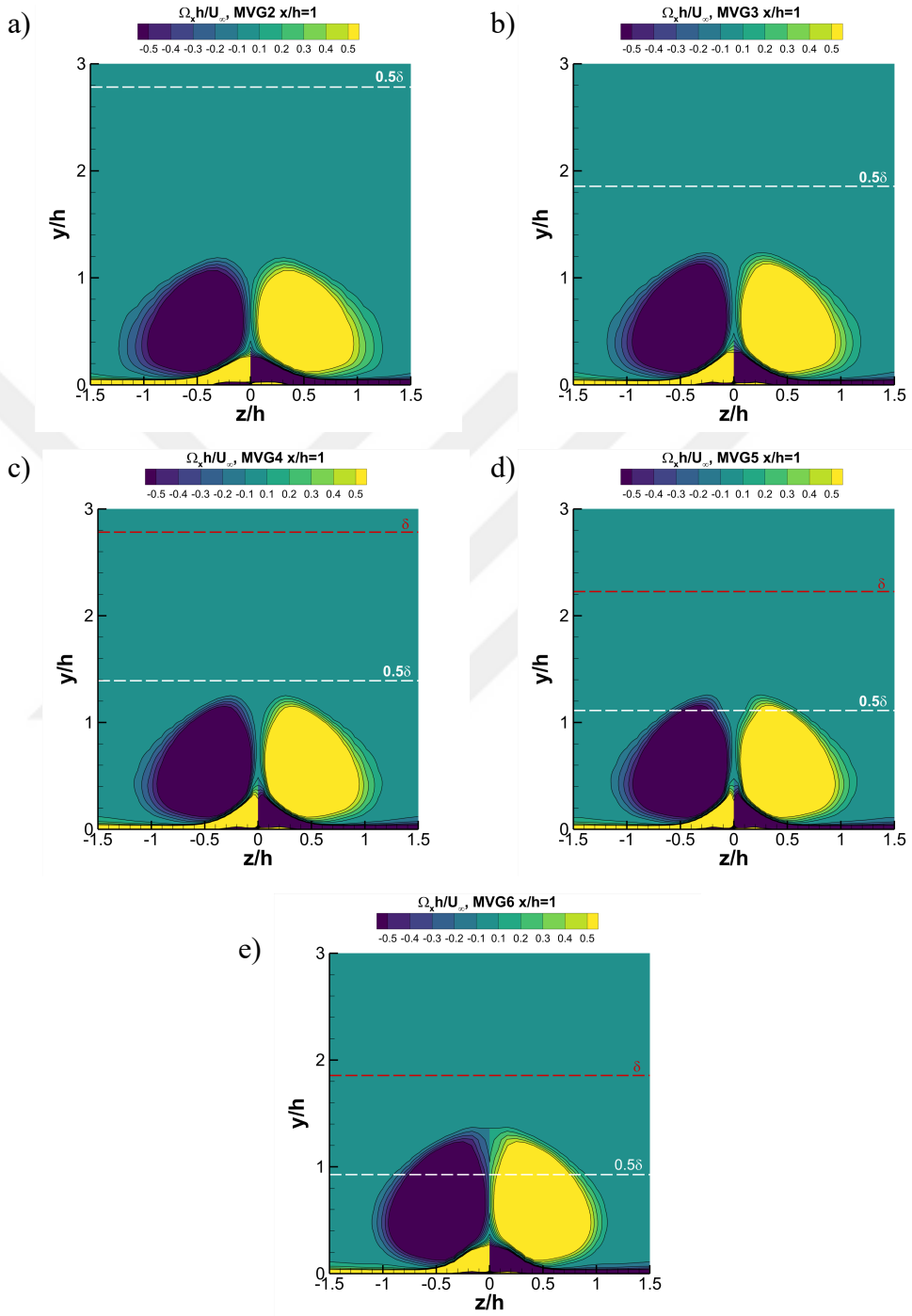

Figure B.8.19 Contours of normalized streamwise vorticity component ($\Omega_x h/U_\infty$) shown over x-planes illustrating the counter-rotating vortices at x/h=1 for a) MVG2, b) MVG3, c) MVG4, d) MVG5, e) MVG6.

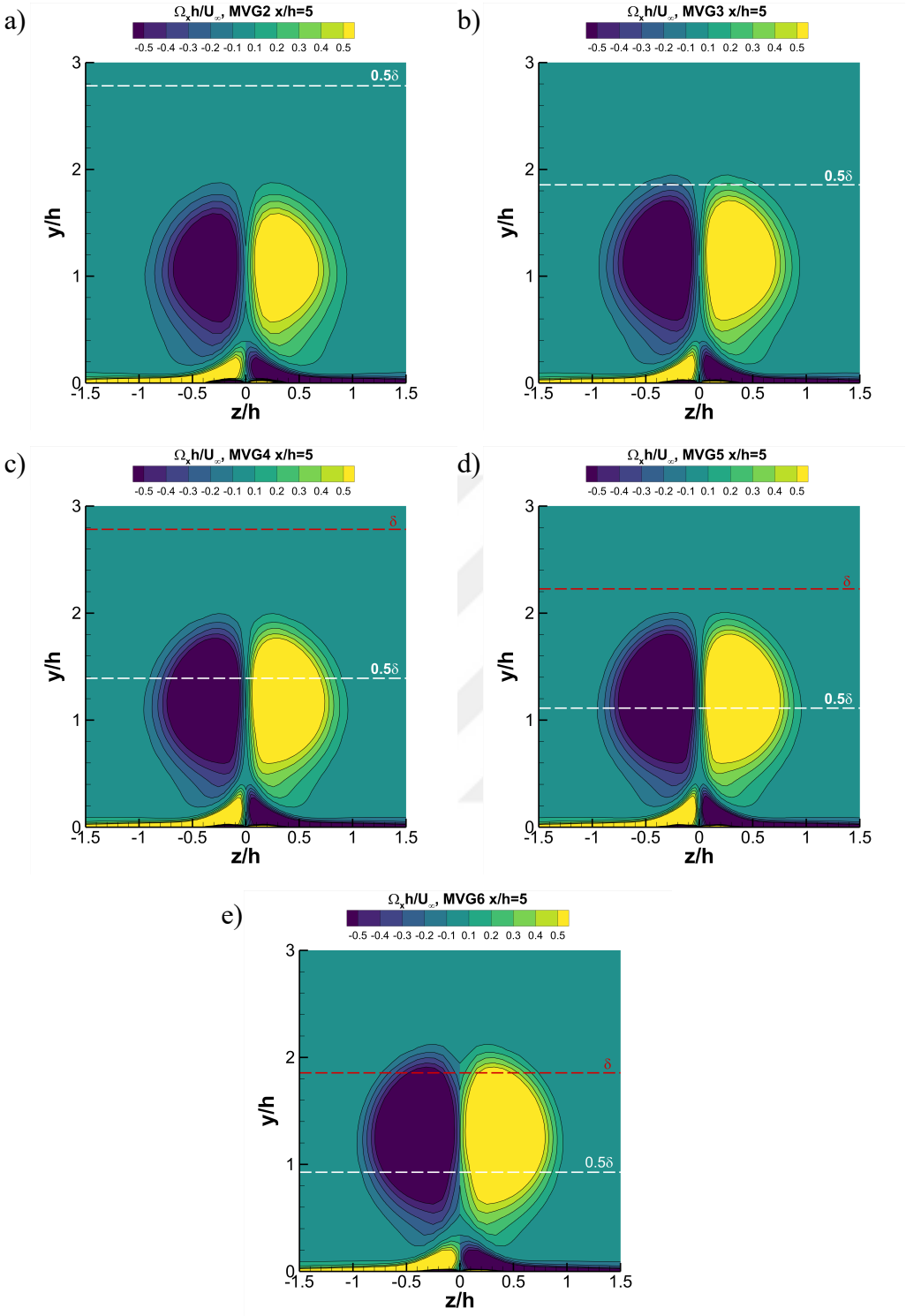

Figure B.8.20 Contours of normalized streamwise vorticity component ($\Omega_x h/U_\infty$) shown over x-planes illustrating the counter-rotating vortices at x/h=5 for a) MVG2, b) MVG3, c) MVG4, d) MVG5, e) MVG6.

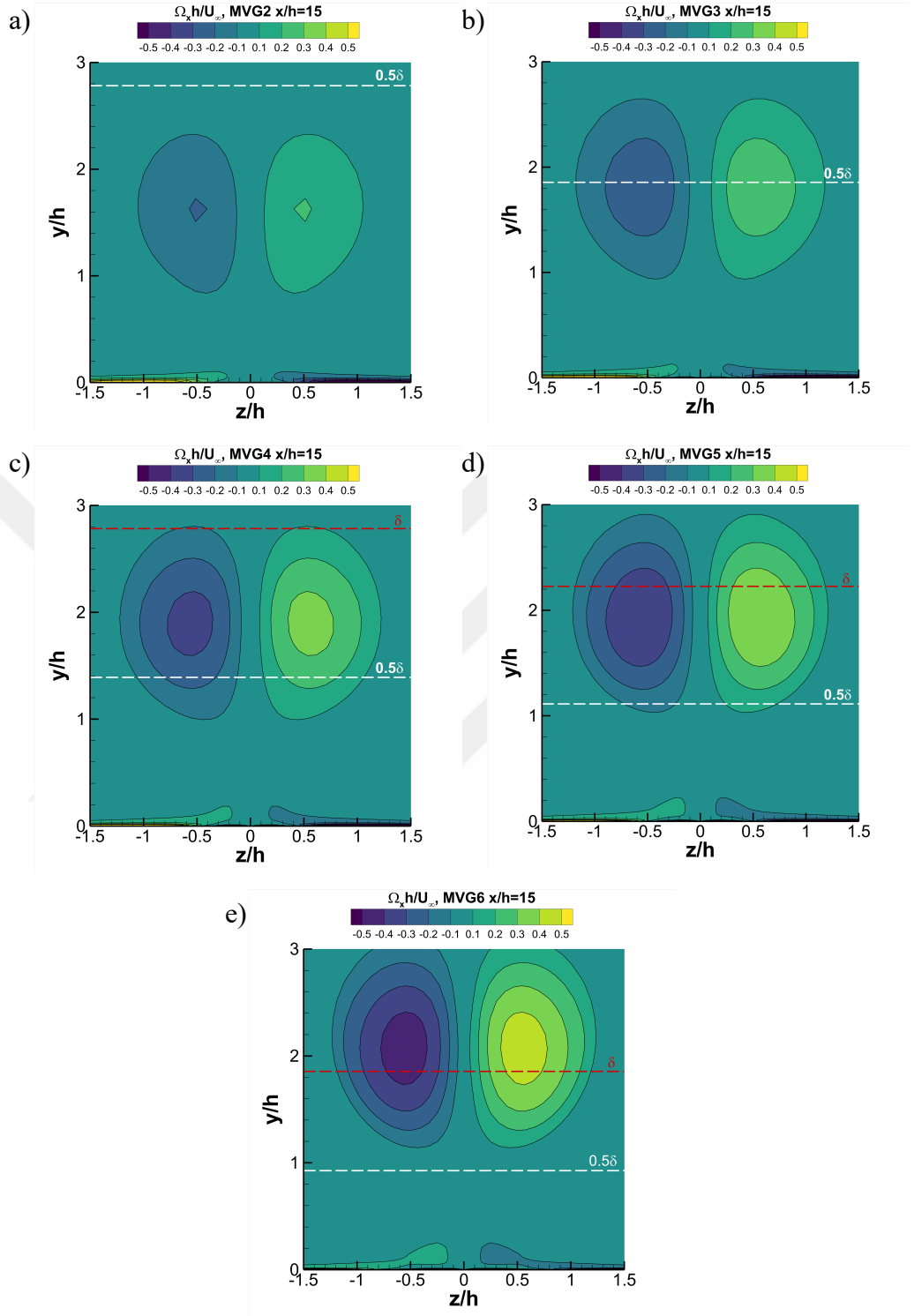

Figure B.8.21 Contours of normalized streamwise vorticity component ($\Omega_x h/U_\infty$) shown over x-planes illustrating the counter-rotating vortices at x/h=15 for a) MVG2, b) MVG3, c) MVG4, d) MVG5, e) MVG6.

CURRICULUM VITAE

PERSONAL INFORMATION

Surname, Name: Akpolat, Muhiddin Tuğrul

EDUCATION

Degree	Institution	Year of Graduation
MS	Erciyes University Energy Systems Engineering	2014
BS	Erciyes University Mechanical Engineering	2011
High School	Nevşehir High School, Nevşehir	2006

WORK EXPERIENCE

Year	Place	Enrollment
2017-2023	Roketsan Missiles Inc.	Lead Engineer
2016-2017	ODTÜ-RÜZGEM (METUWind)	Scientific Project Expert
2012-2016	Atılım University Civil Aviation School Airframe and Powerplant Maintenance Department	Research Assistant
2011-2012	Erciyes University Energy Systems Engineering Department	Project Assistant

FOREIGN LANGUAGES

Advanced English

PUBLICATIONS

1. **Akpolat, M. T.**, Öztürk, B., Hassanein, A., Perçin, M. "Mikro Vorteks Üreteçlerinin İz Bölgelerinin Karakteristikleri Üzerine Bir Çalışma", 17. Uluslararası Bilimsel Araştırmalar Kongresi, 19-20 August 2023, Ankara, Türkiye.

2. Öztürk, B., Hassanein, A., **Akpolat, M. T.**, Abdulrahim, A., Perçin, M., Uzol, O. "On the wake characteristics of a model wind turbine and a porous disc: Effects of freestream turbulence intensity", Renewable Energy, 212, 238-250 (2023)

3. Öztürk, B., Hassanein, A., **Akpolat, M. T.**, Abdulrahim, A., Perçin, M., and Uzol, O. "Effects of freestream turbulence on the wake growth rate of a model wind turbine and a porous disc", Journal of Physics: Conference Series, 2265, p. 022042 (2022).

4. Yigili, I., Andirin, M. A., **Akpolat, M. T.**, Baskan, O., Percin, M., and Uzol, O. "Design of a gust generator and comparison of model wind turbine and porous disc wake flows in a transverse gust", Journal of Physics: Conference Series, vol. 2265, p. 022108 (2022)

5. Abdulrahim, A., **Akpolat, M. T.**, Hassanein, A., Perçin, M., & Uzol, O. "Effects of inflow boundary layer on the wake of a radially non-uniform porous disk", Journal Of Renewable And Sustainable Energy, 13(3), 033302. doi: 10.1063/5.0045404 (2021)

6. Abdulrahim, A., **Akpolat, M. T.**, Perçin, M., and Uzol, O. "Comparison of analytical wake model predictions with experimental data for a non-uniform porous disc for uniform and non-uniform inflow," Wind Energy Science Conference (WESC) - 2021.

7. **Akpolat, M. T.**, Abdulrahim, A., Hassanein, A., Uzol, O., Percin, M. "Experimental Characterization of Micro Vortex Generators in Low-Speed Flows", 10th Ankara International Aerospace Conference, 8-10 September 2021, METU, Ankara, Türkiye.

8. Bahan, D., **Akpolat , M. T.**, Çitak, C., Harputlu, Ö., Gürses, K., and Acar, B. "Experimental Evaluation of Aerodynamic Performance and Structural Excitation Characteristics of a Supersonic Air Inlet", AIAA 2021-2494, in AIAA AVIATION 2021 FORUM, August 2021.

9. Ostovan, Y., **Akpolat, M. T.**, Uzol, O. "Experimental Investigation of the Effects of Winglets on the Tip Vortex Behavior of a Model Horizontal Axis Wind Turbine using Particle Image Velocimetry", J. Sol. Energy Eng. 141(1): 011006 (13 pages), (2019).

10. **Akpolat, M. T.**, Arısoy, E., Çıtak, C., Harputlu, Ö., Aksu, T. "Experimental Validation of an Air Intake Performance", 10th Ankara International Aerospace Conference, 18-20 September 2019, METU, Ankara, Türkiye.

11. Bozkır, B., **Akpolat, M. T.**, Arısoy, E., Karpuzcu, I. T. "Experimental and Numerical Design and Characterisation of a Supersonic Ideal Nozzle for Free-Jet Test Facilities", 10th Ankara International Aerospace Conference, 18-20 September 2019, METU, Ankara, Türkiye.

12. Çıtak, C., Harputlu, Ö., Arısoy, E., Aksu, T., **Akpolat, M. T.** "Computation Methodology of Performance Characteristics for a Supersonic Air Intake",10th Ankara International Aerospace Conference, 18-20 September 2019, METU, Ankara, Türkiye.

13. Aksu, T., Çıtak, C., Harputlu, Ö., **Akpolat, M. T.**, Arısoy, E. "Inlet Geometry Effect on Combustion in a Ducted Rocket Combustor", 10th Ankara International Aerospace Conference, 18-20 September 2019, METU, Ankara, Türkiye.

14. Arısoy, E., **Akpolat, M. T.**, Aksu, T., Çıtak, C., Harputlu, Ö. "Study on Shock Wave-Boundary Layer Interaction on a Mixed Compression Air Intake", 10th Ankara International Aerospace Conference, 18-20 September 2019, METU, Ankara, Türkiye.

15. Harputlu, Ö., Aksu, T., **Akpolat, M. T.**, Arısoy, E., Çıtak, C. "Effect of Bleed System on Air Intake Performance", 10th Ankara International Aerospace Conference, 18-20 September 2019, METU, Ankara, Türkiye.

16. Uluocak, S., Hazaveh, H. A., Perçin, M., **Akpolat, M. T.**, Uzol, O. "Experimental Investigation of The Effects of Different Helicopter Rotor Tip Geometries on Aerodynamic Performance and Tip Vortex Characteristics", 44th European Rotorcraft Forum, Delft, The Netherlands, 19-20 September, 2018.

17. Uluocak, S., Hazaveh, H. A., Perçin, M., **Akpolat, M. T.**, Uzol, O. "Helikopter Pal Ucu Şekillerinin Aerodinamik Performansa ve Uç Girdabına Etkisinin Deneysel Olarak İncelenmesi", VII. Ulusal Havacılık ve Uzay Konferansı, 12-14 September 2018, Samsun, Türkiye.

18. Ostovan, Y., **Akpolat, M. T.**, Uzol, O. "Experimental Investigation of the Effects of Winglets on the Tip Vortex Behavior of a Model Horizontal Axis Wind Turbine using Particle Image Velocimetry", Wind Energy Science Conference 2017, Technical University of Denmark, Lyngby Campus 26 June - 29 June 2017.

19. Genc, M. S., Açıkel, H. H., **Akpolat, M. T.**, Özkan, G., Karasu, İ. "Acoustic control of flow over NACA 2415 aerofoil at low Reynolds numbers", Journal of Aerospace Engineering-ASCE, vol.29, pp.04016045-1-04016045-19 (2016)

20. Genc, M. S., Karasu, İ., Açıkel, H. H., **Akpolat, M. T.**, Özkan, G. "Acoustic Control of Flow over NACA2415 Aerofoil at Low Reynolds Numbers", Sustainable Aviation Energy and Environmental Issues, Editors: Karakoc, T.H., Ozerdem, M.B., Sogut, M.Z., Colpan, C.O., Altuntas, O., Açıkkalp, E., Springer International Publishing, ISBN 978-3-319-34181-1 (2016)

21. **Akpolat, M. T.**, Toker, K. A., Genç, M. S. "Design and Optimization of a Notional Scramjet by Means of Stream Thrust Analysis and Design of Experiments", 19th AIAA International Space Planes and Hypersonic Systems and Technologies Conference, Georgia, Atlanta, USA, June 2014.

22. Genc, M. S., Karasu, İ., Açıkel, H. H., **Akpolat, M. T.** "Low Reynolds Number Flows and Transition", Low Reynolds Number Aerodynamics and Transition, Editor: M. Serdar GENÇ, InTech-Open Access Publishing, ISBN 978-953-51-0492-6 (2012)

23. Genc, M. S., **Akpolat, M. T.**, Açıkel, H. H., Karasu, İ. "An Experimental Study of Perpendicular Acoustic Disturbances Effect on Flow Over an Aerofoil at Low Reynolds Numbers", ASME 2012 International Mechanical Engineering Congress & Exposition IMECE2012, November 9-15, 2012, Houston, Texas, USA.

24. Karasu, İ., Genc, M. S., Açıkel, H. H., **Akpolat, M. T.** "Düşük Re Sayılı Akışlarda NACA2415 Kanat Profili Üzerinde Oluşan Laminer Ayrılma Kabarcığının Deneysel İncelenmesi", IV. Ulusal Havacılık ve Uzay Konferansı, 12-14 September 2012, İstanbul, Türkiye.

25. Açıkel, H. H., Genc, M. S., **Akpolat, M. T.**, Karasu, İ. "Düşük Re Sayılı Akışta NACA2415 Kanat Profili Üzerinde Oluşan Laminer Ayrılma Kabarcığına Akışa Paralel Ses Dalgalarının Etkisi", IV. Ulusal Havacılık ve Uzay Konferansı, 12-14 September 2012, İstanbul, Türkiye.

26. Açıkel, H. H., Genç, M. S., **Akpolat, M. T.**, Karasu, İ. "An experimental study of acoustic disturbances effect on laminar separation bubble and transition on an aerofoil at low Reynolds number", AIAA-2012-2684, 6th AIAA Flow Control Conference, New Orleans, Louisiana, USA, 25-28 June 2012.

27. Karasu, İ., Genç, M. S., Açıkel, H. H., **Akpolat, M. T.** "An experimental study on laminar separation bubble and transition on an aerofoil at low Reynolds number", AIAA-2012-3030, 30th AIAA Applied Aerodynamics Conference, New Orleans, Louisiana, USA, 25-28 June 2012.